

**The TITAN Electron Beam Ion Trap:
Assembly, Characterization, and First Tests**

by

Michael Wayne Froese

A Thesis submitted to the Faculty of Graduate Studies
in partial fulfillment of the requirements for the degree of

Master of Science

Department of Physics and Astronomy
University of Manitoba
Winnipeg, Manitoba

© Michael Wayne Froese, 2006

Abstract:

The precision of mass measurements in a Penning trap is directly proportional to an ion's charge state and can be increased by using highly charged ions (HCI) from an Electron Beam Ion Trap (EBIT). By bombarding the injected and trapped singly charged ions with an intense electron beam, the charge state of the ions is rapidly increased. To use this method for short-lived isotopes, very high electron beam current densities are required of the TITAN EBIT, built and commissioned at the Max-Planck-Institute for Nuclear Physics in Heidelberg, Germany and transported to TRIUMF for the TITAN on-line facility. This EBIT has produced charge states as high as Kr^{34+} and Ba^{54+} with electron beams of up to 500 mA and 27 keV. Once the EBIT is operational at full capacity (5 A, 60 keV), most species can be bred into a He-like configuration within tens of ms.

Acknowledgements:

To all of those who have supported, given guidance, worked along side me, or even just smiled in the hallway in encouragement, thank you for making this degree possible.

I wish to thank Gerald Gwinner for allowing me the privilege of being his first graduate student. As complex as this degree was, given that it took place in Winnipeg, Heidelberg, and Vancouver, it worked as a result of your work and willingness to keep in contact, regardless of the time of day.

To those who were essentially my other supervisors, José Crespo Lopez-Urrutia, Jens Dilling, and Joachim Ullrich, thank you for your encouragement and the opportunity to work in your groups. In particular, I'd like to thank Jens for his support and for creating the TITAN group.

Besonders bedanken möchte ich mich bei den Mitarbeitern der EBIT-Gruppe am Max-Planck-Institut für Kernphysik, die den Bau dieser EBIT erst möglich gemacht haben. Herr Müller und Herr Bechberger, vielen Dank für Ihre Geduld und unglaublichen handwerklichen Fertigkeiten. Thomas Busch, danke für dein Engagement mir die Hochspannungsphysik näher zu bringen sowie elektrische und elektronische Bauteile zu entwerfen und zu bauen.

I can not forget to thank my coworkers at MPI who were always there for help and understanding: Başak Balli, Jo Blaszak, Johannes Braun, Günter Brenner, Hjalmar Bruhns, Numa Crosthwaite, Antonio González-Martínez, Katharina Kubicek, Alain Lapierre, Volkhard Mäkel, Chris Osborne, Alex Rohr, Christoph Sage, Rosario Soria, and Hiro Tawara.

To my TITAN coworkers at TRIUMF, Laura Blomeley, Maxime Brodeur, Paul Delheij, Jochen Pfister, Matthew Smith, and Vladimir Ryjkov; thank you for putting up with me while I was writing this. I look forward to working with you all this summer!

I would also like to thank all of my friends, classmates, and professors at the University of Manitoba for your support during the course-work part of this degree.

An den Rest des Seabiscuit-EBIT-Teams, Günther Sikler und Sascha Epp: Wir haben es geschafft! Es war eine Freude, mit Günther zusammenzuarbeiten, der ein Hauptgrund dafür ist, weshalb unsere EBITs so gut funktionieren. Man kann glücklich sein, solch gute Kollegen zu haben, die man auch als Freunde bezeichnen kann und die solche Geduld, Freundlichkeit und Wissen haben, aber auch die Weisheit, es mit anderen zu teilen!

I would like to thank my family for their years of support in shaping who I am and getting me here, never mind during the completion of this degree!

Schließlich möchte ich meiner Freundin Ruth danken. Ohne deine Liebe, Unterstützung, Verständnis und Geduld wäre diese Arbeit nicht möglich gewesen.

Contents

1	Introduction	1
1.1	Motivation for Precision Mass Measurements	1
1.2	Overview of the TITAN Setup	5
1.3	General EBIT Experimental Setup	9
1.4	EBIT History	13
2	Theory	17
2.1	Charge Breeding and Charge Breeding Devices	17
2.1.1	Charge Breeding Efficiency	18
2.1.2	Charge Breeding Speed	22
2.2	Primary Reactions in an EBIT	26
2.2.1	Electron Impact Excitation and Ionization	30
2.2.2	Dielectronic Recombination	33
2.2.3	Radiative Recombination	35
2.2.4	Charge Exchange	37
3	Experimental Setup	39
3.1	EBIT Components	39
3.1.1	Electron Gun	39
3.1.2	Ion Trap	42
3.1.3	Collector	47
3.1.4	Gas Injection System	49
3.1.5	Ion Optics	51
3.1.6	Support Devices	53
3.2	Assembly and Characterization of the TITAN EBIT	55
3.2.1	High Voltage Tests	55
3.2.2	Electron Gun Characterization	58
3.2.3	Trap Characterization	62
3.2.4	Collector Characterization	72
3.2.5	Electron Beam Radius and Current Density	76

3.2.6	Electron Density and Space Charge	82
3.2.7	Assembly Notes	88
3.3	TITAN EBIT Diagnostic Components	91
3.3.1	X-ray Spectroscopy Setup	91
3.3.2	Installed Prism and Channeltron	94
4	First Tests and Results	97
4.1	Barium DR and Observed Charge States	97
4.2	Krypton Dielectronic Recombination	104
4.3	Axial Space Charge	108
5	Conclusion and Outlook	115
5.1	Conclusion	115
5.2	Outlook	117
A	TITAN EBIT Brief Operation Manual	121
A.1	Start Up Procedure	121
A.2	Shut Down Procedure	122
A.3	Venting the EBIT System - Excluding the Cathode Chamber	123
A.4	Restoring the High Vacuum	126
A.5	Venting the Backing Vacuum System	127
A.6	Restoring the Backing Vacuum	128
B	Additional EBIT Component Schematics, Figures, and Photos	131
B.1	Schematic Drawing for Replacement Part	131
B.2	EBIT Photos	133
B.3	Printable Figures	138
	Bibliography	141

List of Figures

1.1	<i>Ft</i> values of the most precisely known superallowed beta emitters (taken from [85])	4
1.2	Schematic layout of the TITAN experiment.	5
1.3	Schematic of magnetic field lines defining the area in which an electron can orbit.	9
1.4	Basic principles of an electron beam ion trap (modified from [18]). . .	11
1.5	Photo of the eight-fold radially segmented central trap electrodes. . .	12
1.6	Labelled cross-sectional TITAN EBIT overview.	14
2.1	Vacuum pressure at which charge state gains due to ionization equal charge exchange losses in Pb ions [4].	20
2.2	Electron energy at which charge state gains due to ionization are equal to radiative recombination losses in Pb ions [4].	21
2.3	Charge breeding simulation for Kr based on EBIT theoretical modeling with RR using the SUK program developed by Becker [5].	24
2.4	Charge breeding times of low Z elements based on EBIT theoretical modeling using the SUK program developed by Becker [5].	25
2.5	Charge breeding times of high Z elements based on EBIT theoretical modeling using the SUK program developed by Becker [5].	27
2.6	Charge breeding rates for Kr based on EBIT theoretical modeling without RR using the SUK program developed by Becker [5].	28
2.7	Atomic shells in an atom with some characteristic x-ray transitions between these levels.	29
2.8	Schematic of RR and DR with an initial He-like state from [72]. . . .	34
3.1	Cross-section view of the electron gun assembly.	40
3.2	Schematic layout of the EBIT HV power supplies.	42
3.3	Simulated TITAN EBIT axial magnetic field strength (data from [80]).	43
3.4	Cross-sectional overview of the TITAN EBIT trap electrodes.	44
3.5	Central trap electrode labelling nomenclature, with respect to the electron beam direction.	45

3.6	Photo looking inside a magnet vacuum chamber port with the magnet former and thermal shield windows removed.	46
3.7	Photo of the gas injection slit installed on the magnet former.	47
3.8	Cross-sectional view of the electron collector.	48
3.9	The two-stage differentially pumped gas injection system.	49
3.10	Photo of the gas injection shield slit assembly.	50
3.11	Photo of the installed gas injection shield slit assembly.	51
3.12	Steerer lens for ion beam steering and focusing.	52
3.13	Schematic of the secondary side transformer electrical connections to the HV rack.	54
3.14	Photo of the central segmented trap electrodes with attached wires.	56
3.15	Cross-section view of the cathode assembly for the small 0.5 A cathode.	59
3.16	Electron gun components with schematic electrical circuits.	60
3.17	Initial superconducting 6 T magnet temperature regions.	64
3.18	The thermal connection between the magnet's thermal shield and the transition electrodes, C_{trans} and G_{trans}	65
3.19	Photo of the folded electrode wires in the ceramic insulators.	67
3.20	Schematic of the parallel capacitance during the RF crosstalk measurement.	71
3.21	Collector coil tests plotting magnetic field vs current.	75
3.22	Collector coil tests plotting voltage vs current.	76
3.23	Calculated Herrmann radius plotted against the residual magnetic field B_c at the cathode.	79
3.24	Calculated Herrmann radius as a function of cathode temperature T_c (a), axial magnet field B (b), electron beam current I_e (c), and electron beam energy E_e (d).	81
3.25	Electron current density plotted against beam current for the TITAN EBIT.	83
3.26	Sample plot of the radial space charge	85
3.27	Calculated axial space charge due to trap geometry.	87
3.28	Photo of the misalignment of the magnet thermal shield.	88
3.29	Photo showing the thermal shield misalignment.	89
3.30	Photo of the points chosen for trap alignment.	89
3.31	Photo of the channeltron and prism installed between the magnet and electron gun chambers.	95
3.32	Channeltron schematic.	96
4.1	Spectrum of a DR resonance in Ba.	99
4.2	Energy calibration for the DR resonance in Ba.	101
4.3	Two overlaid Ba spectra with electron beam energies of 23 and 25 keV.	102

4.4	Energy calibration for the Ba spectra using electron beams of over 20 keV.	103
4.5	Spectrum of the KLL DR resonance in Kr at 13 keV.	106
4.6	Energy calibration for the DR resonance in Kr.	108
4.7	Inferred axial space charge plotted as a function of electron beam current I_e	110
4.8	Measured and calculated axial space charge plotted as a function of electron beam current I_e	111
4.9	Cross-sectional view of the TITAN EBIT with the axial magnetic field strength plotted below.	112
A.1	Schematic of EBIT vacuum system from 2005 (modified from [88]).	125
B.1	Modified copper ring schematic for use with the TITAN EBIT collector and electron gun vacuum seals.	132
B.2	Photo of the trap with connected wires during assembly.	133
B.3	The collector head after partial assembly.	134
B.4	The collector head during assembly.	134
B.5	The prism and channeltron assembly installed between the magnet and the electron gun.	135
B.6	Backside view of the channeltron and prism installed for diagnostic purposes.	135
B.7	The high voltage power supply setup used to float the electronics, electron gun, and collector to -20 kV.	136
B.8	Controller box for one of the steerer lenses used for ion beam focusing and steering.	137
B.9	Electrical schematic of the primary side of the transformer used for the HV cage.	138
B.10	Company label on the transformer with additional specifications.	138
B.11	Labels for the two twelve-piece electrical feedthroughs for the trap electrodes.	139
B.12	Trap electrode labels with the electron gun on the left side.	140

List of Tables

1.1	Summarized properties of selected EBITs.	15
2.1	Some ionization values of high Z elements included in the charge breeding time simulations [3].	23
2.2	Rate and cross-section estimates for charge changing reactions using Rb^{34+} with $E_e = 20$ keV.	38
3.1	Summarized power supply specifications for the electron gun.	59
3.2	Summarized recommended maximum values and characteristic values of the bucking and trim coils in the electron gun.	62
3.3	Measured capacitance between the TITAN EBIT trap electrodes.	70
3.4	RF crosstalk amplitudes between all 17 trap region electrodes.	73
3.5	Summarized recommended maximum values and other characteristic values of the collector coil.	74
3.6	Heat Wave dispenser cathode characteristic performance	82
3.7	Some calibration sources and their respective dominant emission lines [35].	91
3.8	Properties of the solid-state, planar, high purity germanium detector used during the first tests of the TITAN EBIT.	93
4.1	Table of relevant Ba ionization energies for the presented results [3].	98
4.2	Table of some Kr ionization energies [91].	104
4.3	Typical TITAN EBIT operational parameters (used while measuring the axial space charge).	109

Glossary

CPET: cooling Penning trap, 5

CX: charge exchange, 23

DESY: Deutsches Elektronen-Synchrotron, 11

DR: dielectronic recombination, 23

EBIS: electron beam ion source, 8

EBIT: electron beam ion trap, 4

ECR: electron cyclotron resonance, 15

ECRIS: electron cyclotron resonance ion source, 15

EIE: electron impact excitation, 23

EII: electron impact ionization, 23

FEL: free electron laser, 11

HCI: highly charged ion, 27

HD: Heidelberg, Germany, 7

HV: high voltage, 44

ISAC: isotope separator and accelerator, 4

KLL: a DR resonance involving electrons in the K-shell and the L-shell, 30

LHC: Large Hadron Collider, 12

LLNL: Lawrence Livermore National Laboratory, 13

MCP: multi-channel plate detector, 48

MPET: measurement Penning trap, 5

MPI-K: Max-Planck-Institute for Nuclear Physics, 11

QED: quantum electrodynamics, 31

RFCT: radio-frequency quadrupole cooling trap, 4

RFQ: radio-frequency quadrupole, 6

RHIC: Relativistic Heavy Ion Collider, 12

RR: radiative recombination, 23

TITAN: TRIUMF's ion trap for atomic and nuclear science, 4

TRIUMF: TRI-University Meson Facility, 4

Chapter 1

Introduction

1.1 Motivation for Precision Mass Measurements

The binding energy of nucleons, or the mass that is converted into energy during fission or fusion processes, is one of the most fundamental properties of the nucleus. The motivation to understand this property spans from power generation (fission and fusion reactors) for today's society to explaining the cosmic abundances of elements heavier than iron. Binding energies can be measured by performing high precision (1 part in 10^8) mass measurements using a Penning trap in a laboratory. Such mass measurements allow the improvement of nuclear models that predict masses of isotopes, an understanding of astrophysical processes producing nuclei up to and beyond iron, the testing of fundamental concepts like the conserved vector current (CVC) hypothesis, and the investigation of the unitarity property of the Cabbibo-Kobayashi-Maskawa (CKM) matrix. Extremely high precision (≤ 0.2 parts in 10^9) mass measurements in a Penning trap have also led to increased accuracy of the determination of one of the most fundamental constants in physics, the fine-structure constant α [16].

During supernovae, novae, or x-ray bursts, nuclides initially formed from the fusion

process in a star can fuse with an abundant supply of hydrogen, allowing the formation of heavier elements. Elucidation of this rapid proton capture process and a similar process for neutrons can be accomplished by measuring properties such as the mass, lifetime, and capture cross sections of the various isotopes taking part in these processes [21].

The CKM matrix is a three by three rotation matrix describing the mixing of the weak and mass eigenstates of quarks [19, 54]:

$$\begin{pmatrix} V_{u,d} & V_{u,s} & V_{u,b} \\ V_{c,d} & V_{c,s} & V_{c,b} \\ V_{t,d} & V_{t,s} & V_{t,b} \end{pmatrix}$$

When one of the matrix elements is squared, taking V_{ud}^2 as an example, it represents the transition probability of an up quark, via the weak interaction, to convert into a down quark. The unitarity condition for the top row of the matrix has come under recent scrutiny as a method of testing the Standard Model, which describes the interactions of elementary particles, for new physics. This model predicts that the combined probabilities of the three terms (see Equation 1.1), describing the known mixings for the up quark should sum to one. A recent publication by Savard *et al.* [85] highlights the reduced error in the top row as a result of new mass measurements of superallowed $0^+ \rightarrow 0^+$ decays:

$$V_{ud}^2 + V_{us}^2 + V_{ub}^2 = 0.9985 \pm 0.0012. \quad (1.1)$$

Studies of $0^+ \rightarrow 0^+$ superallowed beta decays are ideally suited to determine the value of V_{ud} , as these transitions are pure Fermi decays, corresponding to the perfect overlap of the initial and final state wavefunctions. This allows for a simpler determination of

1.1. Motivation for Precision Mass Measurements

their respective ft values, where t is the half-life of the decay and f is a phase-space factor; ft values depend on measurements of the lifetime, the Q value, in addition to branching ratios of the decays for a particular species. The Q value is defined as the mass difference between the parent and the daughter nucleus in the decay and the branching ratio for a decay is the ratio between decay rates of individual decay modes and the total decay rate. The ft value is then corrected for nucleus-dependent radiative effects, allowing the comparison of these decays. This produces a so-called Ft value, which can have the form [43]:

$$Ft = ft(1 + \delta'_R)(1 + \delta_{NS} - \delta_C) = \frac{K}{2G_V^2(1 + \Delta_R^V)}, \quad (1.2)$$

which depends on the weak vector coupling constant G_V , a numerical constant K , an isospin symmetry-breaking correction δ_C , two transition-dependent parts of the radiative correction δ_{NS} and δ_C , and a transition-independent part of the radiative correction Δ_R^V . Relating back to the choice of using superallowed decays, the conserved vector current (CVC) hypothesis predicts that all such decays have the same G_V value. The average G_V value resulting from these decays can then be combined with the Fermi coupling constant (derived from the purely-leptonic muon decay) to produce the most accurate value for V_{ud} .

By examining the theory and Figure 1.1 from Savard *et al.* [85], it becomes clear that further reduction of the error associated with the Ft values of the superallowed beta decays would result in tighter constraints on the V_{ud} term of the CKM matrix. For clarification, the three terms have the values: $V_{ud} = 0.9736(4)$ [85], $V_{us} = 0.2248(19)$ (see discussion in [85]), and $V_{ub} = 3.67(47) \times 10^{-3}$ [33]. It, however, should be noted that the current uncertainty of the top row is dominated by the theoretical uncertainties in the V_{ud} and V_{us} terms.

One superallowed beta decay candidate to improve is ^{74}Rb . This isotope, however,

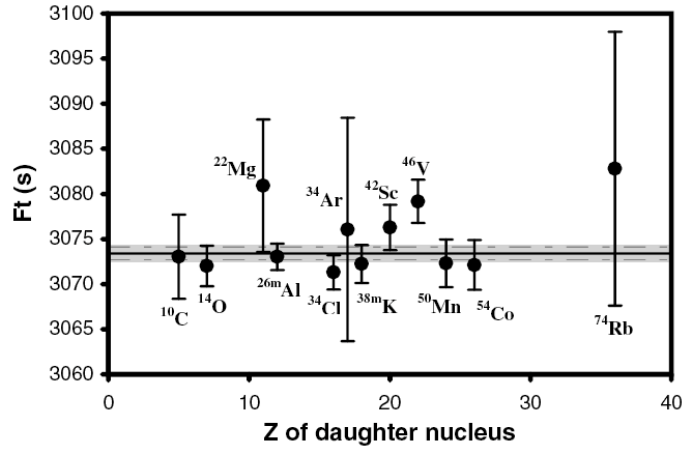


Figure 1.1: Ft values of the most precisely known superallowed beta emitters (taken from [85]). Note that ^{74}Rb has the largest error bar and the daughter nucleus with the highest Z . The mass determination of this species will be one of TITAN's first mass measurements to further test the CKM matrix. Reprinted figure with permission from G. Savard *et al.*, Phys. Rev. Lett., 95, 102501, 2005. Copyright (2005) by the American Physical Society. Abstract: <http://link.aps.org/abstract/PRL/v95/p102501>.

has a short lifetime of about 65 ms and is difficult to produce in useful quantities for use with Penning trap systems. Radioactive isotopes must be produced on-line for use in experimental setups. In Canada, this is done at TRIUMF (TRI-University Meson Facility), Canada's national laboratory for particle and nuclear physics located in Vancouver. The isotope separator and accelerator (ISAC) facility uses a cyclotron to accelerate protons up to energies of 500 MeV and currents up to 100 μA [59], which can be used to bombard a thick target, producing many reaction products. The produced atoms diffuse out of the target, become ionized and are subsequently electrostatically extracted to form a beam with energies of up to 60 keV. A dipole magnet is used to select the isotope of interest. The produced beam is then transported to the ISAC experiments, one of which is TRIUMF's Ion Trap for Atomic and Nuclear science (TITAN) [27]. The goal of this experiment is to perform high precision mass measurements ($\delta m/m \leq 1 \times 10^{-8}$) on short lived ($T_{1/2} \geq 50$ ms) radionuclides such as ^{74}Rb .

1.2 Overview of the TITAN Setup

As mentioned above, the TITAN experiment's goal is to perform high precision mass measurements on short lived radionuclides. To achieve this goal, the TITAN project will employ five main components (see Figure 1.2): a gas-filled linear radio-frequency quadrupole cooling ion trap (RFCT) for cooling and bunching the radioactive beam, an electron beam ion trap (EBIT) for breeding the ions to high charge states, a two Wien filter system (WIFI1 and WIFI2) for selecting specific mass-over-charge ratios, a cooler Penning ion trap (CPET) to cool the ions before mass measurement, and a Penning ion trap (MPET) for high precision mass measurements. Additionally, there are two off-line ion sources for component testing and optimization.

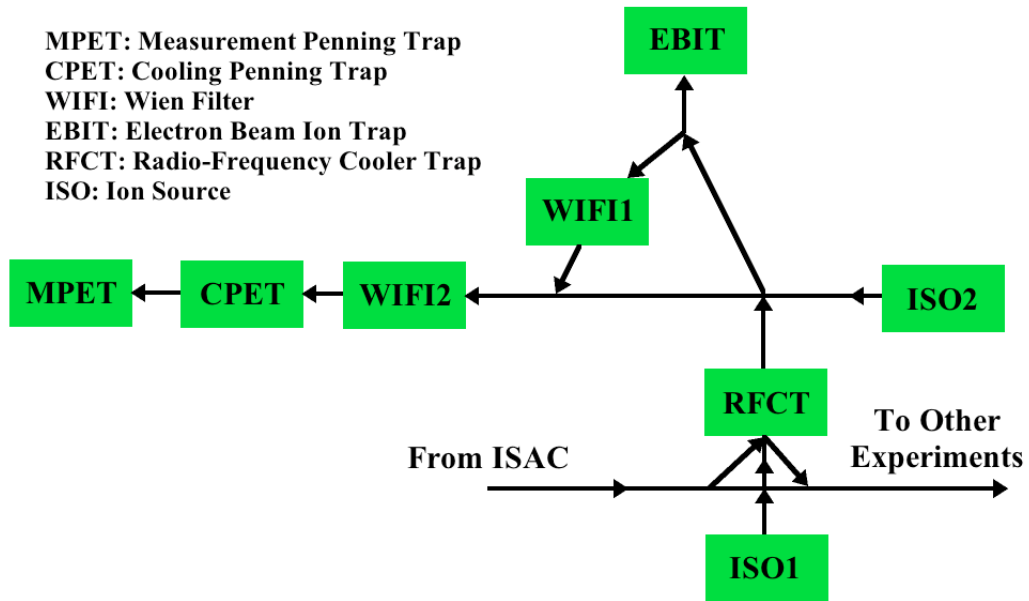


Figure 1.2: Schematic layout of the TITAN experiment.

The RFCT's purpose is to receive a 30-60 keV ISAC beam, cool it via collisions with a neutral buffer gas, and convert it to a bunched beam at a given energy of up to 5 keV, similar to devices at ISOLDE [45] and IGISOL [79]. This is accomplished by

using RF quadrupole fields to radially confine the ions while a longitudinal electric field pulls the ions through the buffer gas.

Simulations including the injection and ion deceleration efficiencies indicated that the TITAN RFCT could reach values of almost 100% [90], and experimental tests confirmed that a value around 90% [14] can be achieved. Ion injection and trapping using a buffer gas in the RFCT was already successfully demonstrated at voltages of up to 5 kV, with future plans to reach 60 kV [14]. The introduction of the buffer gas for cooling typically increases the beam size, but applying RF fields to the trap's electrodes assists in the confinement of the beam by guiding the ions toward the center of the trap. To test the emitted beam and the device's optimal cooling parameters, an emittance meter was used, roughly agreeing with simulated results with an experimental emittance of 7π mm mrad at an extraction energy of 5 keV [14, 28].

A unique aspect of the TITAN RFCT compared to other radio-frequency quadrupole (RFQ) devices is the ability to accept ions with a large range of mass-over-charge ratios. Such an ability is necessary for the acceptance of light to heavy ions that will be produced by ISAC. This is accomplished by using a square-wave RF driver, which allows the setting of the desired frequency and amplitude as needed for the injected species as opposed to using sine-waves in a tuned circuit for a specific range of ratios. Detailed information about this device can be found in [14, 90].

After an ISAC beam is cooled and bunched by the RFCT, it can be injected into the TITAN EBIT, which is the focus of this work and hence is discussed in greater detail below. In the EBIT, the ions are successively ionized to higher charge states, after which they are extracted, and the desired ions are separated from the rest by passing through a Wien filter. Such a device uses crossed magnetic and electric fields to deflect ions with non-desired mass-over-charge ratios and not allow them to pass. The Wien filters for the TITAN experiment have an m/q resolving power of 400, i.e. can separate species with ratios that differ by 1/400. This should allow them to effectively

1.2. Overview of the TITAN Setup

select the desired charge state from the distribution of charge states produced by the EBIT and other ionized background gas and cathode material contaminants.

After the beam has been filtered to selected the isotope and charge state of interest, it enters the CPET. This Penning trap is required for ion cooling as the resulting thermal energy of the ions after extraction from the EBIT is expected to be higher than that required for precision mass measurements (around $1 \text{ eV}/q$ where q is the charge state of the ion). McDonald *et al.* [73] from the Lawrence Livermore National Laboratory published results stating that ion thermal energies in an EBIT are mainly determined by the applied trapping potential V_{well} [eV],

$$k_B T_{\text{ion}} \approx 0.1q V_{\text{well}}, \quad (1.3)$$

where k_B is Boltzmann's constant, q is the charge of the ion, and T_{ion} is the temperature of the ion. These results were based on simulations by Penetrante *et al.* [82], estimating the temperature of the ions¹. Ion temperatures after extraction from the EBIT using a modest trap depth of only 100 V, however, are still too high ($10 \text{ eV}/q$) for precision measurements. Therefore, assuming that Equation 1.3 gives a rough estimate for the temperature of extracted ions from the TITAN EBIT, it is clear that cooling will be necessary. The typical cooling method, however, which employs a buffer gas to slow down ions through collisions, would result in prohibitively large charge exchange losses. Thus, a new technique is required for the cooling of highly charged ions. Currently,

¹It should be noted that the published computer simulated data can vary from this estimate by almost a factor of 4. McDonald *et al.* [73] also drew upon experimental results from Beiersdorfer [8] to confirm this relationship between the trap depth and the ion temperature. When this relationship is compared to results by Lapiere *et al.* [57] at the Heidelberg (HD) EBIT, with ion temperatures of Ar^{13+} ($k_B T_{\text{ion}} = 350 \text{ eV}$) determined from the Doppler width of a spectral line, the formula above would suggest the applied trapping potential was 270 V as opposed to the actual applied trap potential of 1.5 kV. This difference, however, can be accounted for by considering the space charge of the positive ions in the trap (see Section 3.2.6), which was not included in the published analysis [64]. Other factors, which are usually smaller, can also affect the ion temperature, such as the electron beam current [69].

the use of sympathetic cooling via the Coulomb interaction with a cold ensemble of electrons, positrons, or light ions is being studied for use in the TITAN cooling Penning trap.

Finally, when the ions have been sufficiently cooled in the CPET, they are injected into the precision Penning trap mass spectrometer. Penning traps are widely used, and it has been demonstrated that they can be the most precise devices presently known to measure the mass of ions [16]. The TITAN MPET has been designed to reach an accuracy of $\delta m/m \leq 10^{-8}$ using radionuclides with half lives below 50 ms [27]. In a Penning trap, determination of the mass m is accomplished by measuring the cyclotron frequency ν_c of the trapped ion(s) experiencing a homogenous magnetic field of magnitude B , orbiting inside the trapping region:

$$m = \frac{qB}{2\pi\nu_c}. \quad (1.4)$$

The relative uncertainty in determining the mass m is given by [27]

$$\frac{\delta m}{m} \approx \frac{m}{TqB\sqrt{N}}, \quad (1.5)$$

where T is the excitation time in the Penning trap, q is the charge of the ion of interest, and N is the number of measurements. A more thorough treatment of the relative uncertainty can be found in [15, 22].

When studying short lived isotopes, only very small excitation times are possible and large production rates of each species may not be practical, thus severely limiting the accuracy to which these ions can be measured. If one takes advantage of the charge breeding capabilities of the EBIT to increase the charge q of the isotopes, one can compensate for these disadvantages during the mass measurement process. Higher charge states of longer-lived and easily produced isotopes give the TITAN project

an additional advantage in precision for some species over other mass measurement experiments which typically use singly or doubly charged ions (for example the Canadian Penning Trap [21] and SMILETRAP [44]). It should be noted, however, that one Penning Trap, namely SMILETRAP, has successfully measured cyclotron frequencies of stable highly charged ions (up to Cs^{42+}) bred in an attached Electron Beam Ion Source (EBIS) [20].

1.3 General EBIT Experimental Setup

An EBIT relies on a beam of electrons that collide with trapped ions, resulting in the step-wise ionization and production of highly charged ions (see Figure 1.4). As the rate of these collisions can be increased by creating a higher density of electrons (see Section 2.2), the beam is compressed using a strong magnetic field.

Optimal beam compression is achieved by situating the heated cathode, producing the electrons, in a magnetic field-free region. As the electrons are pulled towards the trap, the magnetic field strength increases, compressing the field lines which define the area in which the electrons can move (see Figure 1.3). As the magnetic field is greatest

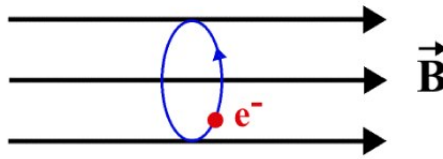


Figure 1.3: Schematic of magnetic field lines defining the area in which an electron can orbit.

in the trapping region, it is here where the highest electron beam compression occurs. For additional details about why the flux contained within an electron's cyclotron orbit must remain constant, using the adiabatic invariance of flux in a magnetic field, see Jackson [49]. Therefore, increases in the magnetic field produced by two

superconducting magnetic coils in a Helmholtz-configuration (up to 6 Tesla) result in a decrease of the electron beam's radius to around $30\ \mu\text{m}$. This reduction of the electron beam radius combined with high beam currents (5 A) can create electron current densities of around $40,000\ \text{A}/\text{cm}^2$.

Applying electrostatic potentials to the trap electrodes confines the ions axially, while the space charge of the electron beam and the magnetic field confine the ions radially. The electron beam successively ionizes the trapped ions that have electrons with an ionization energy less than the energy of the electron beam. After interacting with ions in the trap, the electron beam is expanded and decelerated before it is dumped on the collector electrode. As the beam approaches the collector, the magnetic field decreases, allowing the electron beam to expand. A so-called collector coil (not shown) produces a small magnetic field in the collector, which assists in the expansion of the electron beam. The collector electrode is set to the same potential as the cathode, allowing it to absorb the electrons with minimal heat deposition. While secondary electrons may be produced during this absorption process, electrodes on either end of the collector prevent them from escaping the EBIT system and help to keep them from returning to the trap. The produced heat from the electron impingement in the collector is removed via water cooling.

While the main purpose of EBITs thus far has been to trap ions for spectroscopy, whether that be in the optical or the hard x-ray region, the TITAN EBIT has been designed for charge breeding. Therefore, while its design will allow beam energies of up to 60 keV (high enough to produce He-like uranium), the primary goal is to produce an EBIT with a maximum electron beam current (up to 5 A) to quickly and efficiently breed ions to high charge states for mass measurement in a high precision Penning trap.

The TITAN EBIT (see Figure 1.6) was designed and constructed alongside the TESLA EBIT [66] at the Max-Planck-Institute for Nuclear Physics (MPI-K) in

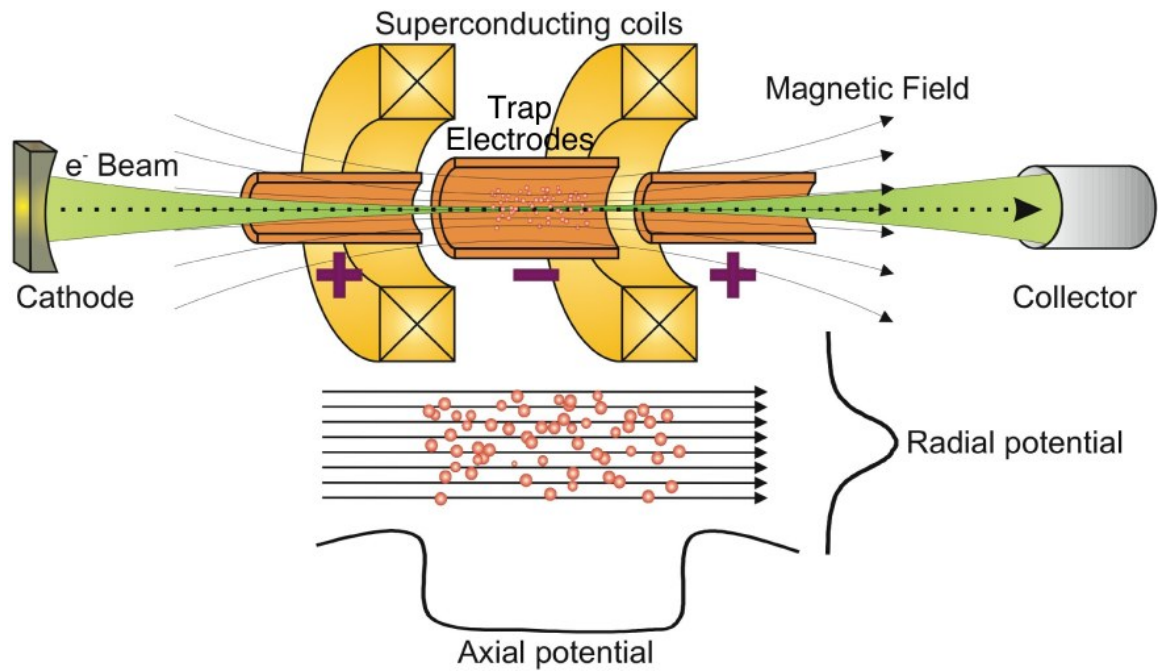


Figure 1.4: Basic principles of an electron beam ion trap (modified from [18]). An electron beam is created by a heated cathode, accelerated towards the trap electrodes, collides with the trapped ions stripping off electrons, then decelerated and absorbed by the collector electrode. Two superconducting magnetic coils in a Helmholtz-configuration compress the electron beam to a radius of around $30 \mu\text{m}$, increasing the electron density and the ionization rate of the trapped ions. The electrostatic force due to the space charge potential of the electron beam confines the ions radially, while the trap electrodes provide an electrostatic well-shaped potential for axial trapping.

Heidelberg, Germany after design work began in 2003. Many essential elements, such as the electron gun and the collector, are upgrades of the corresponding Heidelberg (HD) EBIT elements. The TESLA EBIT was designed to be a transportable EBIT, enabling it to be utilized in experiments at other facilities such as the Deutsches Elektronen-Synchrotron (DESY) in Hamburg, Germany with the VUV free electron laser (FEL), and to achieve electron beam energies of over 80 keV.

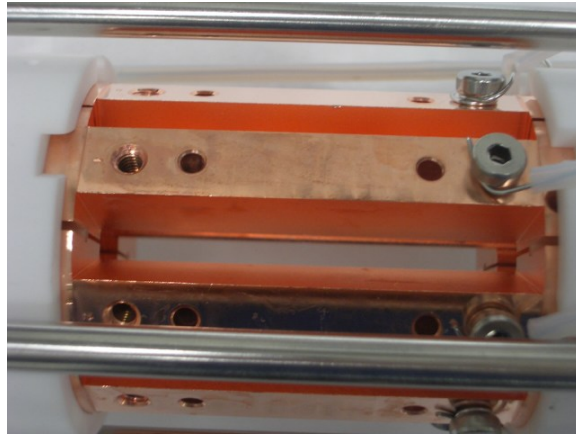


Figure 1.5: Photo of the eight-fold radially segmented central trap electrodes.

While both the TESLA and TITAN EBITs have a similar design, only the TITAN EBIT has radially segmented central trap electrodes (see Figure 1.5). This central trap is comprised of sixteen independently controlled electrodes, eight of which constitute a radially segmented octupole trap, which has a series of slits cut into it that act as viewports for photon detection. This azimuthal segmentation, which has been implemented in other types of ion traps, has been introduced here for the second time in an EBIT. A lower order segmentation (four-fold) combined with two additional cylindrical trap electrodes has recently been built into the Tokyo EBIT [78]. The TITAN EBIT's higher order octupole trap will allow a wide range of options, only one of which has already been attained using EBITs (see Section 3.1.2 for information on RF excitation, resistive cooling, and measuring and moving charge distributions inside

the trap). On either side of the segmented trap electrodes there are four cylindrical electrodes, which allow further variation of trap length and shape. For increased ion control, two sets of ion optic lenses are also placed on either side of the collector. This should allow for optimal transfer to and from the rest of the TITAN experiment.

The HD EBIT, as well as these two new EBITs, all have a horizontal beam axis, lending themselves to simpler ion transfer and extraction to external experiments than previous EBITs with vertical beam axes. The new EBITs also include a closed-cryogenic-helium system that avoids the awkwardness and inefficiency of liquid helium refilling. Both new EBITs also employ thermal coupling of the 6 Tesla superconducting magnet cold head at about 4 K to the trap electrodes and support structure to provide additional cryogenic pumping. This improvement should create excellent vacuum conditions in the trapping region around an estimated pressure of 10^{-13} mbar, thereby minimizing the losses of highly charged ions by charge-exchange (see Section 2.2.4).

1.4 EBIT History

The use of an electron beam to ionize and trap ions was first employed in the electron beam ion source (EBIS), invented by Donets in 1965 in Dubna. Four years later, using a vacuum tube inside an ordinary conducting solenoid, Donets demonstrated the production of bare nitrogen and Au^{19+} [31]. Improvements were made, including the implementation of a superconducting solenoid and drift tubes (trap electrodes) at cryogenic temperatures, allowing KRYON-II to become the first EBIS to produce bare Ne, Ar, Kr, and Xe ions [29]. EBIS development continued to increase, as more of these devices were typically built to provide intense ion beams for large accelerators and colliders, such as the Large Hadron Collider (LHC) at CERN or the Relativistic Heavy Ion Collider (RHIC) at Brookhaven National Laboratory.

At the same time, atomic physics experiments began constructing and using EBIS

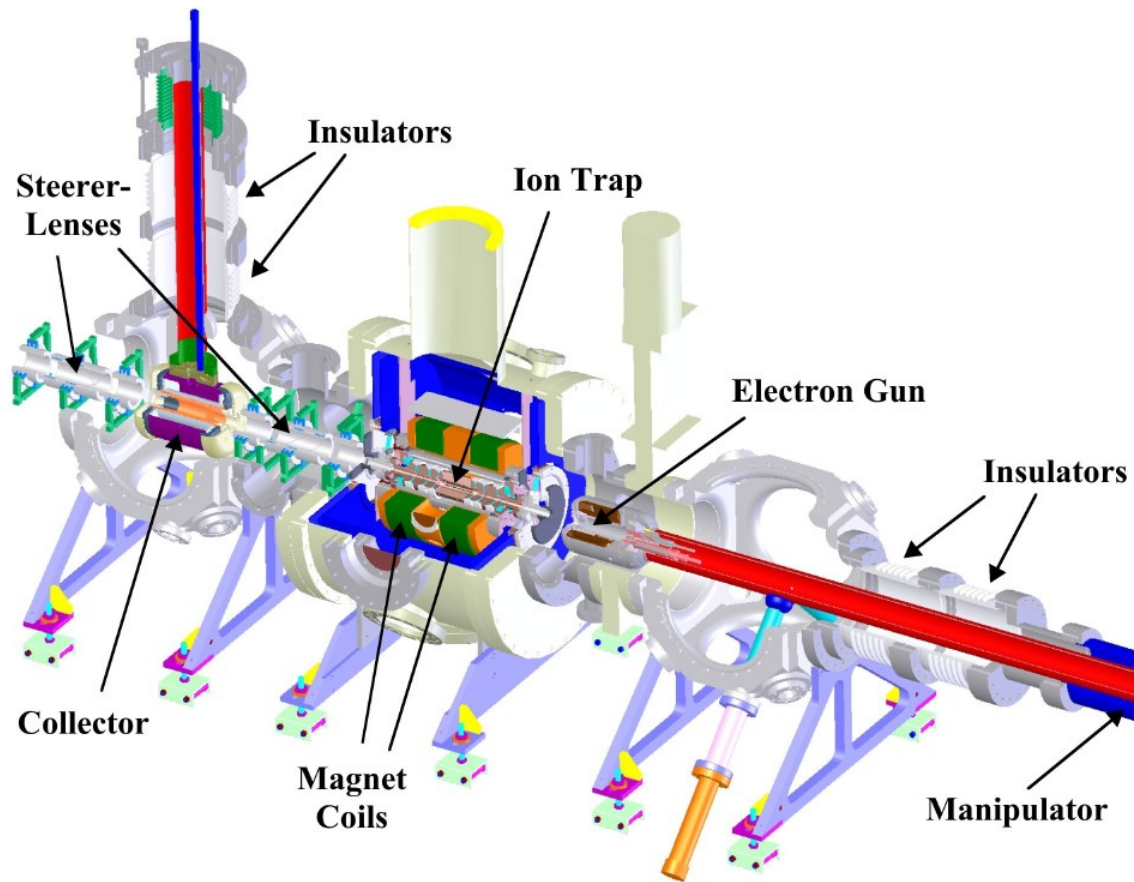


Figure 1.6: Labelled cross-sectional TITAN EBIT overview.

devices in laboratories around the world. It was proposed by Litwin *et al.* [63], based on extensive experience with the Berkeley EBIS, that this typical long electron beam path tends to induce plasma instabilities. A few years later the first EBIT was constructed by Levine *et al.* [61] at Lawrence Livermore National Laboratory (LLNL), using an EBIS design with a shorter electron beam path (with a trap length of ≈ 10 mm instead of typically 1 m in an EBIS [30]) and a pair of coils in a Helmholtz-configuration replacing the solenoid. A new device was later made with various improvements to reach electron beam energies of 200 keV and beam currents up to 200 mA, allowing it to reach the goal of producing bare uranium ions [68] (the required ionization energy

Table 1.1: Summarized properties of selected EBITs.

EBIT	Electron beam properties	
	Electron energy	Electron current
SuperEBIT	200 keV	0.25 A [64, 68]
HD EBIT	100 keV	0.53 A [64, 65]
TITAN EBIT	60 keV	5 A
TESLA EBIT	80 keV	0.5 A [64]
low energy EBITs	≈ 30 keV	≈ 0.25 A [13, 50, 61, 81, 92]
high energy EBITs	≈ 100 keV	≈ 0.2 A [25, 95]

to produce U^{92+} is 132 keV [3]), after which this second EBIT was renamed the *Super-EBIT*.

Additional EBITs were built using the original low energy LLNL design at the National Institute of Standards and Technology (NIST) [38] and at Oxford University [89]. This design was further modified, yielding the Berlin EBIT [13]. A second high-energy EBIT (HD EBIT), designed to reach beam energies of 350 keV and currents up to 750 mA was then built in Freiburg and now resides at the Max-Planck-Institute for Nuclear Physics (MPI-K) in Heidelberg, Germany [65]. Numerous EBITs have since been built, the properties of which have been summarized for comparison in Table 1.1, including the two newest EBITs; the TESLA and TITAN EBITs commissioned in 2005 and 2006 at the MPI-K.

Chapter 2

Theory

2.1 Charge Breeding and Charge Breeding Devices

As TITAN will use highly charged ions for high precision mass measurements with a wide variety of isotopes, including those produced by ISAC with short half-lives, the charge breeding process must be fast and efficient. Currently two charge breeding methods are available, both of which are capable of creating highly charged ions (HCIs), namely the Electron Cyclotron Resonance (ECR) ion source (also abbreviated as ECRIS) and the Electron Beam Ion Trap (EBIT) or Source (EBIS).

An ECR ion source employs a vacuum chamber in which microwaves and a magnetic field are applied to create regions where electrons can efficiently absorb the injected microwave energy. The electrons are then stochastically heated up to the keV range but are still trapped by the surrounding inhomogeneous magnetic field. A hot plasma is thus created, where these excited electrons collide with the atomic electrons of the ions present in the plasma, ionizing them to high charge states.

The basic operation principles of an EBIS/T, as described in Section 1.3, also involve high energy electron collisions to strip off atomic electrons in a step-wise fashion. However, this is accomplished with a magnetically compressed electron beam

interacting with electrostatically trapped ions.

The difference between an EBIT and an EBIS lies in the goal for *in situ* observations of x-rays from highly charged ions, and the resulting physical differences of trap length and the magnet configuration. An EBIS magnet typically consists of a single, long, closed solenoid surrounding the trap electrodes through which the electron beam passes, ionizing the trapped ions. EBIS devices are typically longer (0.8 m at REXEBIS [51], 1.5 m at RHIC EBIS [6]), which, while allowing them to hold more charged particles in a given volume and produce a higher flux of ions, leads to increased plasma instabilities [60]. To avoid these instabilities, an EBIT has a shorter trap length (2 cm at the LLNL SuperEBIT [69], 4 to 20 cm at HD EBIT [72]), which is typically surrounded by a pair of superconducting coils in Helmholtz configuration that produce a magnetic field. The split magnet, when combined with slits or windows cut in the central trap electrode(s), allows the observation of emitted photons. The shorter trap lengths also allow EBITs to more easily employ greater magnetic compression of the electron beam, allowing them to achieve higher electron densities and therefore, higher ionization rates (see Section 2.1.2 for examples and further discussion).

2.1.1 Charge Breeding Efficiency

The efficiency of the charge breeding process is important, when recalling that higher charged ions result in higher mass measurement accuracy in a Penning trap. The goal, therefore, is to produce the highest charge states possible in a short breeding time (given by the isotope's half-life) and at a given rate (determined by the efficiency of extracting ions and successfully capturing them in the mass measurement Penning trap).

For this reason, the inherent limitation on the charge states that can be produced in an ECR is a disadvantage for TITAN's purposes. As discussed by Becker [4], current

2.1. Charge Breeding and Charge Breeding Devices

ECR sources are limited in producible high charge state abundances by radiative recombination and charge exchange. This is due in part to their typical vacuum pressures of around 10^{-7} to 10^{-8} mbar [4,47] both in the source and during subsequent charge state and mass selection [1]. These vacuum pressures containing high levels of background ions, are due to the ionization of residual gas and the support gas used in an ECR [1]. These pressures result in losses of higher charge states due to charge exchange. Using Pb ions as a sample heavy ion, Becker [4] produced Figure 2.1, which plots the vacuum pressure at which ionization gains in charge state equal the rate of charge state losses via charge exchange. It illustrates that while higher current densities can help during the production of higher charge states at higher pressures, the background pressure, through charge exchange interactions, dramatically effect the charge states that can be produced. It should be noted that this figure is device independent and only illustrates the general relationship between the vacuum pressure and charge exchange losses. Although this graph does not consider such factors as radiative recombination, which would further reduce ionization gains in both ECRs and EBIS/Ts, it does illustrate the need for high vacuum in a device used for charge breeding.

Further restricting the charge states that can be produced is the presence of a large range of electron energies in an ECR. While some electrons can have energies much higher than typically found in an EBIS/T, there are also many lower energy electrons which negatively affect the balance between ionization and radiative recombination (RR). These effects lead to a limitation on the maximum producible charge states [4]. Similar to the graph above, Becker produced Figure 2.2, which displays the electron energy at which a balance between ionization and radiative recombination exists for Pb ions. Again, this figure is device independent, and note that both electron impact ionization and radiative recombination scale linearly with electron density (see Equation 2.1).

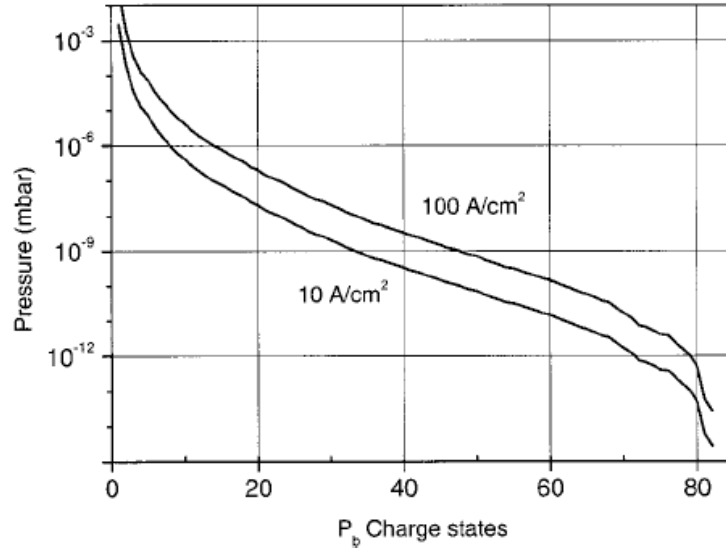


Figure 2.1: Vacuum pressure at which charge state gains due to ionization equal charge exchange losses in Pb ions [4]. As it is advantageous to use the high charge states produced by the TITAN EBIT for mass measurement precision enhancement, lower vacuum pressures are required and rule out using an ECR ion source. Reprinted with permission from R. Becker, *Rev. Sci. Instr.*, 73, 693, 2002. Copyright 2002, American Institute of Physics.

In comparison to ECR sources, EBIS/Ts typically have lower vacuum pressures in the ionization region. The vacuum pressure, for example, in the magnet chamber containing the EBIT trap electrodes is about 10^{-10} mbar for the Heidelberg EBIT and 2×10^{-9} mbar for the TITAN EBIT. In these traps, however, the magnet, trap electrodes, and trap support structure all act as cryogenic pumps when cooled to 4 K, producing a vacuum pressure in the trapping and ionization region that is estimated to be less than 10^{-13} mbar. As for the energy spread of the ionizing electrons, the electron beam in an EBIS/T is almost mono-energetic, which produces a more advantageous balance between ionization and radiative recombination as demonstrated in Figure 2.2. In an ECR, the large energy spread of electrons results in greater radiative recombination rates, limiting the abundance of higher charged states [4].

Considering the limitations placed on effective high charge state production via

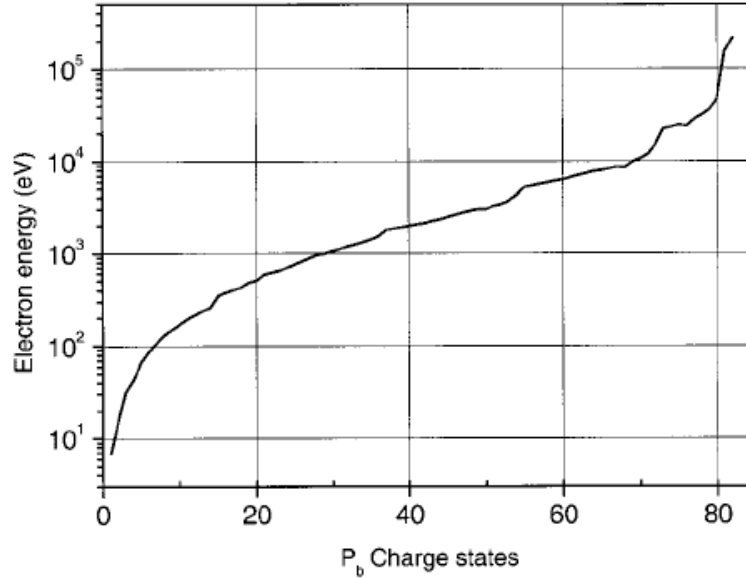


Figure 2.2: Electron energy at which charge state gains due to ionization are equal to radiative recombination losses in Pb ions [4]. This graph demonstrates that having an almost mono-energetic electron beam at high energies will produce the highest charge states with as little RR loss as possible. Such losses are to be avoided for fast and efficient charge breeding and therefore exclude the use of an ECR as a charge breeder for the TITAN project. Reprinted with permission from R. Becker, Rev. Sci. Instr., 73, 693, 2002. Copyright 2002, American Institute of Physics.

step-wise ionization in ECR sources by charge exchange and RR, it is concluded that an ECR source would not be ideal as a charge breeder for TITAN.

High efficiency is also required for the extraction of highly charged ions to the rest of the TITAN system. This requires the transfer of ions from the TITAN charge breeder with minimal losses, which corresponds to a device that can produce a small beam with little divergence. These beam qualities can be characterized in the form of a quantity called an emittance ϵ . It can be defined as $\epsilon = \pi r r'$, where r is the radius of the beam at a specific axial point and r' is the beam's divergent angle from this radius [69]. The emittance is then the area of the ellipse in phase space, which has axes of length $2r$ and $2r'$, where this area remains constant in a conservative potential. A narrow, well defined beam with little divergence, therefore, has a small emittance.

When comparing the available options, an extracted ion beam from an EBIT has the lowest measured emittance of the possible devices with around $1 \pi\text{mm mrad}$ at the LLNL SuperEBIT using 20 keV Xe^{44+} ions [73]. An EBIS also has a small emittance such as the REXEBIS at ISOLDE, which measured less than $15 \pi\text{mm mrad}$ at 5 keV for various measured ionic species [51]. Finally, for completeness, the PHOENIX ECRIS at TRIUMF has a measured emittance of less than $30 \pi\text{mm mrad}$ at 15 keV [1]. Therefore, based on extraction efficiency through emittance, an EBIT or possibly an EBIS appears to be the best option as the charge breeder for precision mass measurements with TITAN.

2.1.2 Charge Breeding Speed

Since ionization rates are linearly proportional to the electron charge density in an EBIS/T, the breeding time of HCIs is inversely proportional to the electron charge density (see Section 2.2). A faster breeding time would allow the production and mass measurement of highly charged ions of shorter lived radioisotopes, thereby establishing the need for a device with the most efficient ionization rates. As mentioned above, the magnetic configuration of an EBIS translates into less beam compression and therefore, smaller current densities such as 500 A/cm^2 at Brookhaven National Laboratory's EBIS Test Stand (EBTS) [7] and $150\text{-}200 \text{ A/cm}^2$ at ISOLDE's REXEBIS [52]. In comparison, EBITs such as LLNL's SuperEBIT have maximum beam current densities on the order of $10,000 \text{ A/cm}^2$ [73] and both the TITAN and TESLA EBITs have measured current densities of up to $15,000 \text{ A/cm}^2$ [64]. As described in greater detail in Section 3.2.5, assuming electron beam currents of up to 5 A, the TITAN EBIT will be able to achieve current densities of around $40,000 \text{ A/cm}^2$. In light of these current densities and their corresponding charge densities and higher ionization rates, the ideal charge breeder for the TITAN experiment is an EBIT.

2.1. Charge Breeding and Charge Breeding Devices

Table 2.1: Some ionization values of high Z elements included in the charge breeding time simulations [3].

Element and charge state	Ionization energy (keV)
He-like Xe ⁵²⁺	40.270
He-like Au ⁷⁷⁺	91.515
Li-like Pb ⁷⁹⁺	24.938
Neon-like U ⁸²⁺	25.260

It should also be noted that for all three possible devices considered for charge breeding, m/q selection must also be performed on the extracted ions. This process is required to separate ionized residual gas, contaminants from the system (i.e. cathode materials in the case of the EBIT), and other charge states from that which is desired for mass measurement. This will be done in the TITAN experiment via the use of a Wien filter system (resolution power around 400), which employs crossed magnetic and electric fields for m/q selection. Only the species with the desired m/q ratio will pass through the device to the cooling Penning trap and the precision Penning trap.

Theoretical modeling of some charge changing processes in an EBIT was performed using a code developed by Becker [5] in a program called SUK. This program uses ionization cross sections from Lotz's formula (see Equation 2.3) and radiative recombination cross sections from Thomas Stoeckler [5]. These RR cross sections produce similar values as those from Kim and Pratt [53]. Parameters such as the electron beam energy E_e and the species to be ionized are specified by the user. Using the program's default settings (500 integration steps and no constant neutral atom influx) while turning radiative recombination on and specifying an electron beam energy of 25 keV, plots such as Figure 2.3 were produced for each element. The log of the current density multiplied by the time was recorded when the given charge state reached its maximum value. To estimate the time needed for charge breeding from this value, a mid-range current density of 25,000 A/cm², which could be produced

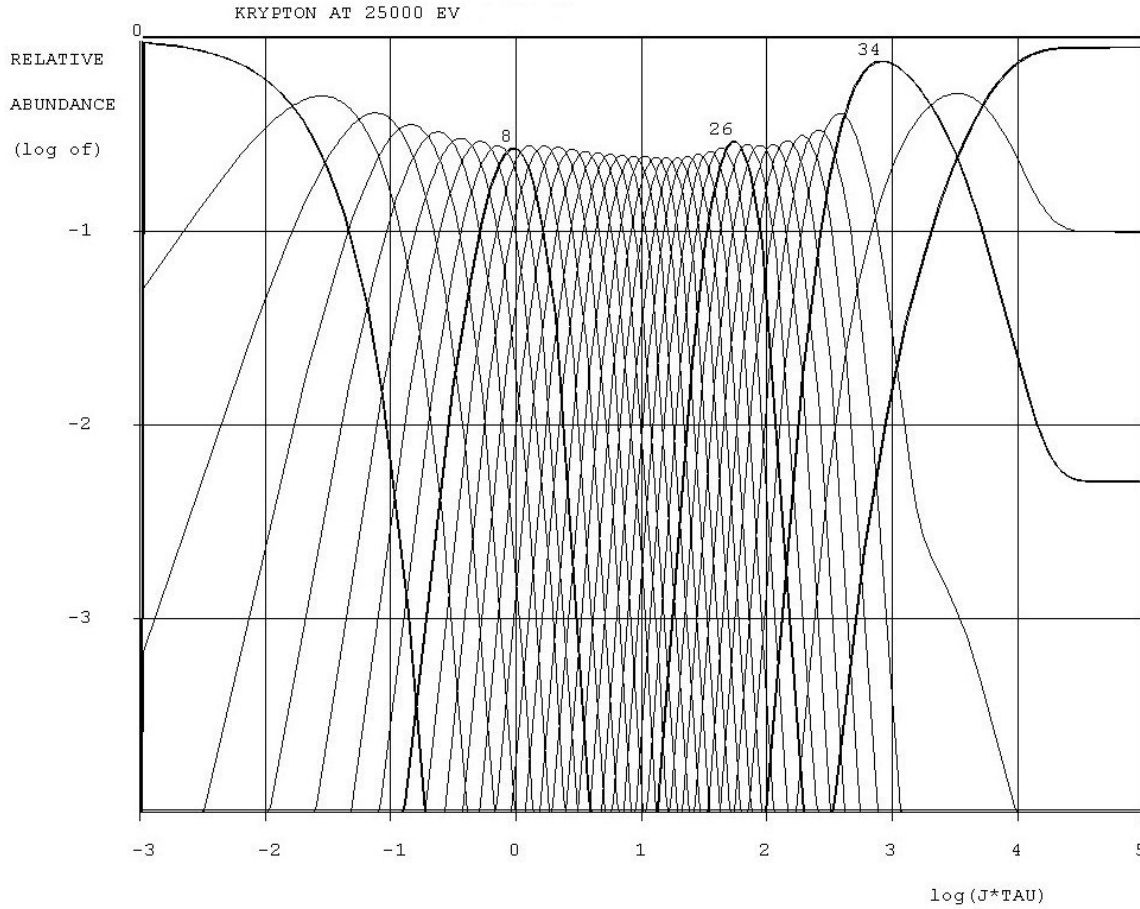


Figure 2.3: Charge breeding simulation for Kr based on EBIT theoretical modeling with RR using the SUK program developed by Becker [5]. The percentage of population is plotted with respect to the log of the electron current density J (A/cm^2) and the time τ (seconds). In addition to step-wise ionization from electron collisions, radiative recombination is also included in this simulation, altering the populations of the higher charge states after sufficient breeding time.

from either of the two larger TITAN EBIT cathodes, was used (see Section 3.2.5 for further discussion). The resulting simulated charge breeding times for the sample ions included in the SUK program are shown in Figure 2.4 for low Z elements and in Figure 2.5 for high Z elements.

To assist in understanding the high Z element charge breeding times, the ionization values of the next charge state (if one exists) are given in Table 2.1. It is clear that a

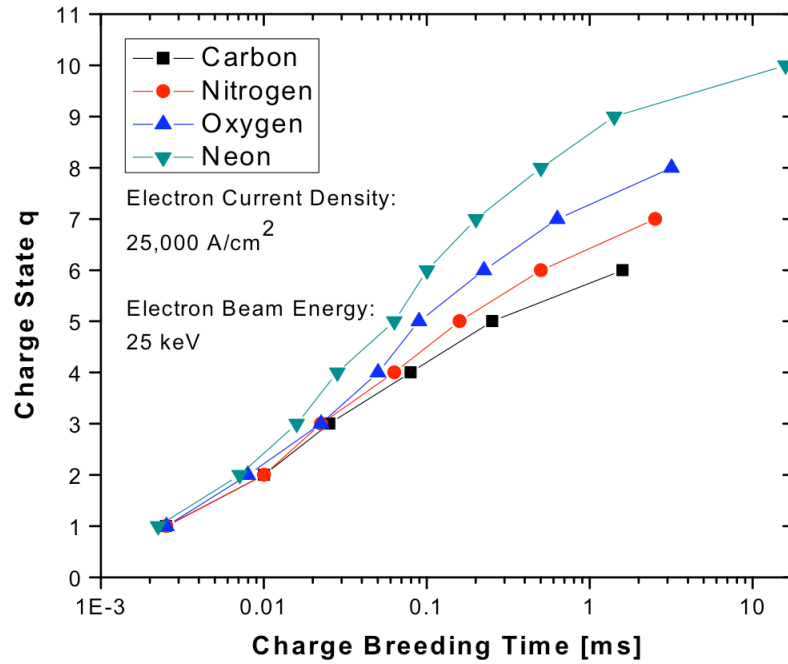


Figure 2.4: Charge breeding times of low Z elements based on EBIT theoretical modeling using the SUK program developed by Becker [5]. The charge state of various elements is plotted as a function of the breeding time in the TITAN EBIT with a current density of 25,000 A/cm².

beam energy of 25 keV is not sufficient to yield charge states beyond Ne-like U. From Figure 2.5, it is clear that the removal of the most tightly bound electrons requires more time in all simulated species, assuming the electron beam energy is high enough to create He-like and bare charge states. This can be seen in more detail in the Kr simulation data in Figure 2.3, as the peak populations of H-like and bare states require more time than the closely spaced mid-charge states. This trend was consistently observed for all of the simulated elements. A beam energy of 25 keV is high enough to produce He-like Au and Li-like Pb. He-like Pb was not created as the simulated RR prevented the population of Li-like Pb from comprising more than about 0.1% of the charge states. Similar conditions prevented Ne-like U from being created in the simulation. While Kr appears to have required more breeding time than Xe, the charge states reached (bare Kr and He-like Xe) clarifies this situation.

When simulations with and without radiative recombination are compared, the charge breeding times (when the maximum relative population for a given charge state was reached) remain almost unchanged. The relative population levels, however, for He-like and higher charged states, are significantly altered when RR is included (see Figure 2.3 with RR and Figure 2.6 without RR). A future version of this program is planned with additional options and the ability to include other charge changing processes such as charge exchange.

2.2 Primary Reactions in an EBIT

To understand the spectroscopic results which allow the determination of the reactions occurring in the trapping region of an EBIT, a review of five processes, namely electron impact excitation (EIE) and ionization (EII), dielectronic recombination (DR), radiative recombination (RR), and charge exchange (CX) is required. Other processes which can also occur in an EBIT, such as ion-photon collisions and the loss

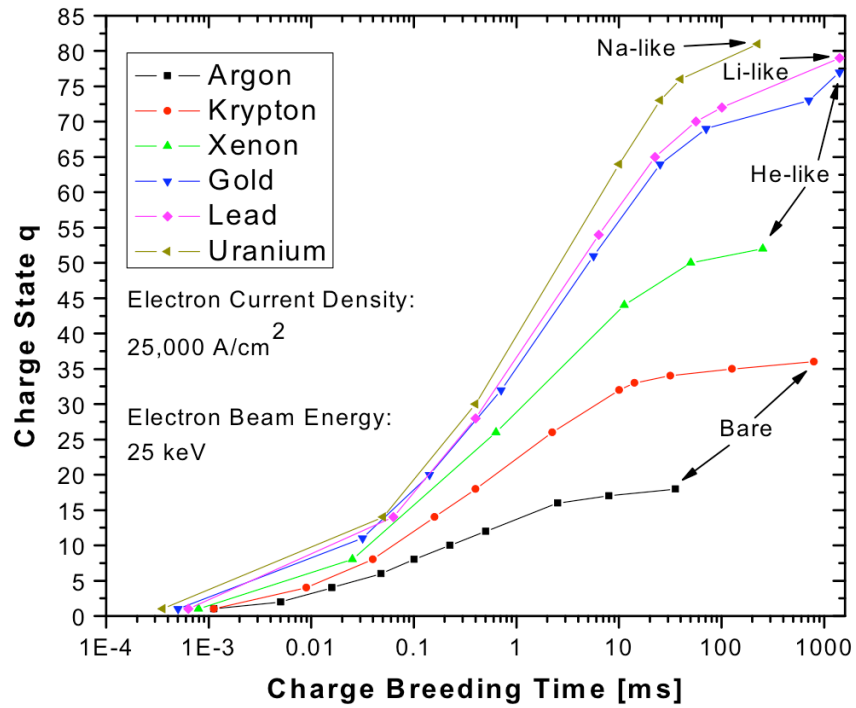


Figure 2.5: Charge breeding times of high Z elements based on EBIT theoretical modeling using the SUK program developed by Becker [5]. The charge state of various elements is plotted as a function of the breeding time in the TITAN EBIT with a current density of 25,000 A/cm².

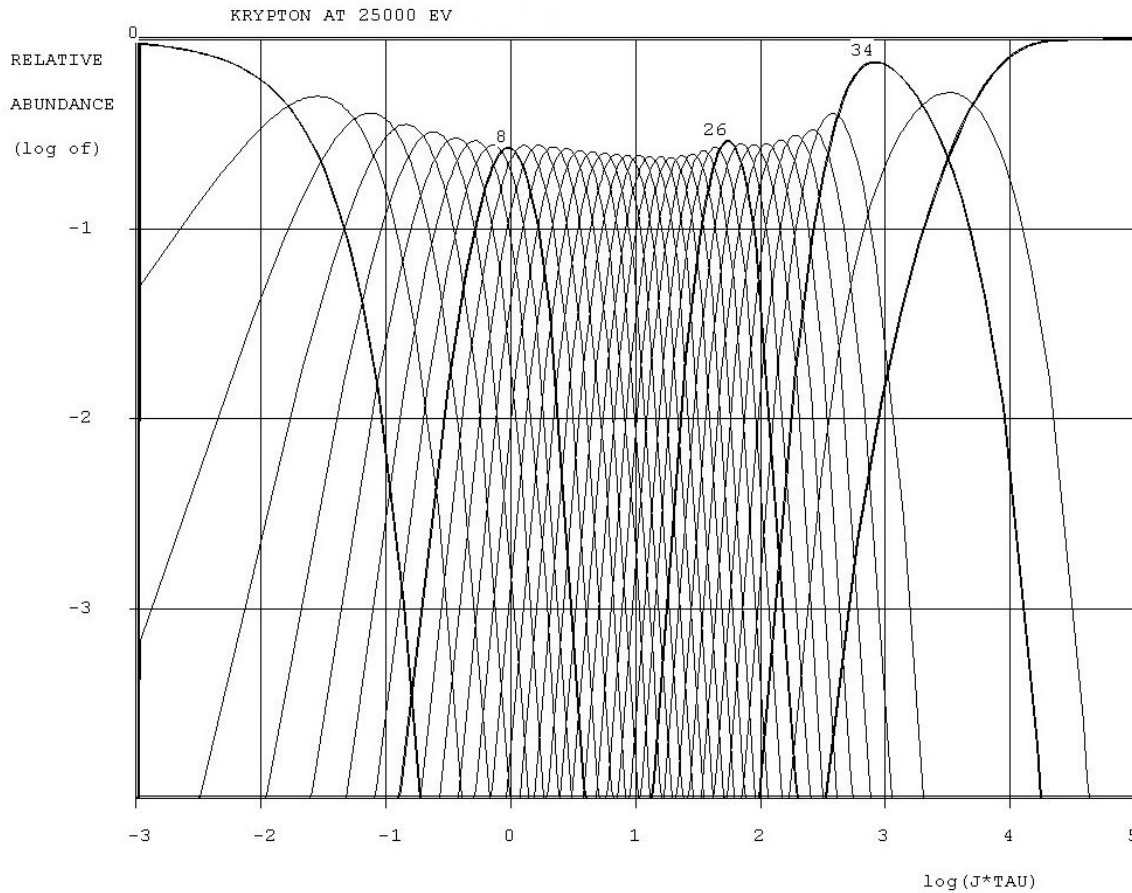


Figure 2.6: Charge breeding rates for Kr based on EBIT theoretical modeling without RR using the SUK program developed by Becker [5]. This graph was produced using the default simulation settings where step-wise ionization due to collisions with high energy electrons occurred. The percentage of population is plotted with respect to the log of the electron current density J (A/cm^2) and the time τ (seconds).

of heated ions due to Coulomb collisions, will not be discussed here.

Consider bound electrons in their different quantum mechanical orbits. When all of the atomic electrons have collectively filled all the lowest energy states, the atom or ion is said to be at ground state. The lowest atomic energy levels contain the most tightly bound electrons and therefore have the highest ionization energies. To clarify spectroscopic notation, Figure 2.7 illustrates various labelled shells in an atom which

2.2. Primary Reactions in an EBIT

electrons can occupy. The primary quantum number n , is shown for each level as well as the alternative letter label for the orbit. In heavy atoms, the energy difference between these shells increase, such that electronic transitions between these levels produce characteristic x-rays, the historical labelling of which is also displayed.

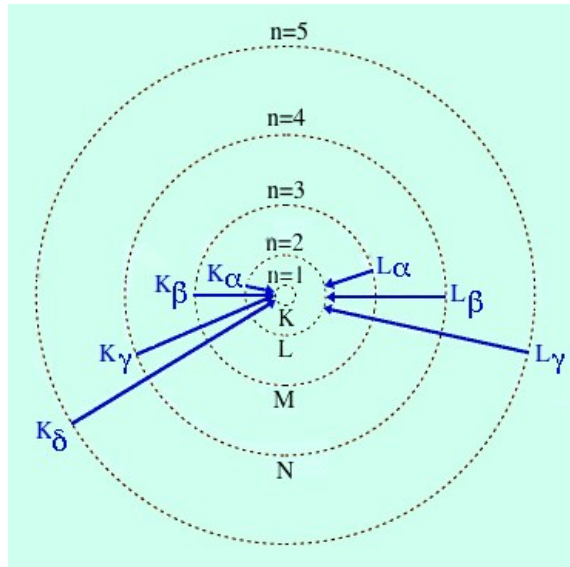


Figure 2.7: Atomic shells in an atom with some characteristic x-ray transitions between these levels. The de-excitation of atomic electrons from higher orbits to vacant lower orbits yields a radiated photon, which for highly charged heavy ions, has an energy in the keV range.

Moving on to the five processes listed above which can take place in the trapping region of an EBIT, it is useful to examine a complete set of differential equations, which describe the population of a given trapped isotope. The population of any ion with a charge state i in an EBIT, taking into account ionization, radiative recombination, dielectronic recombination, and charge exchange, can be given by the following complete set of differential equations:

$$\begin{aligned}
\frac{dn_i}{dt} = & n_e v_e [\sigma_{i-1 \rightarrow i}^{\text{EII}} n_{i-1} - (\sigma_{i \rightarrow i+1}^{\text{EII}} + \sigma_{i \rightarrow i-1}^{\text{RR}} + \sigma_{i \rightarrow i-1}^{\text{DR}}) n_i] \\
& + (\sigma_{i+1 \rightarrow i}^{\text{RR}} + \sigma_{i+1 \rightarrow i}^{\text{DR}}) n_{i+1}] \\
& - n_0 v_{\text{ion}} [\sigma_{i \rightarrow i-1}^{\text{CX}} n_i - \sigma_{i+1 \rightarrow i}^{\text{CX}} n_{i+1}]
\end{aligned} \tag{2.1}$$

The populations of the ion in successive charge states are given by n_{i-1} , n_i , and n_{i+1} . In the equation above, n_e and v_e are the density and velocity of the electrons, v_{ion} is the average thermal velocity of the ions, n_0 is the neutral gas density, and σ are the various cross sections for EII, RR, DR, and CX, which are described in their respective sections below. For a given charge state i , recombination from populations with a higher charge $i + 1$, also yields an increase in the population of charge state i . Note that with the exception of charge exchange, all other listed processes scale linearly with the electron density (three-body recombination involving two electrons and an ion can be safely neglected at the EBIT's high temperatures). Therefore, increasing the electron density when ionization rates are already higher than competing effects will result in a further increase in the ionization rate (maximizing $\frac{dn_i}{dt}$) and hence, a decrease in the required charge breeding time. For optimal charge breeding as already described above (see Section 2.1.1), the neutral gas density (determined by the background gas pressure) should be minimised to reduce charge exchange losses.

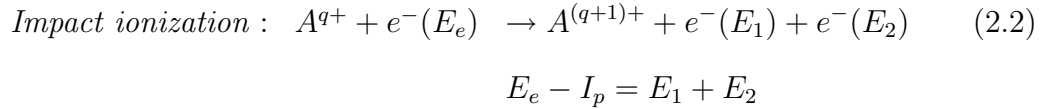
2.2.1 Electron Impact Excitation and Ionization

One of the primary interactions in an EBIT is electron impact (or collisional) excitation (EIE) and ionization (EII) occurring between the electron beam and the ions or neutral atoms in the trap. As these are among the most common processes with highly charged ions (HCIs) due to their production methods (see Section 2.1), electron impact excitation and ionization are well studied, with various thorough theoretical

2.2. Primary Reactions in an EBIT

calculations available (see [39] for further reading).

Considering first the basics of the ionization process, an electron with kinetic energy E_e , which exceeds the ionization energy or ionization potential I_p of the bound atomic electron, impacts this target electron, liberating it from the atom or ion (see Equation 2.2). By conservation of energy, the combined kinetic energies of these two scattered electrons after the collision must equal the kinetic energy of the incident electron minus the ionization energy of the bound electron.



As discussed previously, both ECR and EBIS/T type sources for highly charged ions rely on step-wise electron impact ionization. The rate of this process is determined by the cross section or effective area for such a collision to take place. These cross sections can then be used in the differential equations above (Equation 2.1), describing the populations of a given charge state in the trap region of an EBIT. To calculate the ionization cross sections for positive ions, which determine the rate of ionization, the semi-empirical Lotz formula is often employed [67]:

$$\sigma_{Lotz}^{ion}[cm^2] = 4.5 \times 10^{-14} N \frac{\ln(E_e/I_p)}{E_e I_p}, \quad (2.3)$$

where the electron energy E_e and the ionization energy I_p are in units of eV. This formula for describing the total cross section for ionizing any one of the N electrons in the same shell, with approximately the same ionization energy, yields accurate estimates for ions with few electrons.

For electron impact excitation to occur, an electron with kinetic energy E_e must strike

an ion with an incident energy larger than the threshold energy necessary to excite an ion from level n to level n' (see Equation 2.4). In this equation, A^{q+} represents an ion or atom with charge q , and the asterisk $*$ denotes an excited state. When such a process occurs, the excited ion is normally stabilized through the emission of a photon with a specific energy, a number of photons in a cascade, or by Auger processes.

$$\textit{Impact Excitation} : A^{q+} + e^{-} \rightarrow [A^{q+}]^{*} + e^{-} \rightarrow A^{q+} + \hbar\omega + e^{-} \quad (2.4)$$

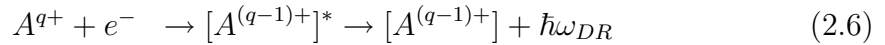
Stabilization via an Auger process refers to a doubly or multiply excited ion (two or more electrons in energy states above a vacant state) releasing an electron or *Auger* electron, which carries away the excess energy in a radiation-less process.

$$\textit{Auger de-excitation} : [A^{q+}]^{*} \rightarrow A^{(q+1)+} + e^{-} \quad (2.5)$$

This process is not possible for singly excited ions as an excited valence electron would not be able to transfer its energy to another atomic electron and ionize it. For neutral or only low multiply charged ions, Auger auto-ionization is the main de-excitation path. However, the Auger process depends only weakly on Z as it is an electron-electron interaction and as a consequence, highly charged ions tend to decay radiatively as the latter rates increase with large powers of Z (e.g.: for H-like ions, E1 and 2E1 electric dipole rates scale as Z^4 [12] and Z^6 [26] respectively, and magnetic dipole M1 transition rates increase as Z^{10} [26]). Therefore, highly charged ions are more likely to decay radiatively than via Auger auto-ionization. Processes including M1 transitions have been observed using HCI in EBITs, such as those presented in [58] and [32], both of which cite results that disagree with or are more precise than the compared theoretical models.

2.2.2 Dielectronic Recombination

In dielectronic recombination (DR), a free electron is captured into a vacant state of an ion A^{q+} with charge q . The energy difference between the free electron's kinetic energy and the bound energy level is transferred non-radiatively to a core electron in a state with energy E_1 . Due to this energy transfer, the core electron is simultaneously promoted to an excited atomic state with energy E_2 . This promotion forms an intermediate state in which the ion may be doubly or multiply excited.



$$\Delta E = E_2 - E_1 \approx E_e + I_p \quad (2.7)$$

The excited intermediate state then decays via an excited atomic electron falling into a lower vacant orbit, emitting a photon with energy equal to the energy difference between these two atomic states. As DR is a resonant process, this transition only occurs when the energy difference between the core electron state and the vacant state into which the free electron is captured is equal to the kinetic energy of the free electron E_e plus the ionization energy I_p required to free this electron from its newly recombined state (see Equation 2.7). This is a simplification as when the captured electron joins the ion, the electronic states change. As a result of this change, the energy difference between the states E_1 and E_2 does change, and hence, the energy of the emitted photon. This effect, however, can be ignored as the presented results do not have sufficient energy resolution to detect this.

As described above (Section 2.2.1), the excited state $[A^{(q-1)+}]^*$ in Equation 2.7 may also decay to the ground state by emitting an Auger electron, returning the ion's charge to its initial value via DR's time reversed process, namely, Auger auto-ionization.

For a sample DR process, consider what is called a KLL DR resonance for a He-like

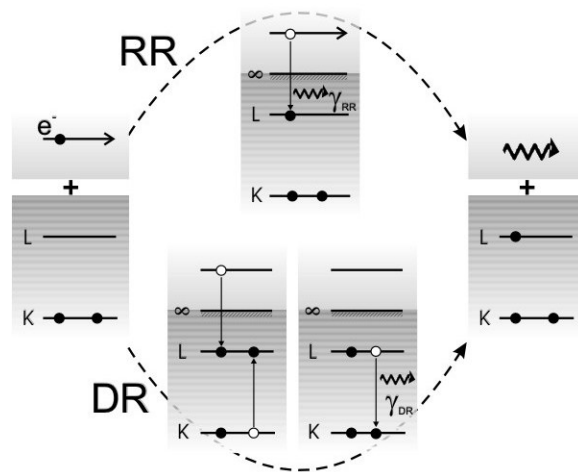
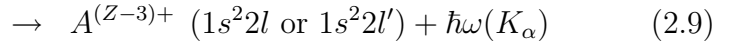
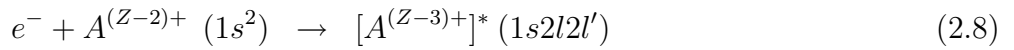


Figure 2.8: Schematic of RR and DR with an initial He-like state from [72] (used with permission). When an electron is captured into an atomic state, the energy difference between its initial continuum state and the captured state can be released in the form of a photon (RR). If this energy difference is equal to the energy difference between a core electron's state and an excited state, the energy can be transferred to a core electron, which can then de-excite by emitting a photon (DR). Note that the energy of the RR photon increases with electron beam energy, while DR only occurs at specific energies as it is a resonant process.

initial state as illustrated in Figure 2.8. A free electron is captured into the L-shell of an ion, while a bound electron can be promoted from the K-shell to the L-shell, thus forming an excited $1s2l2l'$ state. This intermediate excited state can then decay radiatively by emitting a K_α x-ray, resulting in a $1s^22l$ final state. Thus, the label KLL comes from DR's time-reversed process or Auger process as described above.



The cross sections to describe DR are highly dependent on the atomic structure of the species of interest. For this reason, they will not be theoretically described in this work (see [40] for further reading). It is important to note, however, that when the resonance conditions are met, the cross sections (and hence the rates) for the DR process can be many times higher than that of the competing RR process in an EBIT environment. The quantum interference of these two processes, namely DR and RR, has also been recently observed [71]. Extremely accurate measurements (± 14 eV) of 65 to 76 keV DR x-rays from highly charged mercury have recently allowed further testing of quantum electrodynamic (QED) effects and finite nuclear size contributions as discussed in [70]. Many EBIT experiments have been performed to measure DR resonance strengths, including [9] and [96], which can be compared to the absolute DR cross sections after adjustment for the assumed electron energy distribution in the beam.

2.2.3 Radiative Recombination

In addition to the above mentioned ion-electron collisions, non-resonant radiative recombination (RR) can also occur at any electron energy (see Figure 2.8). In this

process, an electron in the continuum, with an energy E_e , is captured into a vacant atomic electron state with an atomic binding energy E_B . To conserve energy, a photon is emitted with an energy equal to the sum of the electron's initial kinetic energy, plus the atomic binding energy of the previously vacant atomic state.



In this process, the photon energy is given by

$$\hbar\omega_{RR} = E_e + E_B. \quad (2.11)$$

These RR transitions follow the electron beam energy E_e in an EBIT, such that decreases or increases in the beam energy will be mirrored in the x-ray energy from an RR process (see Equation 2.11). Again, given that this process can occur at any electron energy, RR can also occur at the same energy as the competing DR process already mentioned.

One method of estimating the RR cross section is to use a simplified Kramers formula [55] (see Bethe and Salpeter [10]), for RR cross sections into hydrogenic states, which is in good agreement with experimental results for absorption into high- n states [2]:

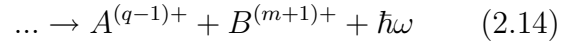
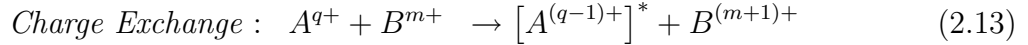
$$\sigma^{RR}[cm^2] = 2.10 \times 10^{-22} \frac{q^4 Ry^2}{nE_e(q^2 Ry + n^2 E_e)} \quad (2.12)$$

Here, E_e is the unbound electron's kinetic energy [eV], q is the charge of the bare ion, Ry is the Rydberg constant (13.6 eV), and n is the principal quantum number. Experimental absolute cross sections for RR and DR have been measured using storage rings like the Test Storage Ring (TSR) at the MPI-K in Heidelberg [76]. A merged-beam technique, in which the velocities of electron and ion beams were nearly

matched, produced low collision energies down to a few meV.

2.2.4 Charge Exchange

Charge exchange is of importance when considering interactions between highly charged ions. In this process, a bound electron from one atom or ion with charge m is transferred to another one via its capture into a vacant state. This vacant state may be an excited state or a ground state. In the former case, the ion can decay to the ground state via a single or successive photon emission as shown below in Equation 2.13. This process is particularly effective when highly charged ions with charge q are approached by slow neutral atoms or molecules, resulting in longer reaction times, thereby allowing multiple single electrons to be exchanged.



A formula often referenced for charge exchange cross section estimates, based on 268 measured values, was developed by Müller and Salzborn [77] for collision energies below 25 keV/amu:

$$\sigma^{chex}[cm^2] = 1.43 \times 10^{-12} q^{1.17} I_p^{-2.76}[eV] \quad (2.15)$$

This formula depends on the charge state of the ion q and the ionization potential I_p of the neutral particle. While similar formulae, providing the cross section for two to four electrons to transfer per collision were also given [77], these higher order processes can be neglected, as even the two electron transfer rates are only a few percent of

Table 2.2: Rate and cross-section estimates for charge changing reactions using Rb^{34+} with $E_e = 20$ keV.

Cross-section (cm^2)	Density (cm^{-3})	Velocity (cm/s)	Rate/ n_i
$\text{EII} = 8 \times 10^{-22}$	$n_e = 10^{13}$	$v_e = 10^{10}$	80
$\text{RR} = 2 \times 10^{-23}$	$n_e = 10^{13}$	$v_e = 10^{10}$	2
$\text{CX} = 5 \times 10^{-14}$	$n_o \leq 10^7$	$v_{\text{ion}} = 10^5$	0.05

the primary one electron transfer rates [82]. Note that this cross section considers neutral atoms as possible donors of electrons to HCI, rather than other less highly charged ions. It is assumed that the Coulomb repulsion between two HCI candidates would suppress the rate to a negligible level. Therefore, the differential equation (see Equation 2.1), only considers charge exchange between HCI and neutral background gas.

It is interesting to note that the cross-section for charge exchange is much larger than those for RR and EII if considering an example such as Rb^{34+} with an electron beam energy E_e of 20 keV. However, the large electron density inside the EBIT, coupled with the speed of the electrons, result in much larger *rates* for RR and EII than for CX. Rough estimates for these values are shown in Table 2.2. The end term would be the rate of the specified charge changing process if it is multiplied by the population of ions n_i with charge state i as outlined in Equation 2.1. These relative rates also illustrate the need for high vacuum to produce higher charge states when the relative rates of these processes become comparable.

Chapter 3

Experimental Setup

This chapter contains a general description and an in-depth characterization of the various components in the TITAN EBIT, a detailed treatment of the electron beam's characteristics, some assembly notes, as well as information on the diagnostic components used to collect the presented results and other diagnostic components installed for future use. The general operating principles of an EBIT can be found in the Introduction (see Section 1.3).

3.1 EBIT Components

The following section describes the main components of the TITAN EBIT. The characterization, further details, and other associated tests of these components can be found in Section 3.2.

3.1.1 Electron Gun

The 'heart' of any EBIT consists of its electron gun. This essential piece contains the cathode that produces electrons when it is heated to high temperatures. The cathode

is surrounded by electric field shaping electrodes to guide the electrons towards the trap. A typical cathode used in an EBIT consists of a tungsten heating filament coated with barium oxide. The surface emitting layer comprises of a mixed matrix of these elements, yielding a work function that is decreased from about $\Phi_W = 4$ eV to $\Phi_{W,Ba,O} = 2$ eV [75]. This low work function requires a lower operating temperature (≈ 1300 K) for electrons to be produced. A longer cathode life, therefore, is also expected as a lower temperature decreases the rate of cathode material evaporation and sputtering. This process is assumed to be greater at higher temperatures.

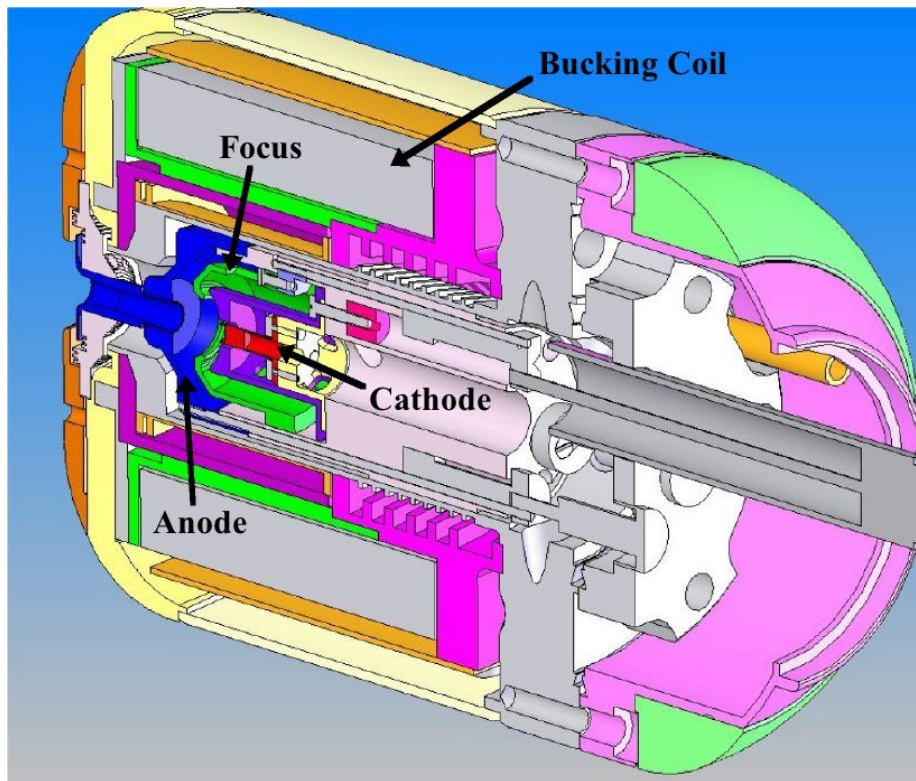


Figure 3.1: Cross-section view of the electron gun assembly (modified from [88]) with TITAN's smallest sized cathode installed. The cathode (coloured in red) emits the electrons, which are then pulled by the focus electrode (green) and accelerated towards the left through the anode (blue). The large piece (purple) surrounding the cathode is the holder, and the large grey areas surrounding the electron gun electrodes are the bucking coils.

3.1. EBIT Components

As shown in Figure 3.1, the cathode is enclosed by the focus electrode, which assists in the control of the emission current by pulling electrons away from the cathode surface. The focus electrode, the power supply of which is floated to the same potential as the cathode heater as shown in Figure 3.2 (typically around -2 kV), compensates for the edge effects of the cathode's field, assisting in guiding the electrons away from the electron gun. The focus and anode electrodes determine the electron beam current strength and affect the beam's tuning.

The anode electrode inherently provides the extraction field for the electrons as this electrode's power supply is not floated by the cathode power supply. This potential difference provides an acceleration of roughly 2 kV, at which point the electron beam is further accelerated towards the positively biased trap electrodes. The anode is particularly sensitive to beam tuning, therefore, minimizing the current striking this electrode is done routinely to optimize performance. It seems likely that some electrons are reflected from the collector, pass back through the trap, and strike the anode surface when the beam is not properly tuned.

The cathode and these shaping electrodes are enclosed by a soft iron shield and a large solenoidal coil, or so-called *bucking coil*, that produces a magnetic field to counter that of the residual superconducting field (see Figure 3.3). This is extremely important, as a residual magnetic field at the cathode surface will increase the electron beam radius in the trap due to less effective magnetic compression. As plotted in Figure 3.23, a residual field of around 10 Gauss can increase the beam radius by a factor of four, therefore, minimizing the residual field by adjusting the *bucking coil* is done to create optimal electron beam conditions. A large electron beam radius in the trap corresponds to a lower ionization rate, which is undesirable for charge breeding. A smaller coil, or *trim coil*, creates a magnetic field with the same polarity of the main field and provides fine tuning or additional focus control of the electron beam.

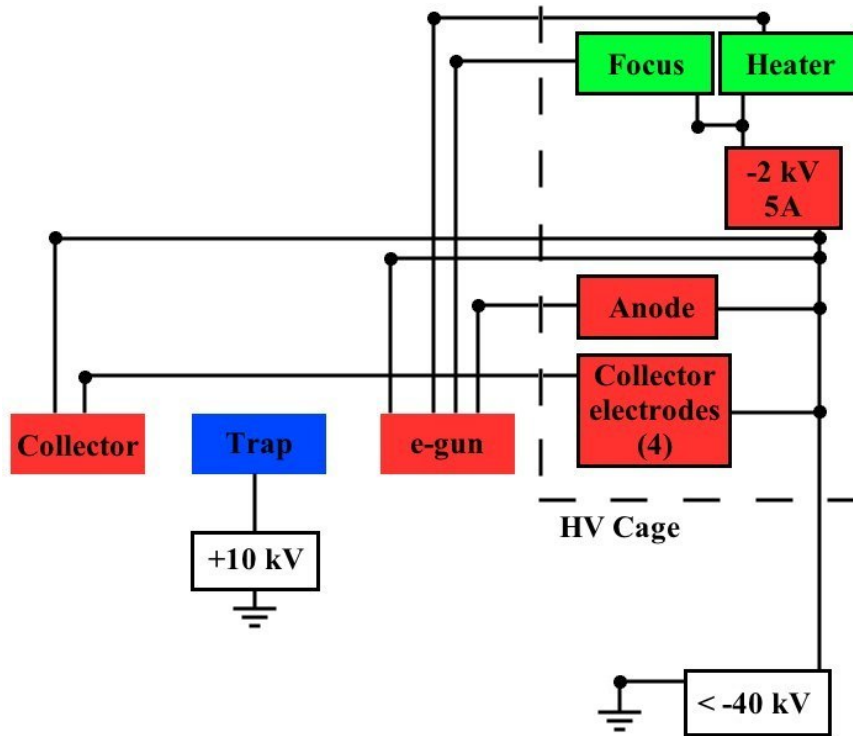


Figure 3.2: Schematic layout of the EBIT HV power supplies. Power supplies have a black border surrounding their respective boxes. By applying a negative potential of up to -40 kV to the platform inside the HV cage, all of the contained power supplies, the collector, and the electron gun are floated to this potential.

3.1.2 Ion Trap

The trapping of ions in an EBIT is done via the combination of radial trapping from the space charge of the electron beam and the superconducting magnet's field (see Figure 3.3), in addition to axial trapping from the electric field created by the trap electrodes inside the magnet bore. The TITAN trap electrodes, as shown in Figure 3.4, consist of sixteen electrodes, eight of which constitute the eight-fold radially segmented central trap. The remaining eight electrodes comprise of two groups of four cylindrical electrodes on either side of the central trap, called the collector and electron gun side electrodes respectively.

3.1. EBIT Components

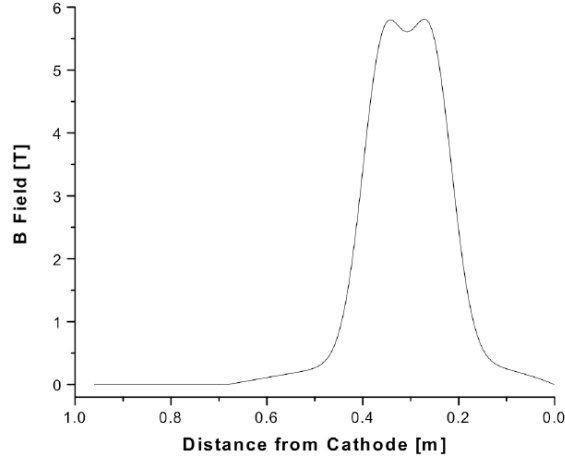


Figure 3.3: Simulated TITAN EBIT axial magnetic field strength (data from [80]). The B-field created by the superconducting coils is at a maximum in the trapping region and about zero at the cathode for optimal electron beam compression.

The eight-fold segmented trap electrodes are numbered from one to eight in a counter-clockwise direction with respect to the electron beam direction starting from the upper left following the nomenclature as shown in Figure 3.5. The sixteen trap electrodes can be biased independently, allowing for a wide variety of trap configurations. For example, the total trap length can be varied between 80 mm to 270 mm. The eight-fold segmented trap electrodes may allow various new techniques that have not yet been implemented in EBITs, such as the use of a high quality factor RLC-circuit for resistive cooling and electronic charge detection via the induced *image charges* on the trap electrodes. While radio frequency excitation was previously done in an EBIT at LLNL using electrodes inserted into the observation ports [87], the TITAN EBIT’s design allows a simpler approach to perform RF excitation, permits the use of quadrupole and octupole traps, in addition to not obscuring any observational ports (see [83, 94] for additional information on these methods). Additionally, it is conceivable that the radially segmented trap electrodes could be used to move the contained charged particles with an applied electrostatic field. Perhaps this could be used to move the

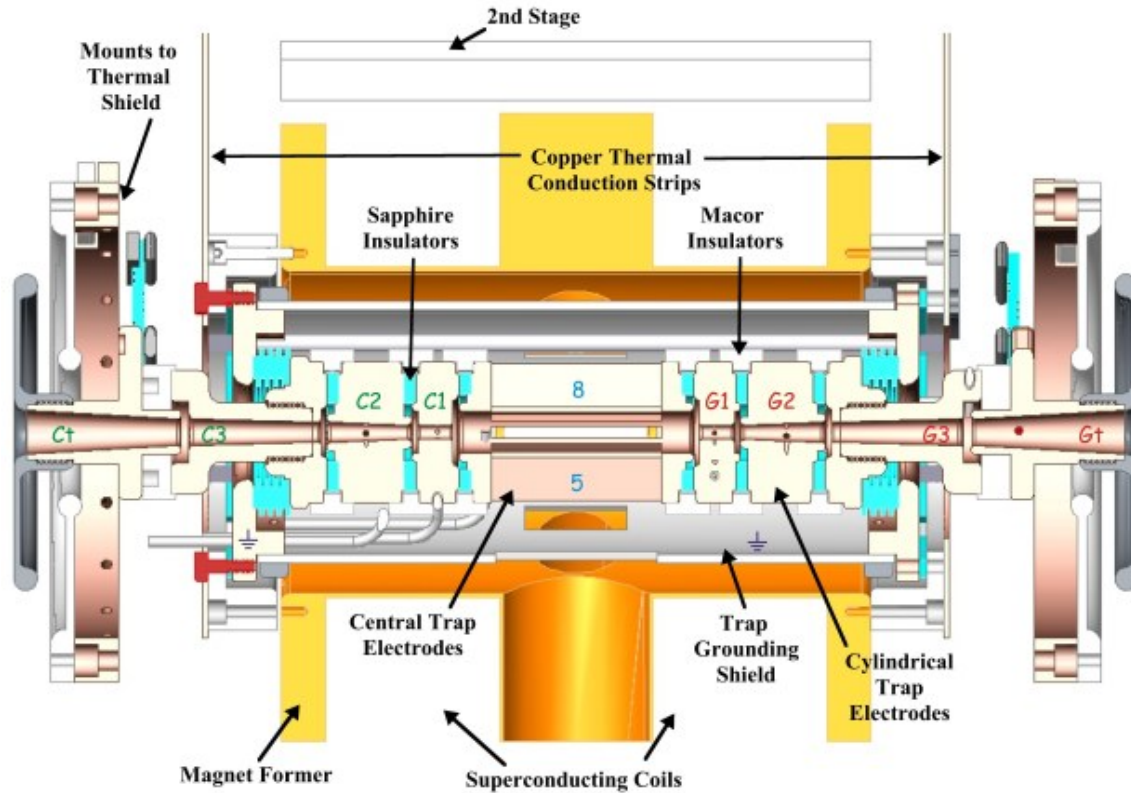


Figure 3.4: Cross-sectional overview of the TITAN EBIT trap electrodes. The radially segmented octupole trap electrodes labelled one through eight are located in the center, with the electron gun-side cylindrical electrodes on the right, and the collector-side cylindrical electrodes on the left. The pieces separating the electrodes (light blue) are the sapphire insulators, which provide good thermal conduction, with the larger spacers (white) being Macor-material insulators.

ion cloud with its undetermined distribution of charge states, with or without the electron beam on, and investigate what changes are observed. If higher charge states are typically found in larger orbits inside the trap and these orbits can be made to cross a more intense region of the electron beam, information about the distribution of ion charges and changes in charge breeding rates could be discovered.

From the seven magnet radial ports, the central trapping region can be accessed. The different regions in the magnet vacuum are separated by plates installed in the thermal shield and the magnet former. For each radial port used, two of these plates

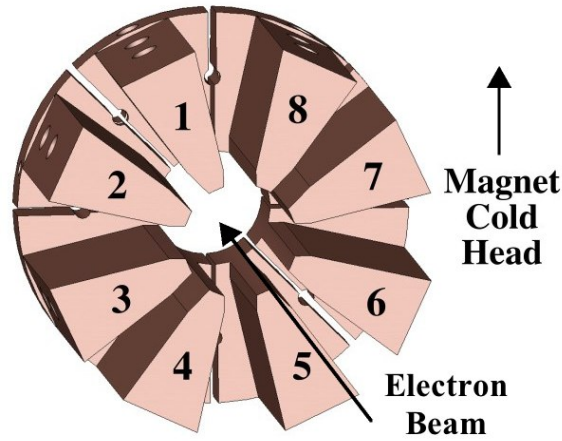


Figure 3.5: Central trap electrode labelling nomenclature, with respect to the electron beam direction.

must be removed, which would decrease the effectiveness of the cryogenic pumping in the trapping region. The use of thin beryllium foils and quartz windows, however, provide an adequate separation allowing the vacua to be maintained. Currently, three of the seven radial ports are in use. There is a beryllium window of $500\ \mu\text{m}$ thickness for x-ray spectroscopy installed in the magnet vacuum housing, in addition to a second beryllium window of $25\ \mu\text{m}$ thickness installed in the magnet former, to ensure a better vacuum pressure and a lower temperature inside the trap region. Given that the ion-emitted x-rays allow one to determine the charge states present in the trap, these x-ray transparent windows are essential for determining the ion populations and their charge states via spectroscopy. Similarly, quartz windows, which are transparent for lower energy photons in the visible range, allow spectroscopy at these energies as well.

A second port is used for pumping the magnet vacuum chamber. A vacuum pipe extension is used to decrease the effect of the magnetic field on the 300 L Varian turbo pump and an ion gauge to monitor the pressure. In order to limit thermal heat entering the trap region, metal discs with slits have been installed for the gas injection

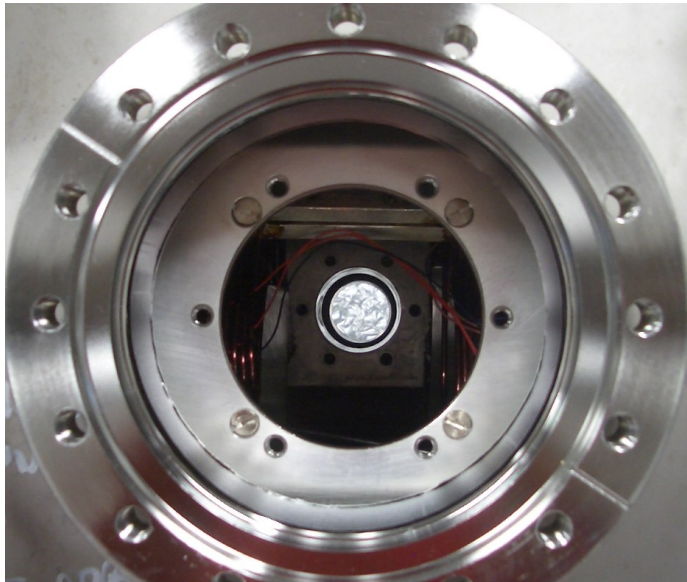


Figure 3.6: Photo looking inside a magnet vacuum chamber port with the magnet former and thermal shield windows removed. The gas injection system was later installed on the featured vacuum port. The turbo pump and larger slits were installed on the opposite side of the trap, which was not yet installed in this photo.

system in the thermal shield and magnet former. These slits also facilitate further collimation of the atomic gas beam instead of leaving the ‘window’ open entirely (see Figures 3.6 and 3.11).

Smaller versions of these slits are installed on a third port opposite the turbo pump for the gas injection system. A gate valve is attached to the magnet externally, allowing the gas injection system to be closed off from the main system. The injected gas, after passing through two differentially pumped regions, enters the magnet vacuum chamber and passes through a slit aperture installed in the thermal shield (see Figure 3.10), as well as a second slit installed in the magnet former (see Figure 3.7) before entering the trapping region.

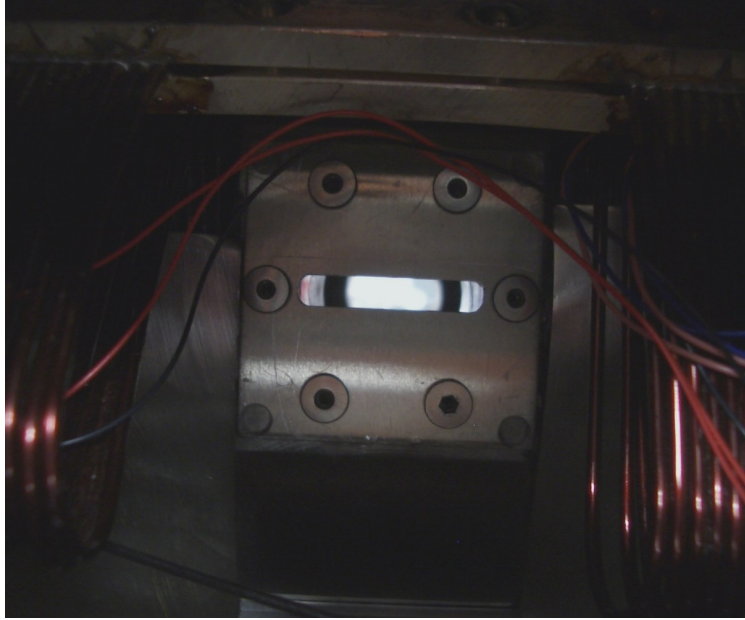


Figure 3.7: Photo of the gas injection slit installed on the magnet former. The superconducting magnet coils can be seen on both bottom edges in addition to some of the magnet internal wiring.

3.1.3 Collector

After the electrons pass through the trap region described above, they begin to decelerate as they pass through a steerer lens set at a potential between the collector and trap electrodes. The electron beam begins to expand as the strength of the superconducting magnetic field decreases and the space charge of the electrons repel each other. Before they reach the collector, the electrons have been decelerated to less than 1 keV. As they enter the collector (see Figure 3.8), the residual magnetic field is dissipated using a field generated by the collector coils, which surround the collector electrode, thus fully expanding the electron beam. The defocused electron beam is then deposited on the inner wall of the collector electrode, where the associated heat is transferred to cooling water via an extensive metal to water surface area.

During the electron beam dumping process, ions are sputtered off the collector electrode surface, and secondary electrons are created. The presence of two electrodes,

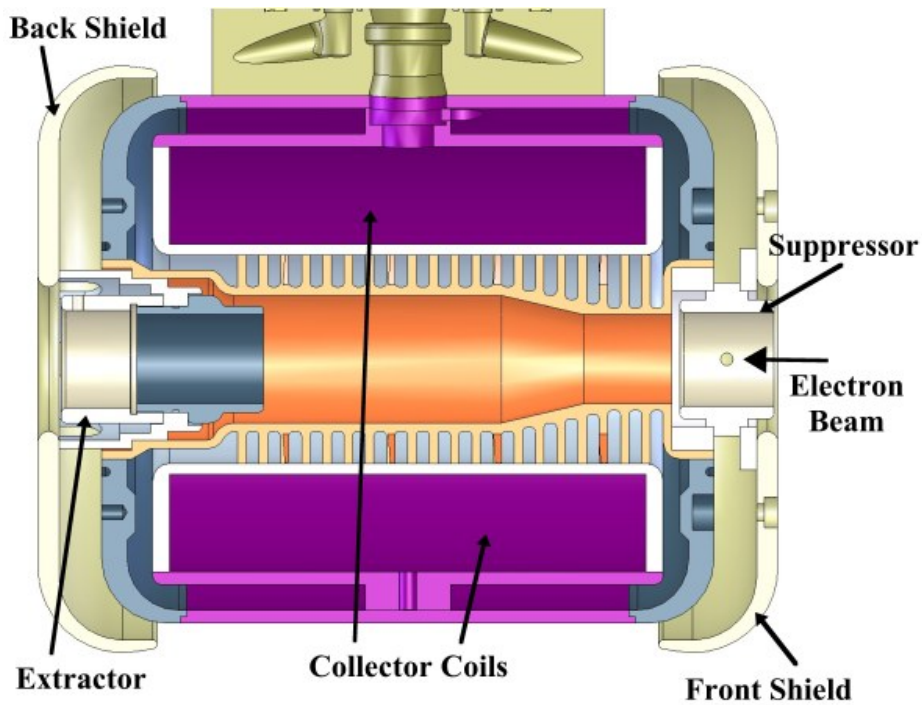


Figure 3.8: Cross-sectional view of the electron collector.

the *suppressor electrode* at the entrance of the collector and the *extractor electrode* at the exit of the collector, both with respect to the electron beam's direction, ensure that electrons do not escape the collector. The suppressor electrode is negatively biased with respect to the collector, to prevent secondary electrons produced in the walls from escaping. The extractor electrode on the other hand, is negatively biased with respect to the cathode (an additional -200 V or more), to ensure that electrons from the initial beam can not pass through the collector, in addition to blocking secondary electrons from escaping the collector. This electrode essentially separates the incoming ions from the electron beam, hence its name.

A thick copper cable is attached externally to the collector support structure, which is inherently attached to the collector itself, and carries the return current back to the high voltage (HV) rack. Given that this is the only connection bringing the return

3.1. EBIT Components

current back to the cathode power supply, it is read as the collector current, which should match the current being produced at the cathode for a properly tuned beam. In addition to watching this return current during beam tuning, the suppressor current is also regularly monitored.

3.1.4 Gas Injection System

One method of introducing a species into the EBIT is by injecting an electrically neutral, collimated atomic beam into the trap. This atomic beam crosses the electron beam, and with sufficient electron beam energy, results in the ionization of the injected gas. Once electrically charged, these species become trapped, and are further ionized by the electron beam to charge states given by the electron beam energy.

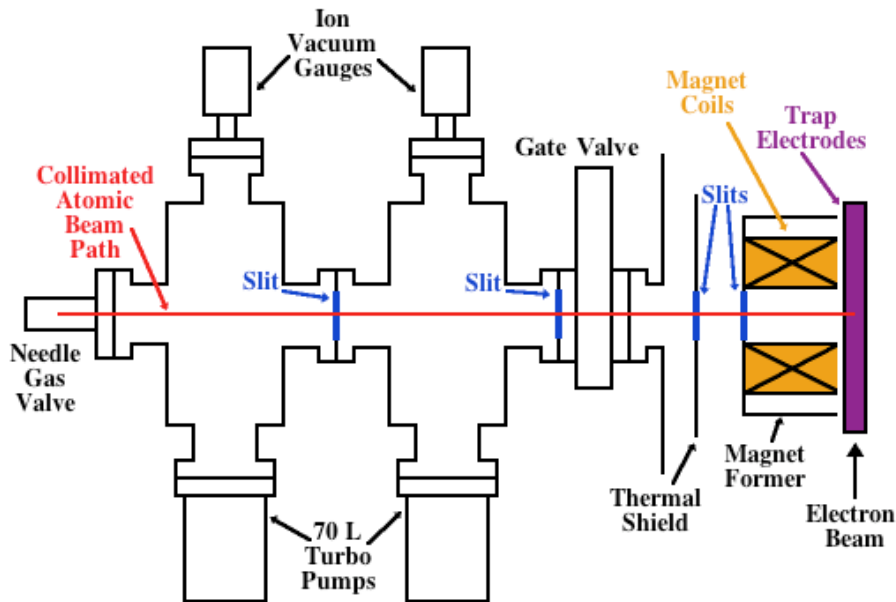


Figure 3.9: The two-stage differentially pumped gas injection system. This system can be used to inject a collimated atomic beam of neutral gas to the trapping region (located on the right in purple), which then becomes ionized and trapped.

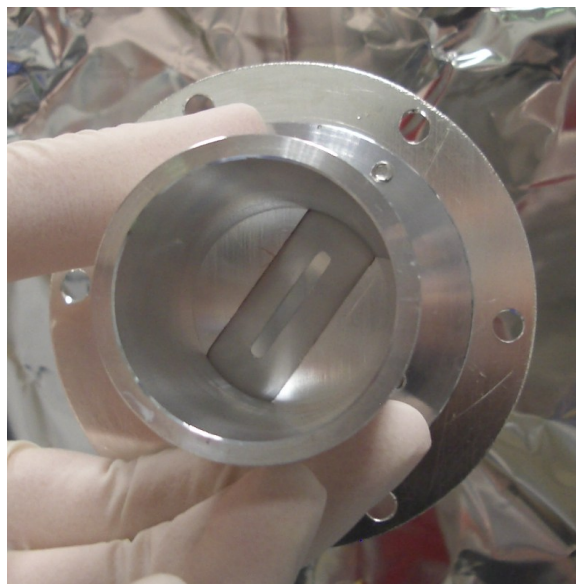


Figure 3.10: Photo of the gas injection shield slit assembly. A similar assembly with a larger slit was attached to the thermal shield exiting to the turbo pump.

The gas injection system uses a leak valve attached to a gas canister. The gas is allowed to leak into the first chamber called the gas_{valve} chamber. The gas must then pass through a slit to the next chamber, or gas_{trap} chamber, thus collimating the beam. It is further collimated using another slit between the gate valve and the gas_{trap} chamber in this series of multiple differentially pumped sections (see Figure 3.9). A slit-shaped atomic beam then enters the magnet vacuum chamber, passes through slits in the thermal shield (see Figures 3.10 and 3.11) and former, and then encounters the electron beam in the central trap region.

Thus far, the gas injection system has been successfully used to inject Kr (see Section 4.2 for results), and can be used in the future to inject other elements or molecules accessible via the gas phase, such as Ne, Ar, Kr, Xe, Cl_2 , UF_6 , Hg, and Bi.

During successful operation, the gas_{valve} chamber was operated around 10^{-5} to 10^{-6} mbar and the gas_{trap} chamber at approximately 10^{-8} mbar. The final density of the atomic beam in the ionization region is assumed to be reduced through collimation

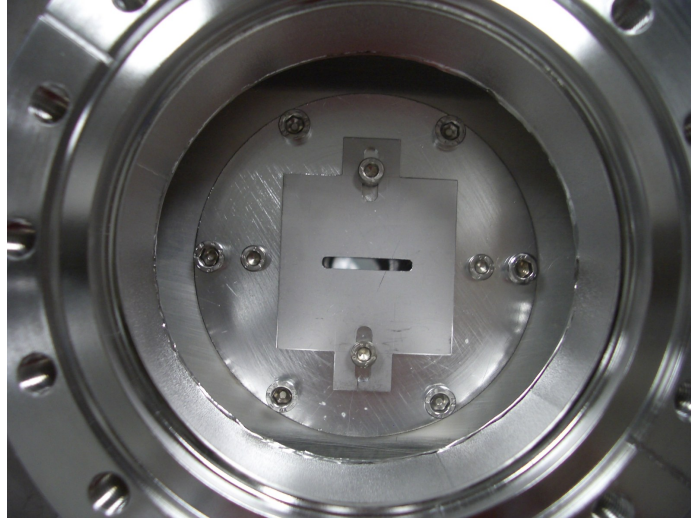


Figure 3.11: Photo of the installed gas injection shield slit assembly. See Figure 3.6 to see the same view without the slit assembly installed.

and cryogenic pumping (due to the shield and magnet former) by a few orders of magnitude. It is assumed that the density of neutral atoms injected is proportional to the pressure measured in the gas_{trap} chamber.

3.1.5 Ion Optics

To allow maximum flexibility, the TITAN EBIT was designed with two sets of beam optic electrodes or steerer lenses (see Figure 3.12). In basic configuration, the steerer lens consists of three hollow stainless steel cylindrical electrodes that can be individually set to the desired potentials and focus ions like a standard Einzel lens. Such a lens uses an electric field created by applying a potential to the central electrode and a different potential to the two side electrodes. The resulting field will alter the path of charged particles passing through the device, allowing the beam to be focused. What makes this particular set of ion optics unique, however, is the four-fold segmented central electrode [88]. Using a precise wire cutting method, the center electrode was divided

into four electrodes that allow for simultaneous steering in both the x and y directions. The steering and focusing properties, based on the superposition of the electric fields, were simulated using the ion optic program SimIon [48] and tested [24]. After the electrodes and frame were built, a control box (see Figure B.8) that determines the appropriate ratio of the four center potentials was built and tested [86]. Turning the two knobs on the box should allow the independent movement of the beam along the x or y axis.

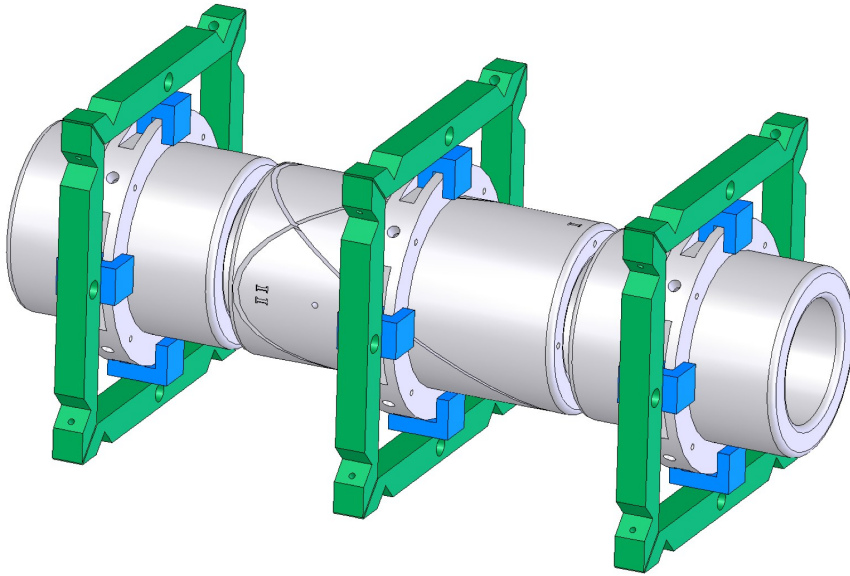


Figure 3.12: Steerer lens for ion beam steering and focusing. The central electrode in a standard Einzel lens (used for focusing ions) was cut into four segments, allowing this device to additionally steer the ions.

The steerer lens on the exit side of the collector should provide additional control of the injected ion beam for charge breeding and the ejected beam, after the desired charge state is reached. The electrode lengths for this set of ion optics are 70, 110, and 70 mm respectively, with electrode spacings of about 5 mm. The lens between the collector and trap allows one to set the potentials that the ions and electrons will experience,

3.1. *EBIT Components*

permitting increased control of their movements, acceleration, and deceleration. Due to space restrictions, the second unit's outer cylinders were shortened by 10 mm (5 mm on each side) in comparison to the other unit. Therefore, the electrode lengths for this shortened unit are 60, 110, and 60 mm respectively, with approximately 10 mm spacing between the electrodes. The electrode spacing between the four segmented center electrodes is about 1 mm for both units.

It should be noted that while both units have been successfully simulated and operated, thus demonstrating that the device can steer the beam, a test confirming that the beam can be moved independently along the x- or y-axis using the control box would be of interest. Given an opportunity and a position sensitive multi-channel plate (MCP) detector or any other similar way of detecting the beam position, this should be experimentally tested and confirmed.

3.1.6 **Support Devices**

Transformer

A 20 kVA transformer is used to power the electronics rack inside the high voltage cage. This transformer system is built to provide 220 V AC to the three power distribution bars in the rack and three phase 110V AC to the cathode power supply. The transformer, via interchanging a series of wires, can accept European standard 220 VAC or North American 110 VAC on its primary side, without any changes to the produced secondary voltages. The 'ground' of the secondary side circuit is set externally at the central copper grounding bar, located midway up the HV rack, as opposed to a wire connecting to the transformer internally (see Figure 3.13). This is in accordance with star-type grounding, where all units are connected to ground at the same place, to avoid ground loops (slight variations in ground potential) and achieve minimal electronic noise. For the same reason, the three common secondary sides of

the transformer are each set at the copper grounding bar, not to each other inside the transformer box with one cable connecting to the bar. For additional transformer information, refer to the transformer figures located in the Appendix B.2 and the company manuals.

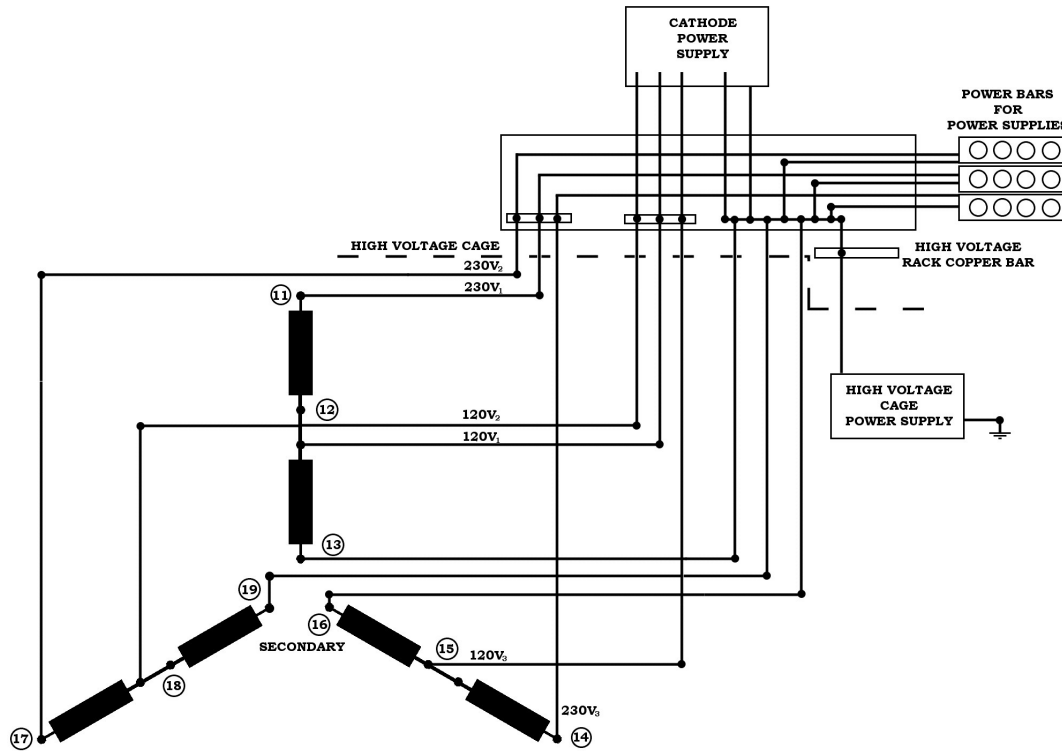


Figure 3.13: Schematic of the secondary side transformer electrical connections to the HV rack. Note that the common for the secondary side of the transformer is established on the copper bar located in the HV electronics rack. The required three phase power for the cathode power supply uses all three transformer segments and the 220 V for the power bars in the electronics rack are established individually, using the full length of each secondary segment. The power consumption from each power bar should be roughly equivalent for proper balance.

Cooling System

The collector and electron gun, which can be set at high voltages, are both cooled with water. To avoid electrical conduction problems using an open system with cooling

water at high voltages, an intermediate oil stage was employed. A closed water system cools the electron gun and collector. In the HV cage, a pump ensures that the primary water flows throughout the system and exchanges its heat with an oil-based closed system. The oil then exits the HV cage and passes through a cooler, where the heat is further transferred to the facility (MPI-K or TRIUMF) cooling water.

3.2 Assembly and Characterization of the TITAN EBIT

This section documents various characterization tests that have been completed with the TITAN EBIT, as well as some additional assembly notes at the end. These characterization tests include those with high voltage, additional detailed properties of the electron gun, trap, and collector, and calculations of the electron beam radius, current density, and space charge for the TITAN EBIT.

3.2.1 High Voltage Tests

A series of three high voltage tests were performed to characterize the TITAN EBIT. As the electron beam energy is roughly given by the potential difference between the cathode and the trap electrodes, it is important to ensure that high potentials can be applied to both components. The first test established a lower limit for the HV breakdown of the trap wires, the second attested the successful floating of the trap electrodes and their electrical feedthrough flanges. The third test documented the floating of the collector, electron gun, and the electronics rack in the high voltage cage.

The EBIT trap electrodes were electrically connected to the two vacuum feedthrough flanges using steel wires covered by a teflon tube for insulation (see Figure 3.14).

As these wires are used to apply high voltages to the electrodes, knowing their HV breakdown limit was important. A sample segment was sandwiched between two grounded metal plates, holding the steel wire and its outer teflon tube in place. The wire and tube extended beyond the two plates by about 6 cm. For accurate testing purposes, the tube was allowed to extend approximately 4 cm beyond the free end of the wire, to prevent sparking from the wire's end to the surrounding grounding plates. The wire was then connected to a 30 kV Heinzinger high voltage power supply, where the voltage was slowly increased as the wire was conditioned. The test continued until the power supply's maximum voltage at +30 kV was reached, setting a lower limit for the HV breakdown of the trap wires.

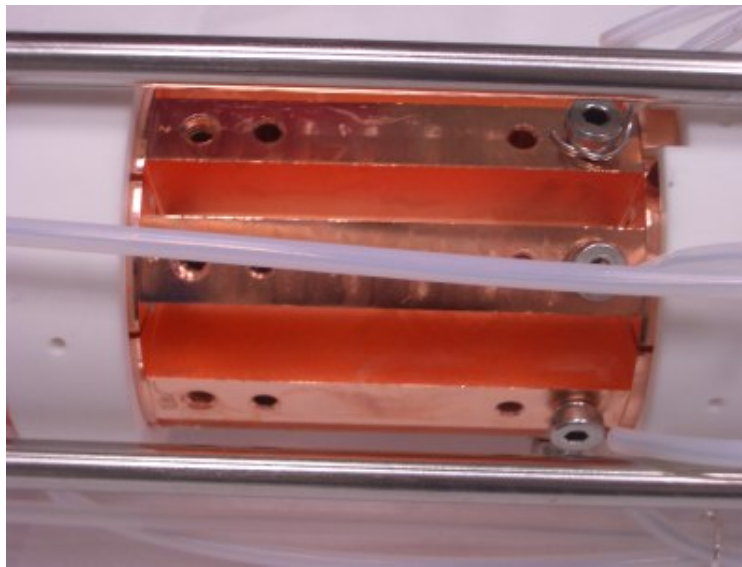


Figure 3.14: Photo of the central segmented trap electrodes with attached wires. The support steel rods as well as the Macor insulators on either side of the 8-fold radially segmented trap can be seen.

While it is necessary that potentials can be applied to the trap electrodes, it is also possible to float these electrodes and the electrical feedthroughs to which they are mounted. To test this, the sixteen trap electrodes were grounded to the feedthrough flanges. The *ground* electrode was connected to an external ground and a +10 kV

3.2. Assembly and Characterization of the TITAN EBIT

Heinzinger high voltage power supply was connected to both of the feedthrough flanges. It was ensured that sufficient safety precautions were taken and that the power supply was current limited to avoid significant sparking, which could possibly damage the trap. The voltage was then slowly increased, allowing the trap to become conditioned. The test concluded with the flanges being successfully floated to +10 kV. The limitation here, and its corresponding design flaw, is the connection of the *ground* electrode. While it is a prudent safety precaution to have this electrode, thus ensuring that any possible sparks are absorbed in a controlled fashion, away from the magnet components, it could have been attached to the magnet vacuum chamber. By having it connected to the 12-fold feedthrough flange, the maximum value to which the flange can be floated is constrained by the breakdown voltage of the SHV cables or the feedthroughs themselves, at approximately 10 kV. While floating the trap to higher potentials should not be necessary for this EBIT's charge breeding role, particularly given that the collector and cathode have already been successfully floated to -20 kV as described below and can reach an estimated limit of -40 kV, having the *ground* electrode attached to an electrical feedthrough is a loss of flexibility.

Demonstrating that the electron gun can be floated to high negative potentials is essential as the beam energy, or equivalently the potential difference between the central trap electrodes and the cathode (ignoring space charge), determines the charge states created. This test was done using a FUG HCN 14-20000 high voltage power supply (see Figure B.7). It was first ensured that the support structure for the EBIT, the FUG power supply that would float the HV platform, the rack housing the trap electrode power supplies, the superconducting magnet power supply, and the computer were all safely grounded. Proper cables used for HV purposes were used to connect the power supply to the HV rack grounding bar. This copper grounding bar is connected to all of the components in the HV rack, as well as to the *ground* or common of the secondary side of the transformer, which provides the power for the entire rack (see

Section 3.1.6 for more details). Previously, the HV rack had been grounded via a grounding cable connected to the rack's grounding bar. To float the rack, however, this connection was removed and instead the FUG HV power supply was attached to the copper bar, defining the common of the HV rack to be at the set negative potential. Floating of the electron gun and collector to -20 kV was successfully demonstrated (see Section 4.1), producing charge states up to He-like Ba⁵⁴⁺ with beam energies of around 27 keV.

3.2.2 Electron Gun Characterization

The electron gun's characteristics determine the maximum electron beam current and the corresponding maximum charge breeding rates. The TITAN EBIT's electron gun, therefore, will be discussed in more detail, including additional cathode information and upgrades, the characterization of the bucking and trim coils, the cathode's so-called 'perveance', and additional information on the power supplies used to power the unit. Tests describing the measured water flow used for cooling the electron gun and collector can be found with the collector characterization (see Section 3.2.4).

The TITAN EBIT was designed and built to use three different cathode sizes. These dispenser type cathodes, purchased from Heat Wave, all have an Os/Ru (so-called *M-type*) coating for emission enhancement and are described as being non-gassy. They operate between 950-1200 °C with operational lifetimes around 10,000 hours, have a Molybdenum base, a Mo/Re sleeve, and 3-5 A/cm² CW emission characteristics [56]. The three cathodes vary in emitting surface size (0.134, 0.250, and 0.500 inch diameters), and therefore, in maximum producible beam currents (0.5, 2.0, and 5.0 Amperes respectively). The TITAN EBIT has been operated thus far using the smallest cathode. All three cathode sizes have a Pierce-type geometry, namely, a spherical concave surface, with a radius of 10 mm, surrounded by an inactive curved

Table 3.1: Summarized power supply specifications for the electron gun.

Label	Voltage	Current
U_{bucking}	20 V	50 A
U_{cathode}	2 kV	5 A
U_{focus}	10 kV	5 mA
U_{heat}	15 V	10 A
U_{trim}	15 V	10 A
U_{anode}	10 kV	5 mA
$U_{\text{acceleration}}$	20-40 kV	0.5 mA

shaping electrode at the same potential (see Figure 3.15).

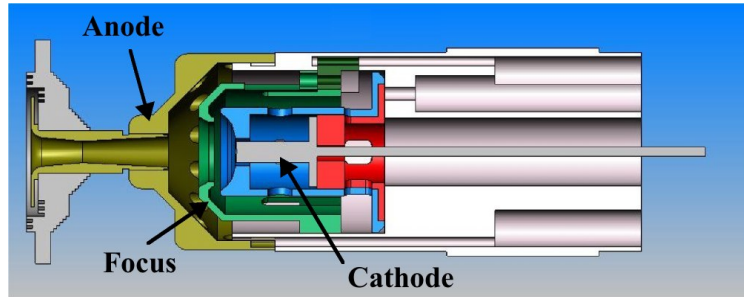


Figure 3.15: Cross-section view of the cathode assembly for the small 0.5 A cathode.

As mentioned previously, the electron gun consists of various electrodes that are set by their respective power supplies, as illustrated in Figure 3.16 and described in Table 3.1. The cathode power supply is used to float the isolated box in the HV rack that contains the cathode heater power supply and the focus electrode power supply, in addition to providing the current for the electron beam. This current is provided via a large copper wire connected to the body of the cathode. The heater supply is connected to the cathode filament using a special HV cable; it has no grounding shield for high voltage purposes. Similar cables are used to connect to the focus and anode electrodes. The power from the heating filament, by necessity, flows out to the main body of the electron gun.

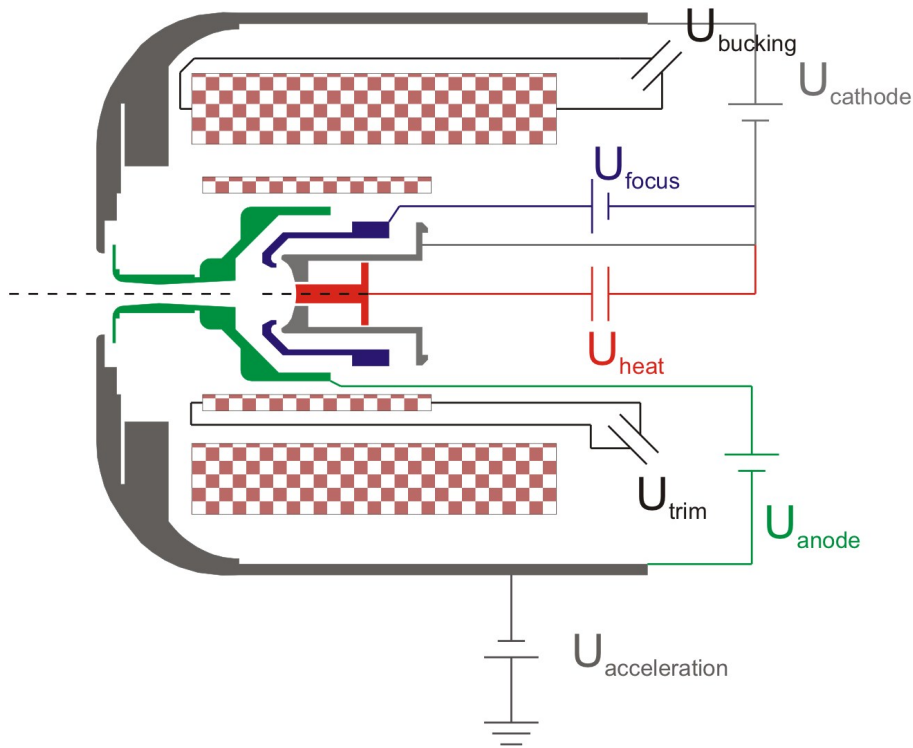


Figure 3.16: Electron gun components with schematic electrical circuits. The checkered areas indicate the position of the bucking and trim (smaller of the two) coils, which are used to tune the electron beam. The dashed line indicates the path of the electrons that are emitted from the cathode.

An additional way of describing or characterizing an electron gun is by its so-called ‘perveance’ P , which is given by: $P=I/\Delta U^{3/2}$, where I is the electron beam current and ΔU is the voltage applied between the cathode and anode. While there was no formal perveance design value, this property can be useful when examining and comparing electron guns. Using data from experiments after the final trap electrodes were installed, the perveance of the TITAN EBIT is calculated to be $0.60 \pm 0.04 \mu\text{A}/\text{V}^{3/2}$. For completeness, the perveance of the electron gun during the initial commissioning with a set of provisional trap electrodes was slightly less, at $\approx 0.2 \mu\text{A}/\text{V}^{3/2}$.

It should be noted that during the course of additional part installations, the electron

3.2. Assembly and Characterization of the TITAN EBIT

gun was inactive for about a month. When the cathode was again heated and electron beams were used to produce HCI with the provisional trap, the initial perveance values were less than $0.08 \mu\text{A}/\text{V}^{3/2}$ and as low as $0.001 \mu\text{A}/\text{V}^{3/2}$ before the cathode was once again conditioned to its regular values. This conditioning process involved using normal high operational temperatures, which produced larger electron beam currents. When the cathode temperature was then reduced, the observed electron current values, while decreasing, remained higher than the initial values. Repeating this process several times restored the cathode to its normal operational performance.

To characterize the electron gun, the properties of the magnetic field-producing coils used to shield the cathode and tune the electron beam were investigated. The length of the bucking coil wire was first estimated at 46 m by counting the number of layers (12) and the number of windings in each layer (16 to 17), for a total of 200 windings. Alternatively, the resistivity ρ of a metal is given by

$$\rho = \frac{RA}{l}, \quad (3.1)$$

where l is the length of the metal, R is the resistance in a given length, and A is the cross-sectional area of the wire or length of metal. This allowed the calculation of the bucking coil wire length, given the resistivity of copper [62] at room temperature and the coil's respective characteristics in Table 3.2. A value of 45 ± 1 m was determined, which agreed with the above estimation. The same calculation for the trim coil was also performed, resulting in a trim coil wire length of 20.3 ± 0.6 m. The effect of any additional residual resistivity [41], due to impurities and imperfections, was investigated but found to be negligible in these calculations.

Following a similar procedure as outlined in the collector coil tests, current was allowed to pass through the coils, and the temperature dependence of the resistivity was exploited. Therefore, the resistance as a function of current (and therefore temperature)

Table 3.2: Summarized recommended maximum values and characteristic values of the bucking and trim coils in the electron gun.

Value	Bucking coil	Trim coil
I_{\max}	34 A	6 A
U_{\max}	11 V	6 V
B_{\max}	≈ 120 mT	N/A
$R_{300\text{K}}$	217 m Ω	910 m Ω
Coil wire length	45 ± 1 m	20.3 ± 0.6 m
Wire cross-sectional area	0.0355 cm ²	0.385 mm ²

in addition to the magnetic field produced along the beam axis (approximately where the cathode would be) was measured. These test results were used to establish the maximum recommended values to ensure sustainable operating temperatures (below 400 K and 370 K respectively) for the bucking and trim coils as displayed in Table 3.2.

3.2.3 Trap Characterization

The charge breeding and all associated reactions take place in the EBIT's trapping region. It is, therefore, important to verify that the trap electrodes are connected properly to the electrical feedthroughs. Installation problems can be found by measuring the capacitance between the electrodes and by applying a radio frequency signal to one electrode and measuring the induced amplitude on neighbouring electrodes.

To ensure optimal performance at high voltage, both in terms of higher breakdown values and less potential variability due to electrode surface imperfections, the TITAN EBIT's sixteen trap electrodes were made of high purity, electro-polished copper. They are electrically separated by insulators made of Macor ceramic [23], in addition to sapphire rings for thermal conduction, which are also electrically insulating. The radially segmented central trap electrodes are separated from each other by short, small cylindrical aluminum-oxide insulators. When the electrodes and insulators were

3.2. Assembly and Characterization of the TITAN EBIT

assembled and placed inside their Macor insulator holders, the central electrodes only fit when they were exactly aligned. The entire assembly was then compressed with four steel rods for installation and alignment purposes. A grounding shield electrode surrounding the entire trap region, consisting of a two piece aluminum shell, protects the magnet coils and electronics from possible sparks from the trap electrodes. This cylindrical shell has eight rectangular holes that correspond to the superconducting magnet ports and their two respective sizes. This electrode was not designed to be floated, although it has been successfully floated to 1.5 kV and will start to discharge above 2 kV.

As described in more detail in Section 3.2.1, all sixteen trap electrodes have been floated simultaneously to 10 kV by grounding the electrode feedthroughs to the flange and floating both flanges. Higher potentials were not possible due to the limitations of the *trap ground* SHV feedthrough. Neighbouring trap electrodes have successfully operated with over 5 kV potential differences between them, excluding the central trap electrodes. Limits on the maximum potential differences between these segmented electrodes have not yet been established.

Moving the discussion beyond the trap, the properties of the magnet surrounding the trap were also examined. The main magnetic field is created by two superconducting coils in a Helmholtz configuration located in the magnet former, capable of producing a field of up to 6 T at a current of ≈ 120 A. The magnet former is directly attached to the coldest part of the magnet called the magnet cold head or 2^{nd} stage, which is cooled to about 3.4 K. Before installation of the trap electrodes and the four additional copper metal pieces for thermal cooling of the trap, the cold head temperature typically read around 3.4 K when cooled. By installing the trap, however, an additional heat load, namely the trap, was introduced. It should be noted that the initial magnet former temperature was about 3.9 to 4.0 K, and after this additional thermal contact between the magnet former and cold head was made, the magnet temperature appeared to

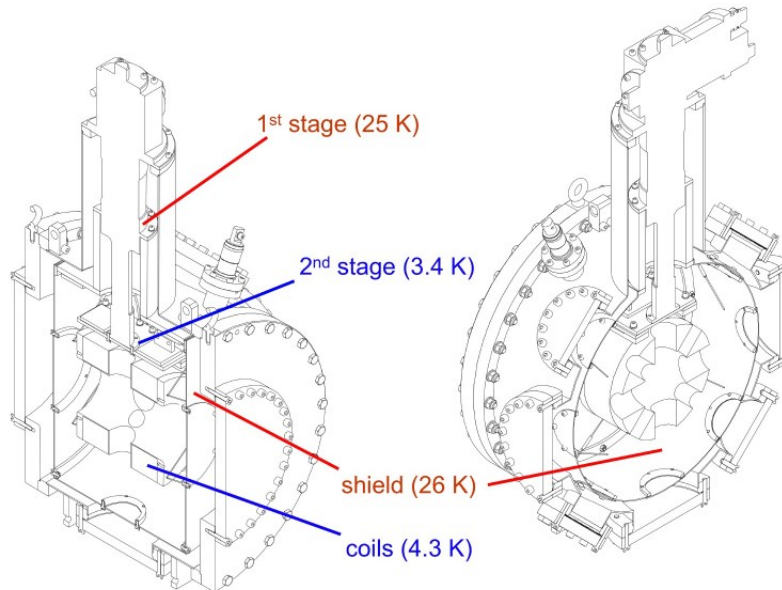


Figure 3.17: Initial superconducting 6 T magnet temperature regions. The temperatures changed slightly after installation of the EBIT trap electrodes, due to additional thermal conductivity between the second stage and the magnet former (see text).

decrease slightly to within a degree of the 2^{nd} stage now at 3.8 K. This is lower than the operating magnet temperature with the provisional trap first used to test the TITAN EBIT, as the final trap electrodes mount directly onto the magnet former for alignment purposes. As it is extremely beneficial for the trap to also be at cryogenic temperatures (for better vacuum pressure), the trap electrodes are thermally attached to both the magnet former and the magnet cold head. While no additional temperature sensors were installed to read the electrode temperatures, it is likely that the trap electrodes are also at about 4 K, producing an estimated pressure in the trapping region of 10^{-13} mbar [64]. This is reasonable to assume, as it is evident that the magnet coils are now more effectively cooled by the 2^{nd} stage, as displayed by the sensor's lower temperatures. This suggests that the additional thermal connections, namely the four copper pieces attaching the cold head to the magnet former and trap

3.2. Assembly and Characterization of the TITAN EBIT

holder, are successfully cooled. If these thermal connections cool the magnet more effectively, then their thermal connections to the trap electrodes should also result in the electrodes being at cryogenic temperatures.

Excluded from this temperature level are the two transition electrodes, C_{trans} and G_{trans} , which pass through the thermal shield and are the last trap electrodes on their respective sides. These two electrodes are thermally, but not electrically connected to the thermal shield via a thin copper strip and sapphire insulator, as shown in Figure 3.18. Sapphire was used here as it is electrically insulating but has a high thermal conductivity. It should be noted that the sapphire pieces in the trap region were coated with Apiezon vacuum grease, which is suitable for ultra high vacuum, to enhance thermal conductivity. The copper strip was used to give added flexibility, particularly since sapphire is brittle.

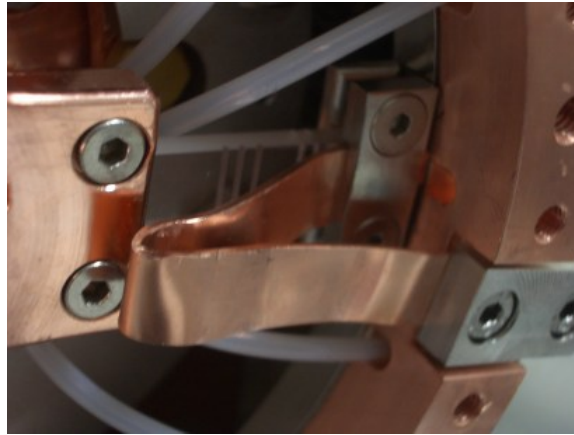


Figure 3.18: The thermal connection between the magnet’s thermal shield and the transition electrodes, C_{trans} and G_{trans} . The copper piece leftmost in the picture is the transition electrode, which is thermally connected to the sapphire piece. The sapphire is then compressed with the bent copper piece, providing the thermal connection to the magnet’s thermal shield. The ends of the sapphire electrical insulator / thermal conductor are coated with Apiezon vacuum grease for increased thermal conductivity.

The thermal shield, held at about 30 K, encloses the magnet former and the trap electrodes, providing a buffer between the magnet vacuum chamber at room temperature

and the magnet at 4 K. The magnet former is supported by a series of rods attached to the outer casing. These thin, but strong rods are thermally connected to the thermal shield to absorb the incoming heat from the room and are sufficiently cooled at the position where they are attached to the magnet former. The arrangement of these rods minimizes their number and, therefore, their heat intake, while at the same time allowing the alignment of the magnet.

The steel vacuum chamber, enclosing the thermal shield, has two horizontal ports through which the electron beam passes, in addition to seven radial ports. Copper rings are used for the vacuum seals throughout the EBIT, with the exception of the magnet horizontal axis flanges, which use indium. These horizontal ports on the magnet vacuum chamber also have ‘floating’ thermal shields installed. The two shields are essentially thin metal discs with a hole for access to the magnet bore and are affixed with thermally insulating plastic screws to the steel flanges. They are described as ‘floating’ as these shields do not have a good thermal (or electrical) connection with any other part of the apparatus.

Capacitance Between Trap Electrodes

Measuring the capacitance between trap electrodes through their electrical feedthroughs allows the investigation of any inconsistencies that could indicate a problem with the trap electrodes. Vastly different values could result from a loose wire or a broken electrical connection. The capacitance between neighbouring electrodes should be the largest, particularly between those sharing a large surface area and the opposite trend should be apparent for electrodes far from each other, with little shared surface area. Calculated estimates for the capacitance values were not performed as it was assumed that possible connection problems would result in large asymmetries or noticeable inconsistencies. Given the resulting asymmetries observed due to the proximity of neighbouring wires that connect to the same feedthrough flange, this assumption is

3.2. Assembly and Characterization of the TITAN EBIT

reasonable.

To measure the capacitance between the various trap electrodes, a Keithley 3322 LCZ meter using a signal test frequency of 100 kHz was used. This measurement is similar to that of using a Wheatstone bridge to measure resistances. Briefly, this meter has four BNC connectors which are divided into two sets. Each set is connected to one end, over which the capacitance is to be measured. To minimize noise and added capacitance, a box was fabricated to split each SHV signal to two BNC ports.



Figure 3.19: Photo of the folded electrode wires in the ceramic insulators. With the magnet and trap located to the left, half of the electrode wires can be seen before they were cut and attached to the electrical feedthrough flange.

The results of the test confirmed that neighbouring electrodes consistently registered the highest capacitance. As shown in Table 3.3, nearest neighbouring central trap electrodes (one through eight) had capacitance values of around 12 pF, whereas the capacitance between other central electrodes consistently dropped below 10 pF. Particularly high capacitance exists between C1 and C2, C2 and C3, C3 and *Trap Ground*, and the equivalent gun side electrodes on the opposite end of the trap with values around 30 pF. This is not unexpected, given that the comparative surface area

between the above mentioned pairs is larger and in close proximity, when compared to other possible pairs of trap electrodes. The trap ground electrode, as was expected, had large capacitances with respect to all trap electrodes, as this electrode basically consists of the entire support structure and surrounds the trap electrodes, thus offering a large surface area to create such a capacitance. For this reason, this electrode's effect on the others during the RF crosstalk test was also large. Noticeable features included the slightly higher capacitance values between the central segmented trap electrodes one through four and the collector side electrodes, as shown via their respective capacitance to electrodes C1 and C2. Larger than expected capacitance values were also measured between the other four segmented trap electrodes five through eight and the electron gun side electrodes such as G1 and G2. This apparent asymmetry results in a difference of approximately 4 pF from a capacitance of around 13 pF between C1 and trap electrodes one through four to a capacitance of around 9 pF between C1 and electrodes five through eight. The effect is reversed for electrode G1, as electrodes five through eight are preferred via an additional 4 pF capacitance as compared to electrodes one through four. By noting the nomenclature used to name the central segmented electrodes (see Figure 3.5), it is clear this effect is not due to improperly compressed electrodes, as this alignment problem would most likely manifest in a horizontal split (electrodes three to six being in one unit) due to a slight sagging of the trap electrodes. Based on the capacitance, it is also clear that this is not an effect of an additional capacitance from the electrode wires passing over the trap, as they all exit through the collector side (such an effect would only be present on the collector side electrodes). Examining the electrical feedthrough flanges, however, clarifies the situation. Electrodes one to four, C1, and C2 are all located on the same flange. As the wires had to be the same length for all electrodes to ensure a low thermal intake into the trap and an associated low thermal load on the magnet cold head, the wires were folded several times in the ceramic insulators to which the electrical feedthroughs

were attached (see Figure 3.19). Similarly, electrodes five to eight, G1, and G2 were also mounted to the same feedthrough, indicating that the additional capacitance is due to the proximity of wires attached to the same feedthrough flange. Note that this effect is also noticed in other combinations from the same electrical feedthrough flange. As the measured capacitance values appear consistent, and appropriately mirrored throughout all trap electrodes, all electrodes were believed to be functioning correctly after final installation, pumping, and cryogenic temperatures were established on January 23rd, 2006.

RF Crosstalk Between Electrodes

To further test that all electrodes were properly installed and functioning, a radio frequency (RF) crosstalk test was performed. This consisted of applying an RF signal to one electrode at a given amplitude and measuring the corresponding amplitude on other trap electrodes. By studying the amplitudes, one can determine if there are inconsistencies, indicating problems such as floating electrodes due to detached or loose wires.

The RF 5 V peak-to-peak (V_{pp}) sine wave at 400 kHz signal was produced by a Stanford Research Systems (Model DS345) 30 MHz Synthesized Function Generator. The frequency was chosen after scanning 100 kHz on either side of 400 kHz for any resonances that would have altered these measurements. Having found no obvious resonances, the values found in Table 3.4 were taken without the use of a 50 Ohm termination. This is mentioned as values taken with this termination would be half of the values quoted. The estimated relative error in the values is ± 10 mV. The amplitude was measured using a Tektronix TDS210 two channel digital real-time oscilloscope with the following settings and specifications: Input impedance was DC coupled, the function generator was used as the external trigger, and the specifications of the scope state that the signal was read in on a channel with $1.0 \text{ M}\Omega \pm 5\%$ in

Table 3.3: Measured capacitance between the TITAN EBIT trap electrodes. The values are in pF and were measured with a Keithley 3322 LCZ Meter at a frequency of 100 kHz. The error is ± 0.1 pF for all values.

Electrode	2	3	4	5	6	7	8	C1	C2	C3	C_{trans}	G1	G2	G3	G_{trans}	TrapGround
1	13.7	8.0	7.3	4.5	4.3	4.9	10.8	15.6	12.6	7.1	3.8	8.3	6.6	8.3	2.7	19.2
2		16.5	8.3	3.7	3.4	3.3	4.2	11.4	9.8	5.6	2.7	7.5	5.9	9.0	2.5	17.4
3			14.5	4.6	3.6	3.3	3.7	11.8	9.8	5.7	2.8	7.7	6.0	9.3	2.6	18.0
4				10.7	5.0	4.1	4.1	12.6	10.6	6.4	3.4	8.1	6.0	7.1	2.7	17.3
5					16.7	9.8	8.1	8.6	7.0	10.3	7.9	12.8	10.8	6.2	5.5	14.6
6						16.0	8.7	8.3	6.8	11.0	8.9	14.7	12.2	6.6	5.9	15.4
7							14.2	8.7	6.9	11.6	7.8	13.3	11.4	6.2	5.5	14.8
8								8.7	6.9	9.6	9.7	12.2	11.5	6.3	3.9	15.1
C1									36.4	14.4	5.4	8.5	7.8	9.5	3.6	25.8
C2										30.8	7.0	8.2	7.7	8.8	3.8	27.5
C3											16.7	12.5	12.0	8.2	6.2	29.3
C_{trans}												9.6	9.7	5.3	3.9	11.2
G1													34.2	14.1	8.9	24.3
G2														31.0	8.4	27.2
G3															13.3	36.4
G_{trans}																13.2

3.2. Assembly and Characterization of the TITAN EBIT

parallel with 20 ± 5 pF. To minimize noise due to the use of custom cables between SHV and BNC connections, an adapter box was fabricated. The remaining noise had a magnitude of 60 mV.

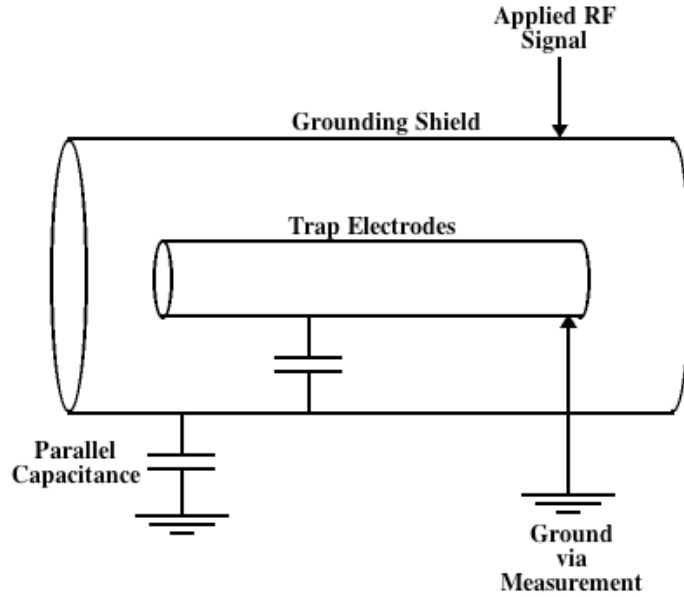


Figure 3.20: Schematic of the parallel capacitance during the RF crosstalk measurement.

The amplitudes measured appeared to be the same when the signal and monitored electrode were switched, so to avoid the process of switching cables on both sides of the EBIT between each measurement, some values were only measured once instead of twice, leading to a table that appears somewhat incomplete. By taking electrode five and six as an example, the measured amplitude on each using the other as the signal electrode yielded 350 mV both times. By scanning across the table, it is evident that the amplitudes are consistent (generally within 10 mV), indicating no unusual features. The amplitudes are also relatively on the same order, or correspond roughly to the distance between the electrodes being measured, also indicating consistency. The only observed asymmetry involved the use of the *Trap Ground* electrode as the

signal electrode. The amplitudes measured on all the other electrodes are offset by about 180 mV when compared to the reverse situation when the amplitude of the *Trap Ground* electrode was measured. This asymmetry comes from a parallel capacitance that only plays a significant role when the signal is applied to the *Trap Ground* electrode. Given that this electrode is essentially attached to the entire support structure of the trap, a capacitance exists between this electrode and laboratory ground via the magnet wires and structures (see Figure 3.20). Due to this added capacitance, the measured RF amplitudes are not symmetric. The end result is that the RF amplitude between the trap structure and laboratory ground has also been measured. This amplitude of 180 mV was fairly consistently measured, with the exception of those involving electrodes C_{trans} and G3, which could be due to a poor electrical connection during this specific measurement. All other measurements involving these two electrodes appear consistent with the remaining electrodes.

3.2.4 Collector Characterization

After the collector was completely assembled, but before mounting this unit in its respective vacuum chamber, various tests were performed to determine optimum operational conditions, the effect of water cooling, and determination of the magnetic field produced at a given current value.

During one of the tests, a Hall probe was placed in the center of the completely assembled electron collector to measure the magnetic field in the center of the device (see Figure 3.21) produced by the current flowing through the collector coil. The power supplies used in this test were connected in series to produce an adequate voltage range, coupled with the large current capacity of both supplies. As the range of the first six data points had been previously tested with a simpler setup, only two minutes was allotted before a measurement was made and equilibrium appeared to

Table 3.4: RF crosstalk amplitudes between all 17 trap region electrodes. A 5 Vpp, 400 kHz, sine wave test signal was used. Table values were taken without a 50 Ohm termination. The relative error is ± 10 mV.

Signal Electrode	Monitored Electrode																
	1	2	3	4	5	6	7	8	C1	C2	C3	C _{trans}	G1	G2	G3	G _{trans}	TrapG
1	295	175	185	175	115	115	125	240	310	260	155	100	180	145	175	80	220
2	290	350	190	105	95	95	115	230	210	130	80	165	135	190	75	190	
3	175	340	305	120	100	95	100	240	210	130	80	165	135	195	75	205	
4	170	190	310	240	125	110	110	255	220	140	90	175	135	155	80	195	
5					350	220	190			210	180	260	225	235	135	170	
6				350	220	335	200			225	195	290	250	250	140	175	
7				220	335	305				195	175	265	235	235	135	170	
8				190	200	305				245	210	245	235	235	105	170	
C1	325	250	260	275	200	190	190	200	650	650	285	130	180	165	195	100	285
C2	270	220	220	235	165	160	165	165	650	650	560	160	175	165	185	100	300
C3				230	240	255	215				340	250	245	245	150	315	
C _{trans}				185	200	180	220				330	200	200	200	105	140	
G1				280	315	290	270				250	210	620	620	200	260	
G2				240	270	250	250				240	210	620	620	190	290	
G3	185	200	210	85	150	160	150	95	185	175	175	125	280	570	280	390	
G _{trans}				140	145	140	110				140	105	190	170	155		
TrapGround	390	360	370	360	315	325	315	320	480	520	540	235	460	515	660	280	

Table 3.5: Summarized recommended maximum values and other characteristic values of the collector coil.

Value	Collector coil
I_{\max}	30 A
U_{\max}	19.5 V
B_{\max}	≈ 150 mT
$R_{300\text{K}}$	460 m Ω
Coil wire length	100 ± 3 m
Wire cross-sectional area	0.0375 cm ²

have been reached. A time interval of three minutes was used for the remainder of the test to ensure that thermal equilibrium (i.e., no further voltage increase indicating a resistance increase was observed) was reached at each current controlled data point (see Figure 3.22).

The test concluded at 48 A, 38.8 V, with a field of 253 mT. It should be noted that the voltage was still rising at this particular data point, even after having waited for three minutes. The solid copper leads of the collector, however, were already quite hot, so the test was stopped. A test performed later confirmed that the expected values had not changed, indicating that the coils had not been damaged by the high temperature levels. The maximum test settings correspond to a power of 1860 Watts and a calculated average temperature of 385 K, although during this measurement thermal equilibrium had not yet been reached. The cooling water flow (at 30°C) was quite high, but even at the highest power dissipation, a noticeable temperature difference through the water pipes between in-flowing and out-flowing water was not observed. These test results were used to establish the maximum recommended values, to ensure suitable operating temperatures (below 400 K) over the entire length of the coils (as opposed to the average) for the collector coil as displayed in Table 3.5.

Given the resistivity ρ , as defined in Equation 3.1, and the collector coil's resistance (460 m Ω at room temperature), it was determined that the wire length of the col-

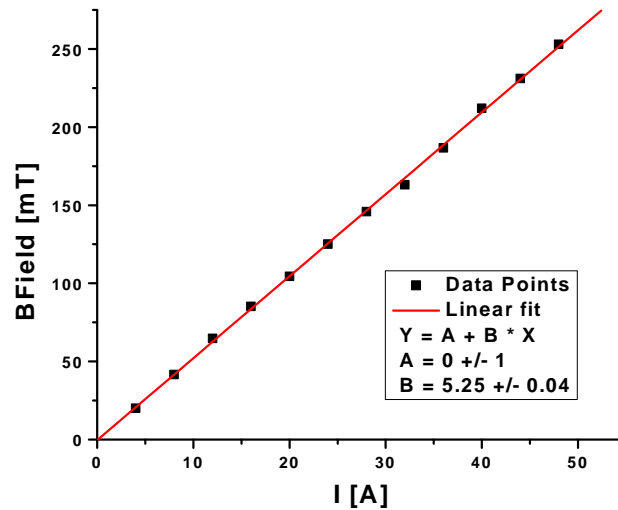


Figure 3.21: Collector coil tests plotting magnetic field vs current. As expected, the magnetic field in the center of the collector increased linearly with the current flowing through the coils.

lector coils was 100 ± 3 m. As mentioned previously during the electron gun coil characterization, the effect of any additional residual resistivity due to impurities and imperfections was found to be negligible [41].

After the EBIT system was fully assembled with an operational HV cage, additional testing was done to measure the flow of water through the collector and electron gun systems. With a pressure of 2.3 bar in the expansion vessel, the water pump in the high voltage cage was turned on to pump water through both the collector and electron gun systems which were hooked up in parallel. The total flow through the system was about 4.1 L/minute. The flow to the electron gun was then pinched off, producing a flow of 2.4 L/minute through just the collector branch. Reversing the roles, the flow through just the electron gun was measured to be 2.3 L/minute. Even these small flow rates have shown to be enough to effectively remove the heat generated by an electron beam with up to 400 mA. A stop in water flow results in a noticeable increase in resistance and hence voltage across the collector coils when the

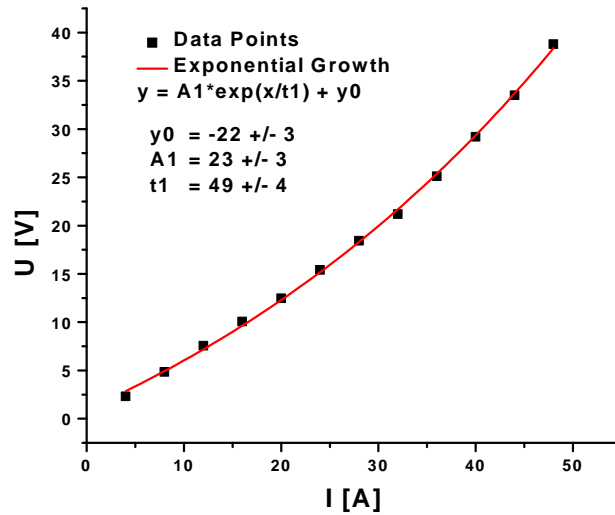


Figure 3.22: Collector coil tests plotting voltage vs current. The voltage increased exponentially as additional current passed through the coils. This trend is expected, due to the additional heat from the increased current and the resulting resistance increase.

beam is on.

Further careful testing of the heat dissipation via the collector cooling water is recommended, when the two larger cathodes for higher currents become available. While the collector electrode has been designed to transfer the expected heat to the water when using a 5 A electron beam, it must be ensured that sufficient water flow is maintained through the unit for proper operation.

3.2.5 Electron Beam Radius and Current Density

The determination of the electron beam radius allows the calculation of the electron beam's density, which is consequently used to estimate the rates of various charge changing reactions such as ionization. The Brillouin theorem [17] describes a uniformly distributed electron beam propagating under the presence of a uniform axial magnetic field B , which can be used to calculate the electron beam radius in the trapping

3.2. Assembly and Characterization of the TITAN EBIT

region. This theory assumes a laminar flow, such that electron trajectories do not cross, in addition to the assumption that the electrons are produced in a region with no magnetic field. It should also be noted that the initial electron thermal energy is neglected in Brillouin's theorem for the electron beam radius r_B , which is given by

$$r_B = \sqrt{\frac{2m_e I_e}{\pi \epsilon_0 v_e e B^2}}, \quad (3.2)$$

where I_e is the electron beam current, B is the axial magnetic field, v_e is the electron speed, m_e is the electron mass, e is the elementary charge, and ϵ_0 is the permittivity of vacuum. For ease of calculation, this equation can be reduced to the following form:

$$r_B [\mu m] = 829.91 \frac{\sqrt{I_e} [\text{A}]}{B [\text{T}] E_e^{1/4} [\text{eV}]}. \quad (3.3)$$

In the non-relativistic regime, the radius is calculated using $v_e = \sqrt{\frac{2eE_e}{m_e}}$ with E_e being the electron energy in eV. The non-relativistic version overestimates the velocity by 1% at electron energies of 10 keV and by almost 4% at 25 keV. For a more precise value, the relativistic form of the electron speed is given by

$$v_e = c \sqrt{1 - \left(\frac{E_e}{m_e c^2} + 1 \right)^{-2}}. \quad (3.4)$$

A more rigorous method for calculating the electron beam radius was given by Herrmann [46], who removed the assumption of laminar flow. This approach starts with a non-laminar electron beam (electron paths can cross) of cylindrical shape and takes into account the thermal motion of the electrons. This theory assumes that the axial velocity of the electrons is independent of their radial position, allowing the effective electron beam radius to be expressed in terms of the Brillouin radius r_B . The Herrmann radius also includes a multiplicative factor containing the contributions

from the magnetic field used for compression and a term derived from the properties of the cathode (radius r_c , magnetic field strength on its surface B_c , and temperature T_c). The Herrmann radius r_H , is then defined as containing 80% of the total electron beam current,

$$r_H = r_B \sqrt{\frac{1}{2} + \frac{1}{2} \sqrt{1 + 4 \left(\frac{8m_e k_B T_c r_c^2}{e^2 r_B^4 B^2} + \frac{B_c^2 r_c^4}{B^2 r_B^4} \right)}}, \quad (3.5)$$

where k_B is Boltzmann's constant. This formula has been shown to agree with experimental results from the TESLA EBIT, which is the sister EBIT of that used in TITAN. With the exception of the radial trap segmentation, the electrode structure, electrode radii, collector, and electron gun in both of these EBITs are currently identical. An upper limit of 50 μm for the electron beam radius was determined by measuring the spacial width of observed spectral lines [34]. The emission originated from extremely short-lived states in the trapping region of the EBIT. Assuming that the ion cloud overlaps the electron beam and that the ions would not have had time to move significantly before emitting a photon, this measurement is consistent with values predicted using Herrmann's formula.

Using the relativistic v_e (Equation 3.4) for r_B , the Herrmann radius equation is also valid in the relativistic regime. As shown in Figure 3.23 and in Equation 3.6, the electron beam radius is smallest when the residual magnetic field at the cathode's surface is close to zero. This is ideal, as the smaller the radius, the higher the electron current density and therefore the ionization rate is also higher (see Section 2.1.2 for more details). This term should be, and is typically minimized in experiments when tuning the beam. The dependence of the Herrmann radius on other experimental parameters is shown in Figure 3.24. Assuming that the second term is minimized

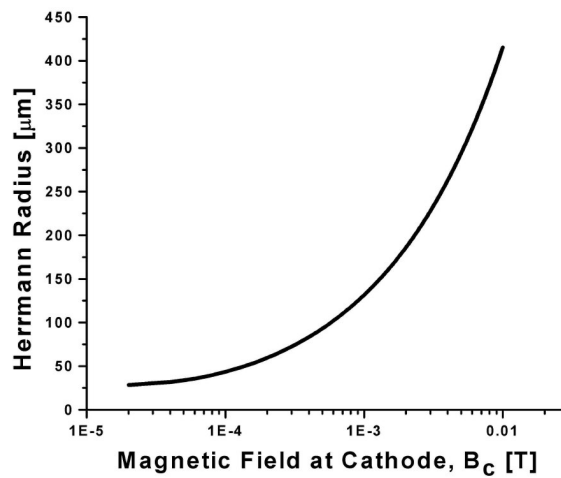


Figure 3.23: Calculated Herrmann radius plotted against the residual magnetic field B_c at the cathode. The following beam conditions were used for this calculation: $E_e = 9.24$ keV, $B = 5.8$ T, $T_c = 1470$ K, $I_e = 172$ mA. This graph demonstrates that optimum beam compression occurs when B_c is minimized.

during beam tuning, the Herrmann radius reduces to

$$r_H \approx r_B \sqrt{\frac{1}{2} + \frac{1}{2} \sqrt{1 + \frac{32m_e k_B T_c r_c^2}{e^2 r_B^4 B^2}}} \quad (3.6)$$

Given that the cathode currently in use has a radius of 1.70 ± 0.06 mm and using data from Feb. 23, 2006 with a beam current of 172.4 ± 0.1 mA, a field of 5.80 ± 0.01 T, and an electron beam energy of 9.24 ± 0.02 keV, the calculated Herrmann radius of the TITAN EBIT is 26.9 ± 0.5 μm . This calculation uses the error given by the company for the cathode concave spherical radius and assumes that the current flowing through the cathode filament (1.44 A) is more indicative of the operational temperature than the voltage (7.23 V), when compared to the bare cathode tests the company performed (see Table 3.6). The considerably longer wire length and electrical connections effectively increase the resistance and hence the voltage of the circuit. When the company operational temperatures (1170 - 1470 K) of the cathode were also taken into account, the cathode temperature T_c was estimated to be near its maximum recommended value at 1470 ± 90 K. As the field constant given by the company for TITAN's EBIT magnet is 515.61 Gauss/Amp and the operating current for a 6.0 Tesla field is 116.4 A, the error was estimated to be 0.01 T at a field of 5.80 T. This estimated error should account for the slight decrease in magnetic field in the center of the trap between the two coils, though is only valid at the center of the trap due to magnetic field variability. The errors were calculated and added in quadrature as outlined in [11]. The largest error contribution, by an order of magnitude, came from the error in the radius of the cathode.

To estimate the electron current densities that the TITAN EBIT is capable of reaching, the Herrmann radius was calculated for electron beam currents of up to 5 A. Recalling that the Herrmann radius by definition encloses 80% of the electron beam, leads to the following equation for the electron density in the trapping region:

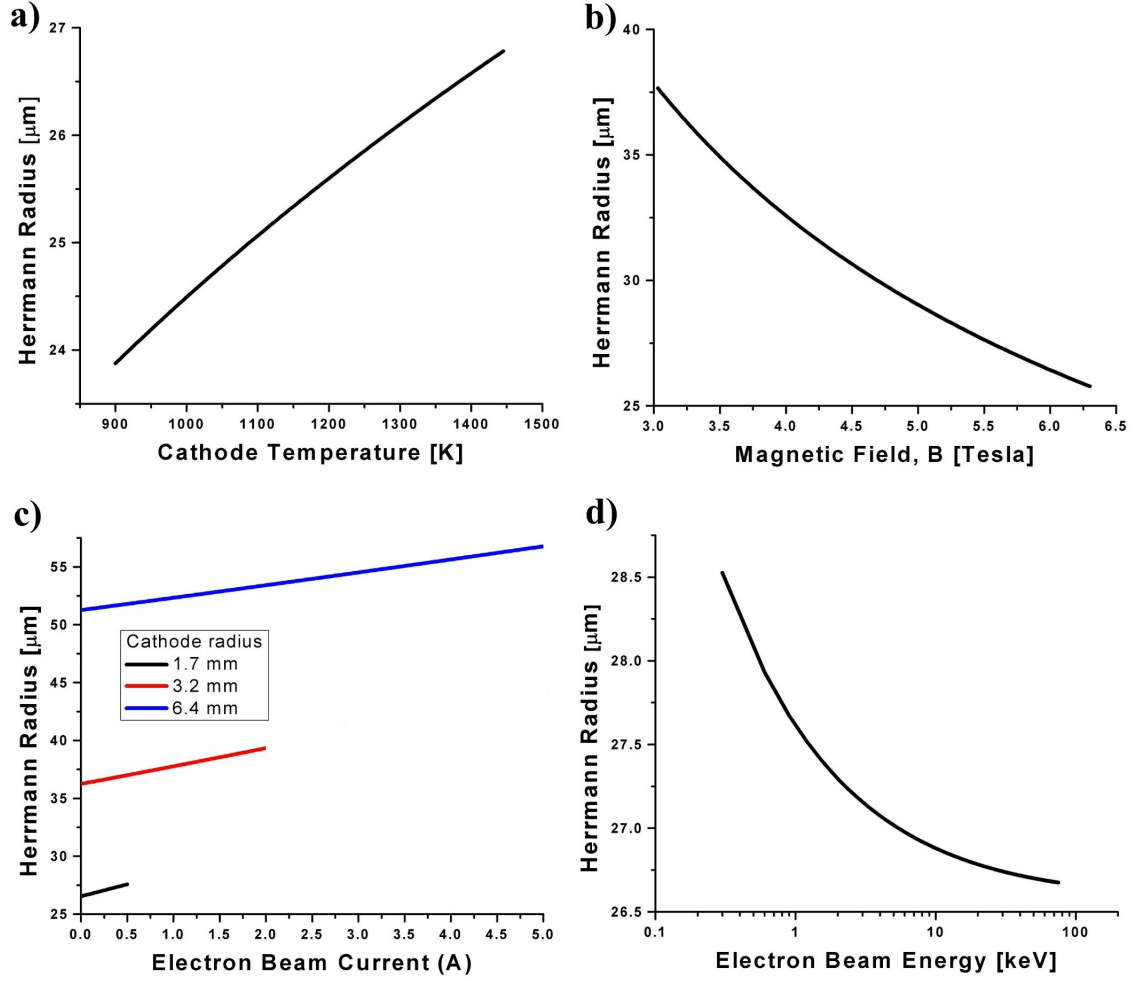


Figure 3.24: Calculated Herrmann radius as a function of cathode temperature T_c (a), magnet field B (b), electron beam current I_e (c), and electron beam energy E_e (d). Unless varied, the following electron beam conditions were used: $E_e = 9.24$ keV, $B = 5.8$ T, $T_c = 1470$ K, $I_e = 172$ mA, $r_c = 1.7$ mm, $B_c = 0$. (a) shows that electrons created with less thermal energy result in a more confined beam. (b) demonstrates the advantage of using larger magnetic fields for optimal beam compression. (c) illustrates that the Herrmann radius slightly increases with current, though note that the current density which determines the rate of ionization also increases with the current (see Figure 3.25). The slight decrease of the Herrmann radius associated with higher energy beams is shown in (d).

Table 3.6: Heat Wave dispenser cathode characteristic performance for part number 101100 [56]. Note that data was taken with a bare cathode at 1×10^{-6} Torr.

Temperature (K)	Voltage (V)	Current (A)	Power (W)
1170	2.90	0.90	2.60
1270	3.70	1.00	3.70
1370	4.70	1.10	5.20
1470	5.80	1.30	7.50

$$J_{\text{density}} = \frac{0.8I_e}{\pi r_H^2}. \quad (3.7)$$

Figure 3.25 clearly demonstrates that the TITAN EBIT, even using a modest beam energy of 15 keV with the largest planned cathode size, can reach current densities of about 40,000 A/cm². This is over six times higher than maximum values typically reported by other EBITs such as the HD EBIT with 6,000 A/cm² [64]. By comparison, the TITAN and TESLA EBITs have already demonstrated current densities of 15,000 A/cm² [64] at beam currents above 0.4 A. Note that the electron current density roughly increases linearly with the current, despite slight increases of the Herrmann radius with beam current. Increases in the electron beam energy, while slightly reducing the Herrmann radius and thus increasing the current density, are a small effect when compared to electron current increases.

3.2.6 Electron Density and Space Charge

For various spectroscopic experiments with an EBIT, it is necessary to precisely know the electron energy. Given the conditions created by such an intense electron beam, the radial space charge potential V_{SpC} generated by the negative charge density of the electrons in the beam has to be considered, as this affects the beam energy.

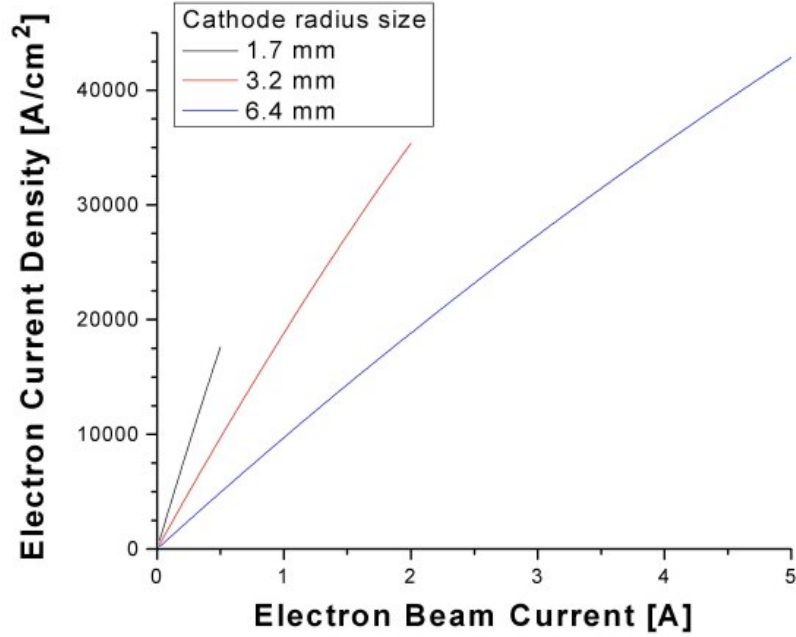


Figure 3.25: Electron current density plotted against beam current for the TITAN EBIT. The plot assumes the following values during the calculation of the Herrmann radius and the resulting current density (using Equation 3.7): $E_e = 15$ keV, $B = 6.0$ T, $T_c = 1470$ K, $B_c = 0$, and r_c varies for the three given radii. Only a modest beam energy of 15 keV was used, which can be achieved without floating the collector and cathode, as higher beam energies do not significantly alter the current densities. For comparison purposes, the HD EBIT has reported current densities of around $6,000$ A/cm² [64].

The space charge potential effectively reduces the interaction energy when compared to the applied acceleration potential between the cathode and trap electrodes. To quantitatively estimate this effect, one can consider an electron beam with a top-hat uniform profile distribution along the radial direction [37] and a constant Herrmann radius r_H (see Equation 3.6). This naturally assumes that there is a uniform magnetic field in the axial direction. The electron density ρ is then written in terms of the electron beam current I_e , the velocity of the electrons v_e , and the cross-section of the

beam A as

$$\rho = \frac{I_e}{v_e} \frac{1}{A} = \frac{I_e}{\pi r_H^2 v_e} . \quad (3.8)$$

To calculate the space charge potential, one must use Poisson's differential equation in cylindrical coordinates and solve for the potential and electric field with respect to the radius r . This assumes the beam is infinitely long, so there is only a radial component. Starting with

$$\nabla^2 = \frac{1}{r} \frac{\partial}{\partial r} r \frac{\partial}{\partial r} \quad \text{and} \quad \nabla^2 V_{\text{SpC}} = -\frac{\rho}{\epsilon_0} , \quad (3.9)$$

it is required that the derivative $\partial V_{\text{SpC}}/\partial r$ be continuous when $r = r_H$. This stipulation leads to the electric fields being given by

$$\begin{aligned} \vec{E} &= E_r(r) \hat{r} \\ E_{\text{SpC}}(r \leq r_H) &= -\frac{I_e}{2\pi\epsilon_0 v_e} \frac{r}{r_H^2} \\ E_{\text{SpC}}(r \geq r_H) &= -\frac{I_e}{2\pi\epsilon_0 v_e} \frac{1}{r} . \end{aligned} \quad (3.10)$$

Having solved for the electric fields above, the space charge potential can be calculated, using

$$-\frac{d}{dr} V_{\text{SpC}} = E_{\text{SpC}} . \quad (3.11)$$

For this calculation, two boundary conditions must be met: the potential must be zero at the electrode surface (radius = $r_{\text{trap}} = 7$ mm), and the potential must be continuous at r_H . This allows the space charge potential to be written in the following

two regions of space,

$$\begin{aligned}
 V_{\text{SpC}}(r \leq r_H) &= \frac{I_e}{4\pi\epsilon_0 v_e} \left[\left(\frac{r}{r_H} \right)^2 + 2 \ln \left(\frac{r_H}{r_{\text{trap}}} \right) - 1 \right] \\
 V_{\text{SpC}}(r \geq r_H) &= \frac{I_e}{2\pi\epsilon_0 v_e} \ln \left(\frac{r}{r_{\text{trap}}} \right).
 \end{aligned}
 \tag{3.12}$$

Figure 3.26 graphically shows the negative of the radial space charge potential, given

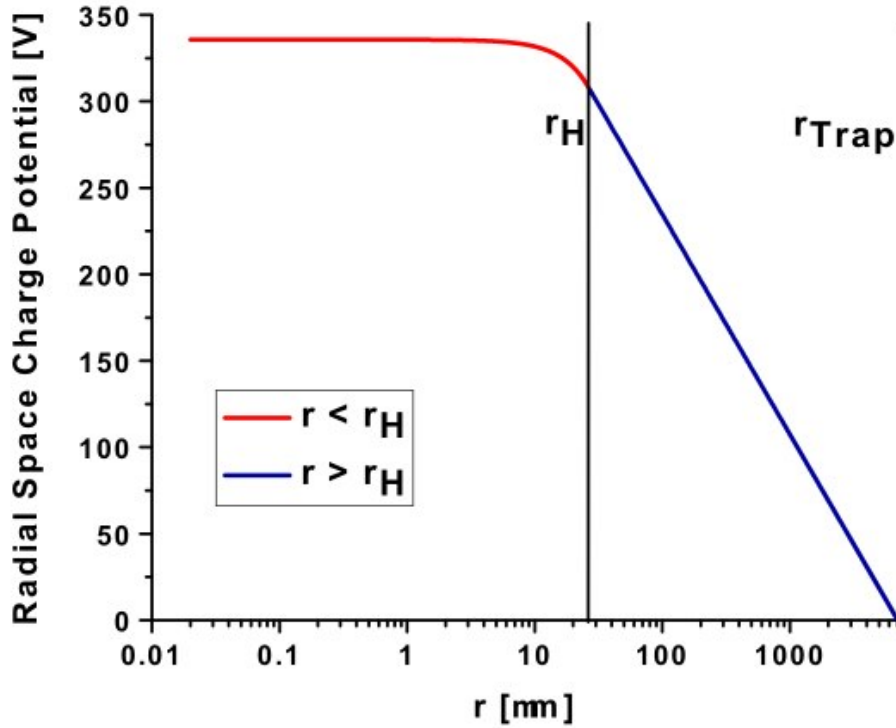


Figure 3.26: Sample plot of the negative of the radial space charge potential for an electron beam with the following characteristics: $r_H = 26.4 \mu\text{m}$, $E_e = 9.2 \text{ keV}$, $B = 5.8 \text{ T}$, $I_e = 172.4 \text{ mA}$, $T_c = 1370 \text{ K}$, $r_c = 1.7 \text{ mm}$. The radial space charge of the electron beam slightly decreases its effective energy.

by the two solutions in Equation 3.12, for the sample experimental conditions used above in the Herrmann radius calculations. By setting the radius to zero in the above equation and using the relativistic form of v_e , the space charge potential can be

simplified to

$$V_{\text{SpC}}(r=0)[V] \approx \frac{30I_e [\text{A}]}{\sqrt{1 - \left(\frac{E_e[\text{keV}]}{511} + 1\right)^{-2}}} \left(\ln \left(\frac{r_H}{r_{\text{trap}}} \right)^2 - 1 \right). \quad (3.13)$$

Using this equation, the radial space charge correction to the beam energy due to the electrons can be calculated, resulting in the total beam energy being given by

$$E_{\text{beam}} = (-V_{\text{cathode}} - V_{\text{HVCage}} + V_{\text{trap}} + V_{\text{SpC}}) \cdot q_e. \quad (3.14)$$

While more difficult to determine, the accumulation of positive ions in the trap also affects the radial space charge potential. A so-called compensation factor f can be defined as [93]

$$f = \frac{\sum_q n_q q}{n_e}, \quad (3.15)$$

where n_q is the total number of positive charge and n_e is the total negative electron charges. Quantifiable values for the number of ions and electrons vary greatly with the chosen operating parameters, including the element being trapped, gas injection pressure, trapping time, electron current and energy, and residual gas pressure. This effect, however, can be estimated by measuring the energy shift of dielectronic recombination resonances, and can be as large as 30 to 40% as reported by Martínez [72].

Axial Space Charge Potential

An additional trapping potential is created due to the difference in radii between the central region of the trap ($r_{\text{trap}} = 7$ mm) and the neighbouring electrodes C₁ and G₁ ($r_{\text{C}_1} = r_{\text{G}_1} = 2.5$ mm) due to the dependence of Equation 3.12 on the electrode radius r_{trap} . This radial difference creates an axial space charge potential, which is given

3.2. Assembly and Characterization of the TITAN EBIT

by the difference between the space charge potential calculated in the two different regions:

$$V_{\text{SpC}}^{\text{Ax}} = V_{\text{SpC}}^{\text{C}_1} - V_{\text{SpC}}^{\text{trap}}. \quad (3.16)$$

Therefore, the actual trapping potential is the summation of the trap depth set by

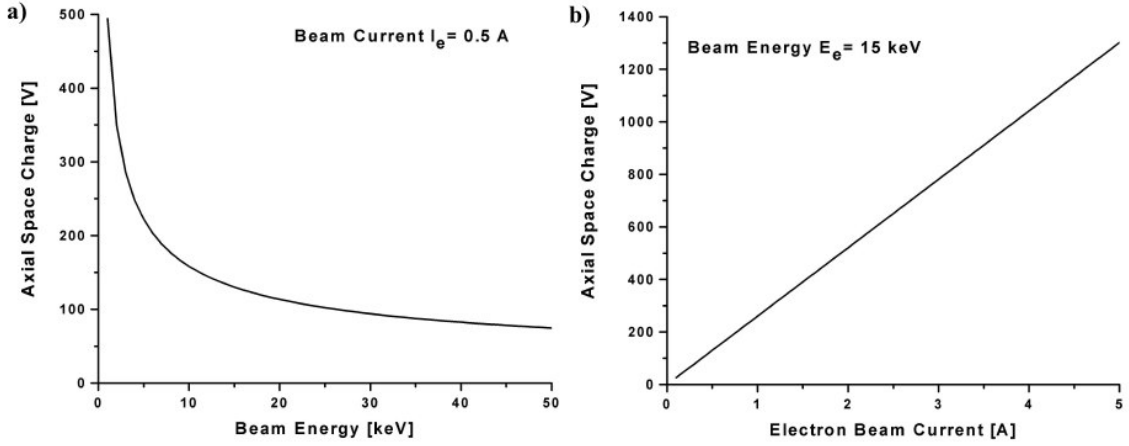


Figure 3.27: Calculated axial space charge potential due to trap geometry. This space charge potential effectively assists in the capture of ions and is plotted with respect to the electron beam energy E_e (a) and with respect to the electron current I_e (b).

the electrodes plus the axial space charge. For the geometry of the TITAN EBIT, the axial space charge can be written as

$$V_{\text{SpC}}^{\text{Ax}} \approx \frac{62 I_e [\text{A}]}{\sqrt{1 - \left(\frac{E_e [\text{keV}]}{511} + 1\right)^{-2}}}, \quad (3.17)$$

and is plotted with respect to the electron beam energy and current in Figure 3.27. It is assumed that the electron beam radius remains constant, yielding an axial space charge potential result that is independent of the radius, and instead dependent only on the geometry of the electrodes, the electron beam current, and the electron beam energy.

3.2.7 Assembly Notes

It became apparent during the EBIT construction that the magnet's thermal shield, as shown in Figure 3.28, was visibly misaligned. The displacement of about 5 mm between the trap axis and the thermal shield axis also corresponds to the 5 mm offset between the vacuum chamber wall and the thermal shield (see Figure 3.29).

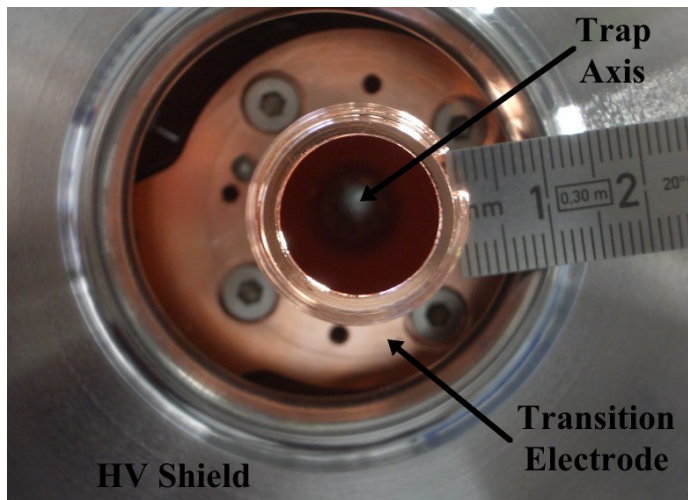


Figure 3.28: Photo of the misalignment of the magnet thermal shield. The transition electrode can be seen centered before its other half is attached. The steel disc obscuring the trap electrodes is attached to the thermal shield. The thermal shield axis would be centered with respect to the trap axis if they were both aligned.

While it is visibly clear that the thermal shield is misaligned, this does not affect the alignment of the trap. This shield is separately aligned and is there to provide a temperature buffer between the magnet former and the vacuum chamber. As stated earlier (see Section 3.2.3), the trap transition electrodes, C_{trans} and G_{trans} , are thermally attached to the thermal shield. Their alignment, however, is set by the magnet former, as is the rest of the trap structure. Therefore, the misalignment of the thermal shield, as no other important components depend on its alignment, is of no concern.

Given that the trap alignment is important and may play a role in future experiments

3.2. Assembly and Characterization of the TITAN EBIT

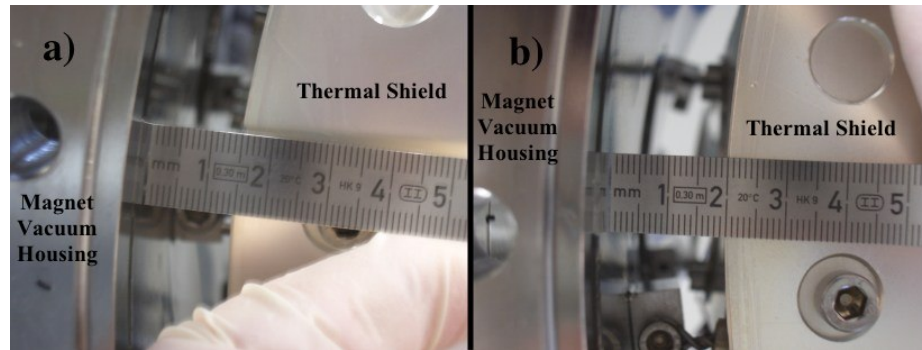


Figure 3.29: Photo showing the thermal shield misalignment. The distance between the thermal shield and the vacuum chamber is displayed as observed from the collector side along the beam axis. a) Left side spacing b) Right side spacing. In both pictures, the steel vacuum chamber is on the left and the thermal shield is on the right.

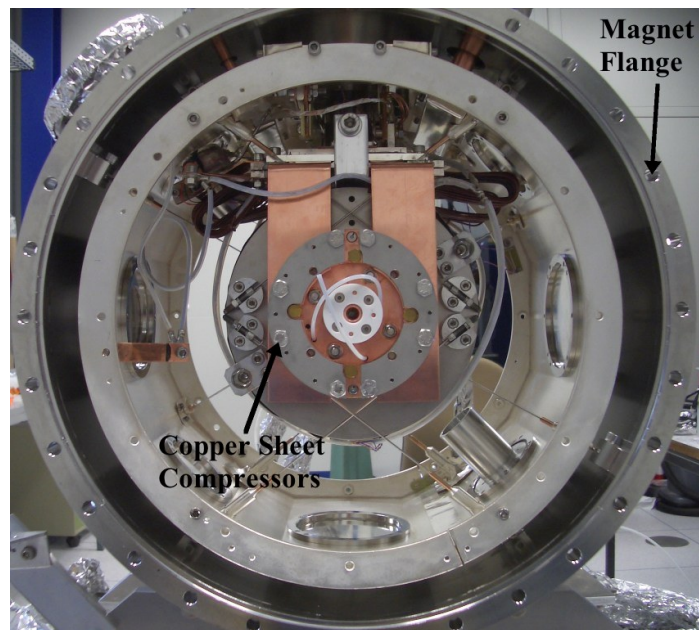


Figure 3.30: Photo of the points chosen for trap alignment. Looking with the electron beam, the thermal shield in light grey just inside the vacuum chamber is clearly shown. The aluminum pieces associated with the gas injection system can be seen protruding towards the magnet former. The copper pieces used to provide thermal conduction between the 2nd stage and the trap are also visible.

where the overlap of the electron beam and the ions is concerned, this will also be discussed here. The main trap electrodes (electrodes 1 to 8, $C_{1,2,3}$, and $G_{1,2,3}$) are

aligned together via their compression using four steel support rods. The transition electrodes, C_{trans} and G_{trans} , are then aligned by their physical attachment to C_3 and G_3 respectively, through the Macor [23] insulating (thermally and electrically) pieces separating them. To ensure that the trap was aligned, it was assumed that the magnet field was aligned with the axis of the magnet former containing the superconducting coils, which produce the field. The goal then was to ensure that the magnet former axis was aligned to that of the vacuum vessel and the rest of the EBIT.

As the trap mounts directly onto the magnet former, the alignment of the former and the trap was checked using a telescope approximately 3 m away. Steel wire, with a diameter of approximately 1 mm, was used to create four intersecting crosses along the beam axis. There were two crosses attached to the magnet main axis flanges, and two attached to the trap supporting structure or more specifically, the aluminum plates providing the copper sheet compression (see Figure 3.30). These sheets were compressed to ensure maximum surface area contact to the trap support structure, as these sheets provide the main thermal connection to the magnet second stage at about 4 K. The alignment was done prior to the final trap installation, which is in process in this figure. These points were chosen since two were connected to the magnet former and hence its respective alignment. The other two were part of the vacuum vessel and its respective alignment, which would later be aligned to the rest of the EBIT. The various EBIT components are assumed to be aligned via the attachment of their vacuum housing chambers.

Assuming that the field axis was the same as the former axis, careful adjustment led to a slight alignment improvement. The maximum displacement of one side of the former with respect to the other was estimated at 0.5 mm, which corresponds to a maximum misalignment between the trap axis and the magnet vacuum vessel/EBIT axis of 0.08° . As the crosses from the magnet former and the magnet flange were aligned on one side, a length of 34.7 cm was used for this calculation, as this is the

3.3. TITAN EBIT Diagnostic Components

Table 3.7: Some calibration sources and their respective dominant emission lines [35].

Source	Dominant Emitted X-ray Energies [keV]				
⁵⁵ Fe	5.888	5.899			
²⁴¹ Am	13.946	17.751	26.3448	59.5412	
¹⁰⁹ Cd	88.04	21.990	22.163	24.912	24.943

distance between the cross from one side of the magnet former to the magnet flange on the opposite side.

3.3 TITAN EBIT Diagnostic Components

Various devices are currently installed for TITAN EBIT diagnostic purposes. A germanium x-ray detector, located on one of the magnet’s radial ports, is used to identify the ion species and charge states present in the trapping region. Between the magnet and electron gun, a channeltron is installed for future ion injection efficiency tests, in addition to a prism which allows for visual viewing and the possible temperature measurement of the cathode.

3.3.1 X-ray Spectroscopy Setup

As the TITAN EBIT was built at the MPI-K where an EBIT was already operational, various detectors were available to observe the emitted x-rays. Given that good energy resolution for x-rays can be provided by detectors with germanium or silicon crystals, an Ortec high-purity germanium detector (see Table 3.8 for specifications) was chosen. These semiconductor detectors essentially act as solid state ionization chambers, where an impinging x-ray’s energy is absorbed by an electron, which produces many secondary electron-hole pairs. An electric field applied to the crystal results in the collection of the electrons, and hence a signal. The integrated charge of this signal

corresponds to the number of electrons collected, and therefore, to the energy of the x-ray deposited. This charge is then converted into a voltage by a preamplifier, before being shaped and amplified by a spectroscopic amplifier.

In this experimental setup, the amplified detector pulse was then sent to a standard PC with a multi channel analysing card, which in combination with Ortec's accompanying computer software, Maestro, displayed in a histogram according to pulse height (x-ray energy deposition). The pulse height spectra were then calibrated with known sources (see Table 3.7) to translate the axis to energy units. Gaussian fits were performed on the lines from the calibration sources, allowing one to match a channel number with a specific x-ray energy. For calibration, at least two x-ray peaks were required, with preference for the calibration points to be close in energy to the range of interest. The known peak energies and their corresponding channel numbers were then plotted, and a linear fit was performed yielding the energy axis transformation. The produced spectra were then compared with those of the ion species known or believed to be present in the trap, and matched with their respective distinct x-ray emission lines, signifying such processes as direct excitation, radiative recombination, and dielectronic recombination. Background ions such as Ba and W are also found in the EBIT trap, as these species evaporate off the cathode and become ionized, thereby providing dependable distinctive emission lines at charge states governed by the electron beam energy, covering a wide range of energies.

For the presented results, the tube protruding from the detector containing the germanium crystal was placed level to the beryllium window port on the superconducting magnet housing. The detector position was varied depending on the source strength, such that the distance between the end of the detector and the beryllium surface was anywhere from 2 cm to 30 cm. A negative HV power supply biased the detector to around -1400 V for sufficient gain of the pulses sent to the multi channel analysing card.

3.3. TITAN EBIT Diagnostic Components

Table 3.8: Properties of the solid-state, planar, high purity germanium detector (GLP-36360/13P) used during the first tests of the TITAN EBIT.

Energy range	3 to ≈ 300 keV
Area	1000 mm ²
Crystal thickness	≈ 13 mm
Crystal active diameter	36 mm
Be window thickness	0.254 mm
Maximum negative bias	-2500 V
Resolution at 5.9 keV	≈ 360 eV
Resolution at 122 keV	≈ 560 eV
Distance to the trap center	245 - 273 mm
Solid angle	1.4 to $1.7 \cdot 10^{-2}$ sr

3.3.2 Installed Prism and Channeltron

A linear feedthrough is attached to the top port of the vacuum chamber between the electron gun housing and the magnet vacuum vessel. This feedthrough allows the insertion of a glass prism and a channeltron (see Figure B.5) to the beam axis, when the electron gun head is not extended and operational.

The prism is aligned so that it reflects the emitted light from the heated, glowing cathode out through a vacuum side port for observation. This simple setup allows an easy and quick visual confirmation that the cathode is indeed heated. Additionally, the light can be analysed using an optical pyrometer, to measure the cathode temperature via its black body spectrum. Such measurements have already been done in testing other cathode materials for EBIS/T devices [84]. Using Heat Wave Lab's (Model HW-101475) 'Micro-Therm' pyrometer as an example, one can measure the temperature of the TITAN EBIT cathode to an accuracy of 0.5% in the range of 700-3200 °C. Measuring the glowing cathode's temperature allows the characterization of this property with respect to its set voltage. Knowing this property will allow more accurate calculations of the electron beam radius, as described previously in Section 3.2.5. Furthermore, should the measured temperature values change with respect to their normal associated voltages, diagnosis of the cathode's condition will be easier. It is expected that the measurement of the cathode temperature will be particularly useful when upgrading the TITAN EBIT to one of the two larger cathodes, thus ensuring the cathode is set to a reasonable operational temperature.

In addition to the prism, a channeltron and its two required electrical feedthroughs were also installed; one to apply high voltage and a second to measure the current. This device was installed to test ion injection efficiency into the trap with a calibrated source. The channeltron entry horn faces the trap, and can therefore, accept small currents (typically under 10^4 sec^{-1} [42]) of ions, which produce secondary electrons



Figure 3.31: The channeltron and prism installed between the magnet and electron gun chambers. As shown, the entire assembly is mounted upside down. The channeltron horn faces the collector and is in the middle of the beam path, when the linear feedthrough it is mounted on is fully extended. The prism can be used to reflect light from the cathode towards the left, out through a vacuum viewport.

upon striking the electrode. A channeltron is designed in such a way, that a potential is applied to the tip of the horn which attracts the charged particles. The particles strike the wall, producing secondary electrons, which are attracted further into the horn due to the resistive surface. The potential on the walls continues to decrease from its initial high negative value, as the distance from the entry point increases. As the electrons travel further into the horn, they strike the walls producing additional electrons, which are collected with an electrode consisting of a small metal plate at the end of the horn. This current is then read out as the channeltron current on the second electrical feedthrough (see Figure 3.32). As shown in Figure B.5, the frame that the channeltron rests on is also grounded to reduce possible noise during operation.

Due to the channeltron's magnetic field sensitivity and its proximity to the main

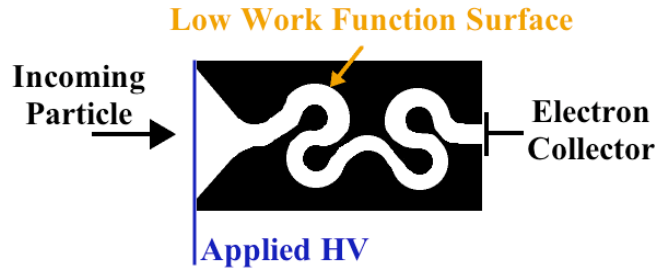


Figure 3.32: Channeltron schematic. Incoming particles are attracted to the entry horn of the channeltron and strike the surface creating secondary electrons. Due to the low work function and the surface resistivity decreasing the potential further down the channel, the electrons are pulled further into the channeltron, creating additional electrons. The multiplying electrons are then eventually collected and can be read out as a current proportional to that of the incoming particles.

magnetic field, it will not be able to operate correctly with strong fields. Other experiments suggest that with applied high voltages of around 4000 V, sufficiently high gain can be achieved for channeltron operation in fields of up to 300 Gauss [42]. Assuming the center of the channeltron is at the center of its housing chamber, which is attached to the magnet, it is 284.5 mm away from the center of the trap. With an applied field of 5.8 T, the simulated residual field at this position is 1230 Gauss. Scaling this result yields a maximum operational field of around 1.4 T, before the channeltron can no longer reliably provide a measure of the injected ion current.

Chapter 4

First Tests and Results

In the following chapter, the first tests verifying the functionality of the TITAN EBIT during progressive stages of development will be described. These include the first operation of the EBIT, using a set of provisional trap electrodes. This section also briefly accounts for the installation of various pieces, including the final trap electrodes. It also discusses the spectra acquired showing the presence of Ba and gas-injected Kr ions in various charge states, with their respective recombination emission x-ray lines. A measurement of the axial space charge in the trap as a function of the electron beam current is also reported.

4.1 Barium DR and Observed Charge States

The TITAN EBIT observed its first electron beam and subsequent highly charged ions using a provisional three electrode ion trap on June 20th, 2005. This provisional trap's central region was a single electrode, in contrast to the octupole segmentation of the final trap. Both traps had the same required observation ports cut into the electrode for ion/electron observation.

The first test runs were conducted with the cathode and collector at ground potential,

Table 4.1: Table of relevant Ba ionization energies for the presented results [3].

State	Ionization energy (keV)
He-like Ba ⁵⁴⁺	43.48
Li-like Ba ⁵³⁺	10.62
Be-like Ba ⁵²⁺	10.38
B-like Ba ⁵¹⁺	10.02
C-like Ba ⁵⁰⁺	9.74
N-like Ba ⁴⁹⁺	9.08
Ar-like Ba ³⁸⁺	2.82
K-like Ba ³⁷⁺	2.55
Ca-like Ba ³⁶⁺	2.45
Sc-like Ba ³⁵⁺	2.35
Ti-like Ba ³⁴⁺	2.26

as the high voltage cage was not yet operational. After the cathode filament was slowly allowed to heat up for the first time over approximately two weeks, the cathode was biased to a maximum of -2.5 kV. This procedure entailed floating the heating element and focus electrode, via their power supplies to a given potential (usually between -2 kV and -2.5 kV). The electrons then escaped from the cathode emitting surface, were pulled and shaped by the focus electrode, and further attracted by the anode, which was set at a positive potential of up to a few kilovolts. The electron beam then passed through the provisional trap, whose electrodes were set up to potentials around +10 kV. Background species were ionized (mainly Ba from the cathode itself), and their characteristic x-rays were detected via the same detection method (see Section 3.3.1) employed with the final trap.

The TITAN EBIT was then taken offline as the superconducting magnet was removed, the final trap electrodes were installed, and the two steerer/Einzel lenses were installed. Following this, the high voltage cage and the associated electronics and transformer were assembled and tested, the trap electronics were similarly completed, and various

4.1. Barium DR and Observed Charge States

high voltage tests were performed (see Section 3.2.1). The EBIT came back online on February 20th, 2006 and once again delivered in situ spectra of the background Ba ions with the final trap electrodes.

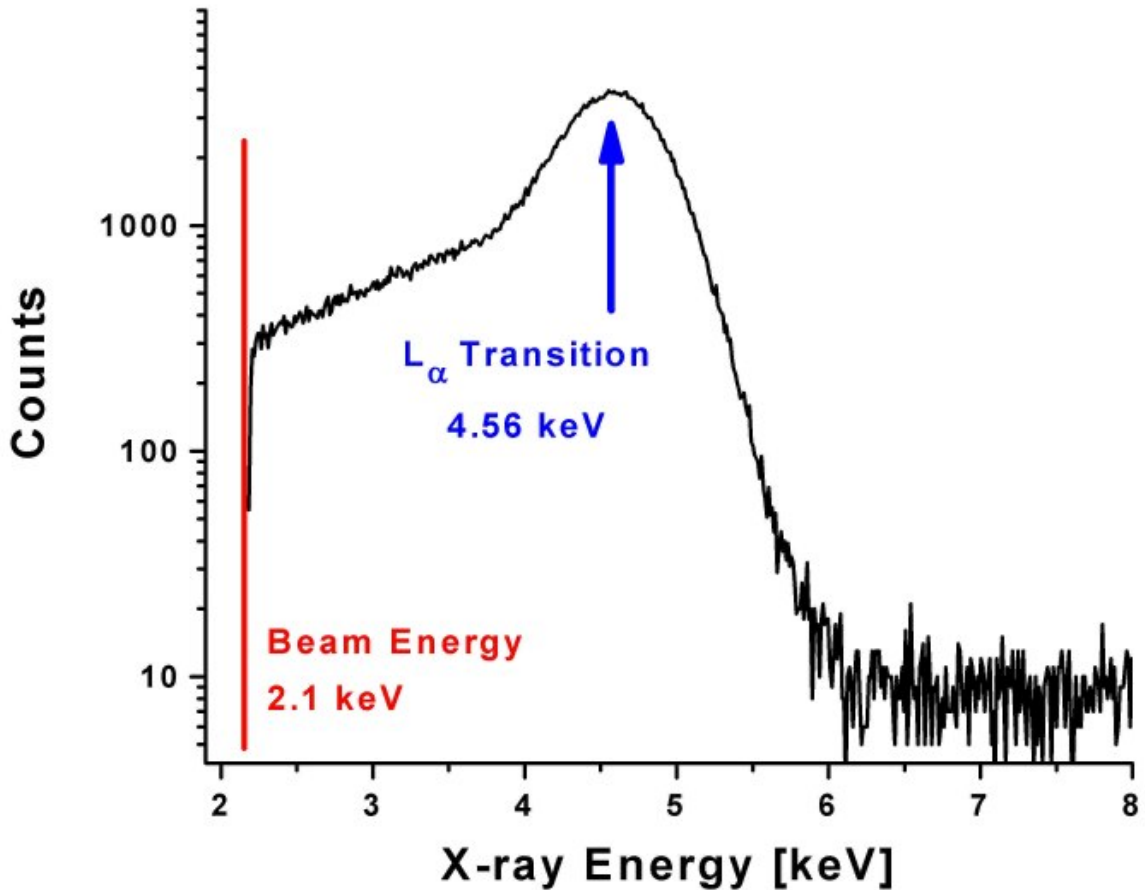


Figure 4.1: Spectrum of a DR resonance in Ba. The characteristic L_{α} line at 4.56 keV of Ba with a background of bremsstrahlung radiation from the electron beam is shown.

While the presence of Ba ions in the trap is both expected due to the cathode in use and clearly visible via direct excitation of transitions between $n = 3$ and $n = 2$ electronic levels, Ba's presence was again confirmed via dielectronic recombination. The electron beam energy was scanned manually around 2 keV by changing the potential of the trap electrodes in search of Ba's known DR resonances, which produce

characteristic Lyman- α radiation. It should be noted that these Ba DR results were for diagnostic purposes only, so the detector calibration was quickly done and no voltage divider was used to precisely determine the electron beam energy. The results do, however, illustrate the observed DR of Ba in the trap and will therefore be discussed.

The trap electrodes were connected so that the octupole trap electrodes were set by one power supply and all other trap electrodes by a second power supply. The cathode was biased to -1.8 kV and with a stable electron beam of 129 mA, the maximum resonance condition was found with the central trap electrodes at 799 V, corresponding to a total beam energy of around 2.6 keV, ignoring space charge corrections. Calculating the electron beam radius (using Equation 3.6) for these beam conditions ($B = 5.8$ T and T_c assumed to be ≈ 1350 K) yields a value of $26.5 \mu\text{m}$. Combining these values and using Equation 3.13 produces a radial space charge potential of around -470 V, decreasing the effective beam energy to about 2.1 keV.

Using the detection method as outlined in Section 3.3.1, it was evident that a DR resonance had been found when a peak at about 4.6 keV with 1200 counts per second became visible (see Figure 4.1). If the beam energy was decreased by just 78 eV (setting the central trap potential to 721 V), the count rate for the Ba DR peak would decrease to 980 counts per second. Beam energies further away from this resonance resulted in no visible peak.

For the final data analysis, the calibration of channel number to keV was done by fitting Gaussian functions to known x-ray peak values. ^{55}Fe 's typical emission at 5.890 keV and ^{109}Cd 's characteristic line at 88.04 keV were used for this calibration. Two additional ^{109}Cd x-ray lines, each comprised of two single emission lines that were not resolved in this experiment, were also employed. The values used correspond to the weighted mean averages, with respect to their relative intensities, at 24.932 keV and 22.105 keV [35]. The corresponding channel numbers and known x-ray energies were then plotted, and a linear fit was performed (see Figure 4.2).

4.1. Barium DR and Observed Charge States

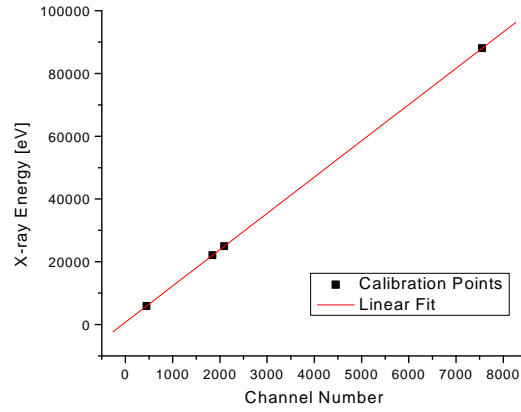


Figure 4.2: Energy calibration for the DR resonance in Ba. Characteristic lines from ^{109}Cd and ^{55}Fe sources were used. The linear fit resulted in a slope of 750 ± 20 eV / channel, a constant 11.558 ± 0.005 eV, and a reduced χ^2 of 1.0.

The Ba DR peak at 4.6 keV, as also observed and explained by D.J. McLaughlin et al. with the NIST EBIT [74], contains the Ba L_α DR transition in addition to a contribution from radiative recombination into Ba's $n = 3$ shell. As evident by referring to the ionization energies of Ba in Table 4.1, ionization states as high as Ba^{36+} were created, allowing radiative recombination into the $n = 3$ shell. The DR transition seen at 4.6 keV corresponds to one of the M-shell electrons (3d) radiatively decaying into a 2p vacancy, thereby emitting an x-ray that has twice the kinetic energy of the incident electron.

To confirm that higher beam energies could be produced by floating the electronics for the cathode and collector in the high voltage cage, a lead from a negative power supply (FUG HCN14-20000) was attached to the copper grounding bar, which was mounted on the rack inside the HV cage (see Figure B.7). (For further details on the transformer and associated connections, see Section 3.1.6.) Following a similar procedure as described above, a stable electron beam was created before the collector and electron gun were floated to -20 kV (trap electrodes at 5 kV, cathode at -2 kV),

raising the beam energy (ignoring space charge) to 27 keV, capable of producing He-like Ba^{54+} (see Figure 4.3). As expected, the increase in beam energy resulted in the shifting of the RR peaks for Ba, while the direct excitation transitions, such as those between shells $n = 3$ and $n = 2$, remain the same at about 5 keV.

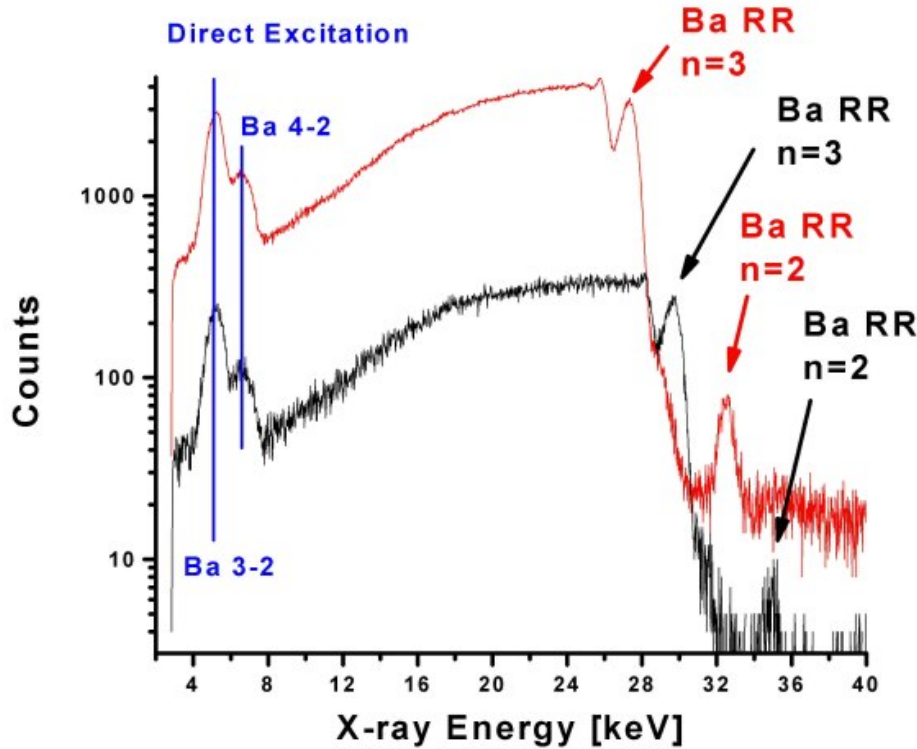


Figure 4.3: Two overlaid Ba spectra with electron beam energies of 23 keV (red line) and 25 keV (black line). The constant energies of the direct excitations involving the Ba $n = 4$ and $n = 3$ to the $n = 2$ shells can be seen in addition to the RR transitions into the $n=2$ and $n=3$ shells of Ba which increase in energy as the beam energy increases.

The energy axis for Figure 4.3 was calibrated using four of the characteristic emission lines (see Table 3.7) from a ^{241}Am source. The electron beam energy was approximated using the Rydberg formula: $\hbar\omega = E_e + \text{Ry} Z^2 \frac{1}{n^2}$, as the beam energies associated with these sample spectra were not recorded. This is due to a combination of acquiring hundreds of data sets and incomplete notes. The variables used here include: Rydberg's

4.1. Barium DR and Observed Charge States

constant $Ry = 13.6$ eV, the effective nuclear charge Z , and an integer representing the final energy state that defines the photon's energy n . The radiative recombination process investigated here involves a continuum electron and a beam energy over 10.6 keV, which is high enough to produce He-like Ba^{54+} (see Table 4.1). This yields an effective nuclear charge of 54 and $n = 2$ or 3, depending on the atomic shell of the specified RR process. The resulting atomic binding energies from this formula can then be subtracted from the energies at which the peaks for these processes occur, yielding consistent beam energies (23 and 25 keV) for RR into both shells for both spectra. Such estimates for the atomic binding energies of Ba into these shells are in agreement (within 0.3 keV at beam energies of 14 keV) with Ba RR into the $n = 2$ shell data from Martínez [72].

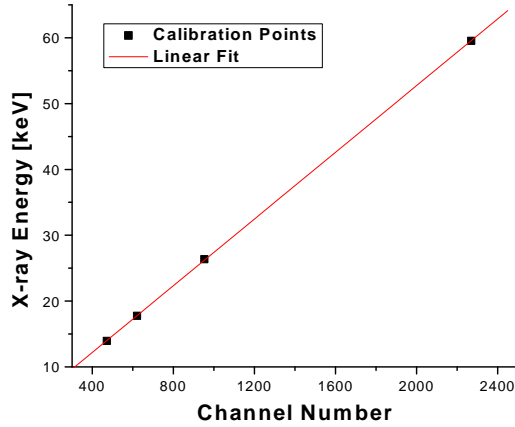


Figure 4.4: Energy calibration for the Ba spectra using electron beams of over 20 keV. Characteristic lines from an ^{241}Am source were used for the energy axis calibration. The linear fit resulted in a constant of 2.05 ± 0.10 keV, a slope of $(2.534 \pm 0.008) \times 10^{-2}$ keV / channel, and a reduced χ^2 of 0.99.

Table 4.2: Table of some Kr ionization energies [91].

State	Ionization energy (keV)
H-like Kr ³⁵⁺	17.936
He-like Kr ³⁴⁺	17.297
Li-like Kr ³³⁺	4.109
Be-like Kr ³²⁺	3.966

4.2 Krypton Dielectronic Recombination

After the successful observation of highly charged Ba ions, the gas injection system (see Section 3.1.4) was tested using Kr gas. Kr was chosen as it was readily available, its spectrum has been well characterized, and it can be bred up to the He-like charge state at beam energies above 4.1 keV (see Table 4.2). It should be noted that these Kr results were for diagnostic purposes only, so the detector calibration was quickly done and no voltage divider was used to precisely determine the electron beam energy. The results do, however, illustrate the observed DR of Kr in the trap and will therefore be discussed.

A stable 156 mA electron beam was allowed to pass through the trap electrodes with the cathode biased to -1.9 kV. Kr gas was then introduced via the multi-chamber differential pumped gas injection system, with a pressure in the order of 10^{-6} mbar. The atomic beam of Kr crossed the path of the electron beam, producing ionized Kr. The trap electrodes were connected in a simplified fashion, with the eight segmented center electrodes at one potential and the two sets of four electrodes on either side of these at a lower potential. The trap electrode potentials were then varied to find the known Kr KLL or $n = 2$ to $n = 1$ DR resonance (see Section 2.2.2) which would be indicated by a sharp increase of counts at an x-ray energy of about 13 keV in the germanium detector spectrum. The large background from Ba $n = 3$ and $n = 4$ shells

4.2. Krypton Dielectronic Recombination

to the $n = 2$ shell transitions at lower energies (around 5 and 7 keV respectively) was partially blocked using aluminum and paper in front of the detector as absorbers of x-rays.

The spectrum shown in Figure 4.5 illustrates the resonance condition found when the central eight electrodes were at 7.68 keV and the outer eight electrodes were at 7.56 keV. After calculating the Herrmann electron beam radius (Equation 3.6 with $E_e = 9.58$ keV, $B = 5.8$ T, $T_c \approx 1350$ K, $I_e = 156$ mA) to be $26.3 \mu\text{m}$, the resulting radial space charge correction (Equation 3.13 with $r_{Trap} = 7$ mm) was around -300 V. Therefore, the effective electron beam energy was 9.3 keV. When the potential applied to the trap electrodes was changed by tens of eV, the DR resonance condition was lost, resulting in the blue or lower curve in Figure 4.5.

The above mentioned applied electrode potentials formed an inverted trap with a magnitude of 120 V. As discussed previously in Section 3.2.6, the estimated axial space charge (Equation 3.16 with $r_{C1} = r_{G1} = 2.5$ mm) modifies the effective or net trapping potential. Using the already mentioned beam characteristics, this space charge correction is about -50 V, yielding a positive potential of 70 V (an inverted trap). Considering that charge states up to He-like Kr were produced and observed, the existence of an inverted trap where ions could not stay or possibly even pass through, is impossible. If, however, the experimental axial space charge results (see below) are used to determine the added trapping potential, a net trapping potential of -107 V is produced. This result is realistic as it would allow the production of highly charged Kr by avoiding a deep potential well where heavier Ba ions could ‘crowd out’ the lighter Kr ions.

As the known KLL transition populated by dielectronic recombination at 13 keV [36, 72] was approached, the count rate of this individual peak dramatically increased up to 250 counts/s, clearly indicating the presence of a resonance. Common EBIT background ions, such as Ba and W from the cathode, have no resonances emitting

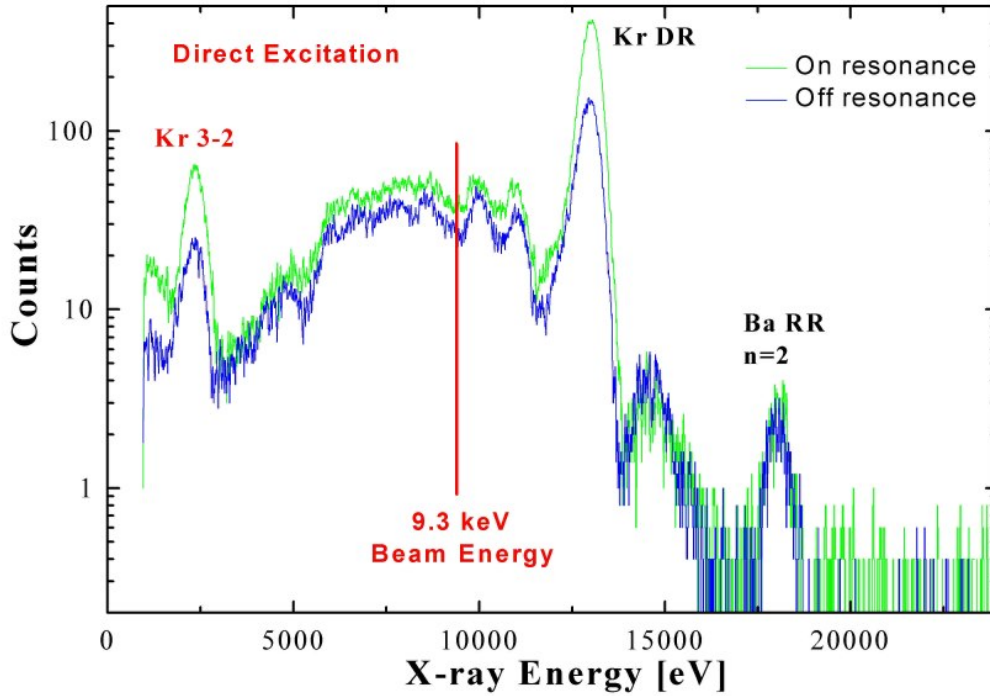


Figure 4.5: Spectrum of the KLL DR resonance in Kr at 13 keV using a beam energy of 9.3 keV. This DR peak is broadened by RR into the $n = 2$ shell of Kr. Background ions such as Ba were also present in the form of direct excitations and RR. Note that neighbouring data points (four) from these two data sets have been used to produce an averaged spectra for clarity.

x-rays at an energy of 13 keV at this beam energy, however, the injected Kr gas does. The peak at this energy would also vanish after a few minutes, if the gas inlet valve was closed. It was, therefore, concluded that Kr was the source of the resonance. Thus, this peak was the result of DR from ion species such as Kr^{34+} to Kr^{30+} (C- to He-like Kr) which have strong KLL resonances in this energy range. Due to the nature of RR, this process occurred simultaneously, producing photons of similar energies.

As binding energies for Kr's $n = 2$ shell in highly charged ions are around 3.5 - 4 keV [3], and x-ray energies from RR processes are given by the summation of the electron beam energy and the atomic binding energy into the ion's respective shells, RR overlaps the DR peak at 13 keV, effectively broadening it. RR transitions of Ba

4.2. Krypton Dielectronic Recombination

into the $n = 3$ shell also occur at around the same energy; hence, the highest peak, when the resonance condition was not fulfilled, contained the RR of Kr and Ba. Kr's RR into the $n = 3$ shell (with atomic binding energies of around 1 to 1.7 keV [3]) around 10.3 - 11 keV at this beam energy was not prominent, due to other RR lines in the same energy range.

The direct excitation of Kr between shells $n = 2$ and $n = 3$ was also detected. After the KLL Kr DR decay, a process which emits a 13 keV photon, a $1s^22p$ state is created. This state can then decay to a $1s^22s$ state, emitting a photon with an energy of about 2.3 keV [64]. Alternatively, the direct excitation of the $1s^22s$ state can also produce the observed photon energy when it decays.

The highest detected energy peak around 18 keV was identified as the RR of Ba^{47+} into the $n = 2$ shell [64]. While a beam energy of around 9.3 keV would be high enough to ionize Ba^{49+} (see Table 4.1), a shallow trapping potential of about -100 V, combined with the presence of the injected lighter Kr ions, would not facilitate the creation of significant higher charge state populations in Ba. The remaining observed peaks include various direct excitations and RR transitions of W and Ba, expected background ions from the cathode.

Given that the Kr KLL DR and RR transitions into the $n = 2$ shell confirm the presence of $Kr^{30+...34+}$, it has been demonstrated that the gas injection system is operational.

While it was not yet possible with the TITAN EBIT experimental setup, a slow, systematic scanning of the electron beam energy around Kr's KLL DR resonance, when coupled with a high resolution germanium x-ray detector, can allow one to differentiate between the different charge states of Kr via their corresponding KLL relative intensities at slightly different beam energies [72].

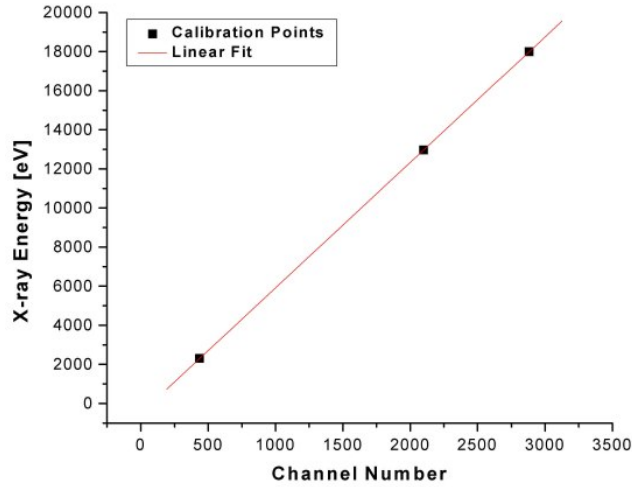


Figure 4.6: Energy calibration for the DR resonance in Kr. The linear fit using Kr’s $n = 3$ to $n = 2$ transition at 2.3 keV, Kr’s DR resonance at 13 keV, and the RR of Ba into the $n = 2$ shell at 18 keV resulted in a constant of -496 ± 7 eV and a slope of 6.415 ± 0.003 eV/channel.

4.3 Axial Space Charge

Using a stable electron beam with typical experimental parameters as outlined in Table 4.3, the axial space charge trapping potential as a function of the electron beam current was measured. Once again, the same germanium detector setup was used to observe x-ray emission from the highly charged ions in the trap. The central trap electrodes (one to eight) were set at 5 kV, while the remaining side electrodes were set at various lower potentials by a second HV power supply. At a given electron beam current, the side electrode potential would be increased from 4 kV to the point at which x-rays from ions in the trap were observed. It was assumed that ions were beginning to collect in the trap as this signal would increase from about zero with a 1 kV inverted trap (potential hill), to 5 counts/s at the onset of the signal. The count rate would then slowly increase as more ions were trapped. If the inverted trap was a few volts too small, the count rate would spike within a couple of seconds to hundreds of counts/s. As the potential was overshoot and the trap appeared to be filling too

4.3. Axial Space Charge

quickly, the data point for this current level was then redone.

Table 4.3: Typical TITAN EBIT operational parameters (used while measuring the axial space charge).

Cathode	-1.80 kV
Collector coil	8.9 A (4.2 V)
Bucking coil	19.5 A (6.0 V)
Trim coil	3.39 A (6.46 V)
Cathode heater	1.44 A (7.11 V)
Central trap electrodes	5.00 kV
B field	5.80 T
Extractor and back shield electrodes	-2 kV
Suppressor and front shield electrodes	0 kV

It was believed that when ions were seen in the trap, the axial space charge potential (Equation 3.16) created by the electron beam passing through the trap electrodes with varying diameters (see Section 3.2.6), had been balanced by the applied inverted trap created by the trap electrodes. The recorded voltages at which this occurred are plotted as a function of the beam current in Figure 4.7.

Upon first inspection, the inferred axial space charge potential linearly increases with the electron beam current, agreeing qualitatively with the calculated plot in Figure 3.27. The slope of the measured results, however, is over four times larger than the calculated result (see Figure 4.7). The offset of about 40 V was removed as this can be reasonably explained by the relative accuracy of the power supplies at 5 kV. Once this offset is removed, the unusually large slope compared to the expected value as shown in Figure 4.8 remains.

It is clear that the measured and calculated axial space charge results do not agree. This suggests that a more complicated process was measured either accidentally, due to a poor experimental setup, or that the axial trapping in an EBIT is not fully understood.

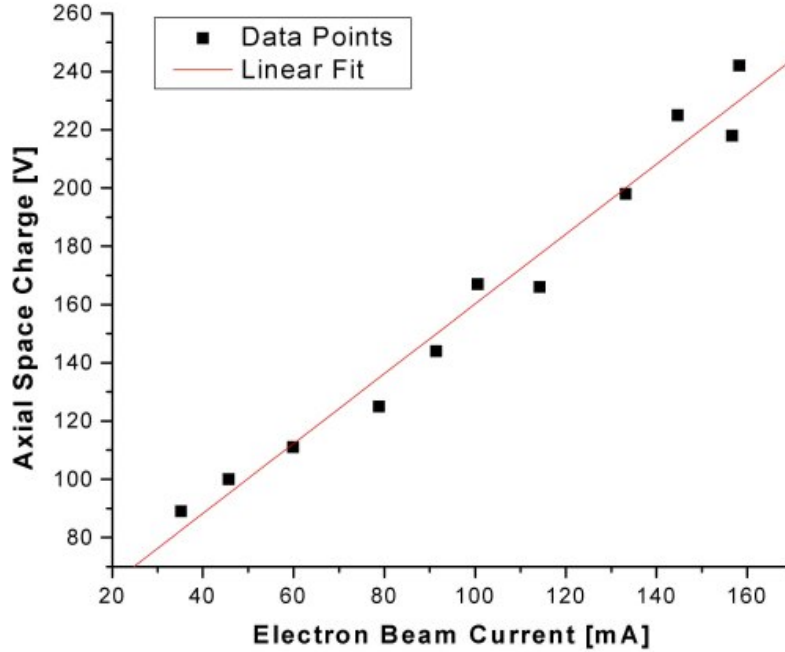


Figure 4.7: Inferred axial space charge potential plotted as a function of electron beam current I_e . A linear fit of the data produced a slope of 1.20 ± 0.07 V/mA, a constant of 40 ± 7 V, a reduced χ^2 of 0.99, and a standard deviation of 9 V.

The assumption that ions were beginning to become trapped could be at fault, as the ions could conceivably be passing through the trap and emitting x-ray radiation at the same time. This, however, would not explain the gradual increase of the x-ray signal with time, signifying at least increased ion traffic through the trap.

An effect that has been ignored until now, namely, the effect of positive charges could possibly explain part of the observed results. This effect normally concerns the beam energy, as the space charge potential generated by the ions can help counteract the potential created by the electron beam. Since in this particular case there should not be any ions in the trap, it is conceivable that positive ions are ionized by the electron beam just outside of the central trapping area. Perhaps having additional positively charged ions in the neighbouring cylindrical electrodes could create what appears

4.3. Axial Space Charge

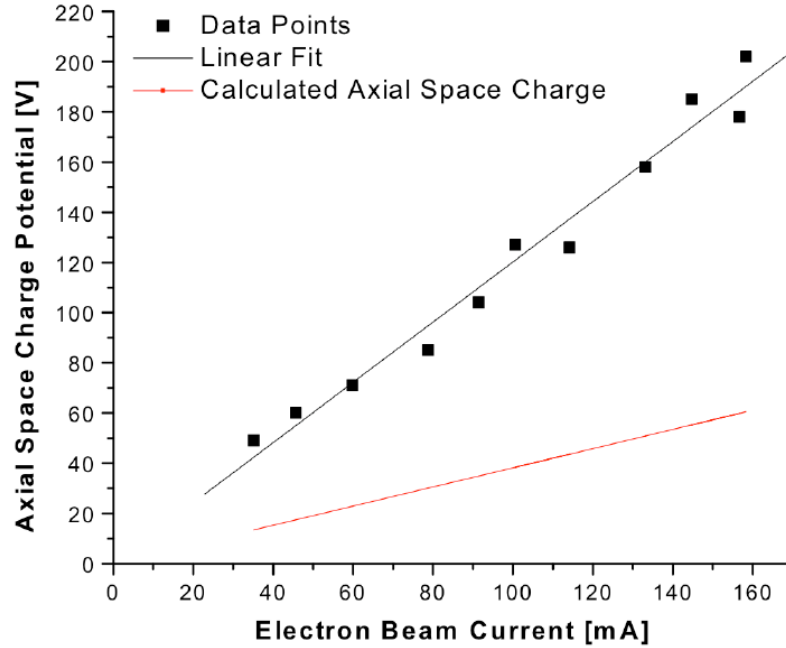


Figure 4.8: Measured and calculated axial space charge plotted as a function of electron beam current I_e .

to be a deeper potential well than expected. After the threshold has been crossed (i.e. the axial space charge potential is balanced by the applied potential), ions would begin collecting in the trap. These ions, however, would be repelled by the collected positive charges in the neighbouring electrodes, essentially creating a deeper well.

Another possible explanation for the disagreement between the measured and calculated axial space charge potential lies in the assumption that the electron radius is constant. The magnetic field of the superconducting coils was simulated by [80] using a program called TRAK. This data has been plotted and the scales have been matched (± 2 cm) to a cross-section of the EBIT as shown in Figure 4.9. As is expected, the magnetic field drops off very quickly as $1/r^3$. This dramatic decrease, however, occurs in the trap electrodes, which would allow the beam to start expanding. Additionally, the dip in the magnetic field at the center, which is expected in non-ideal Helmholtz

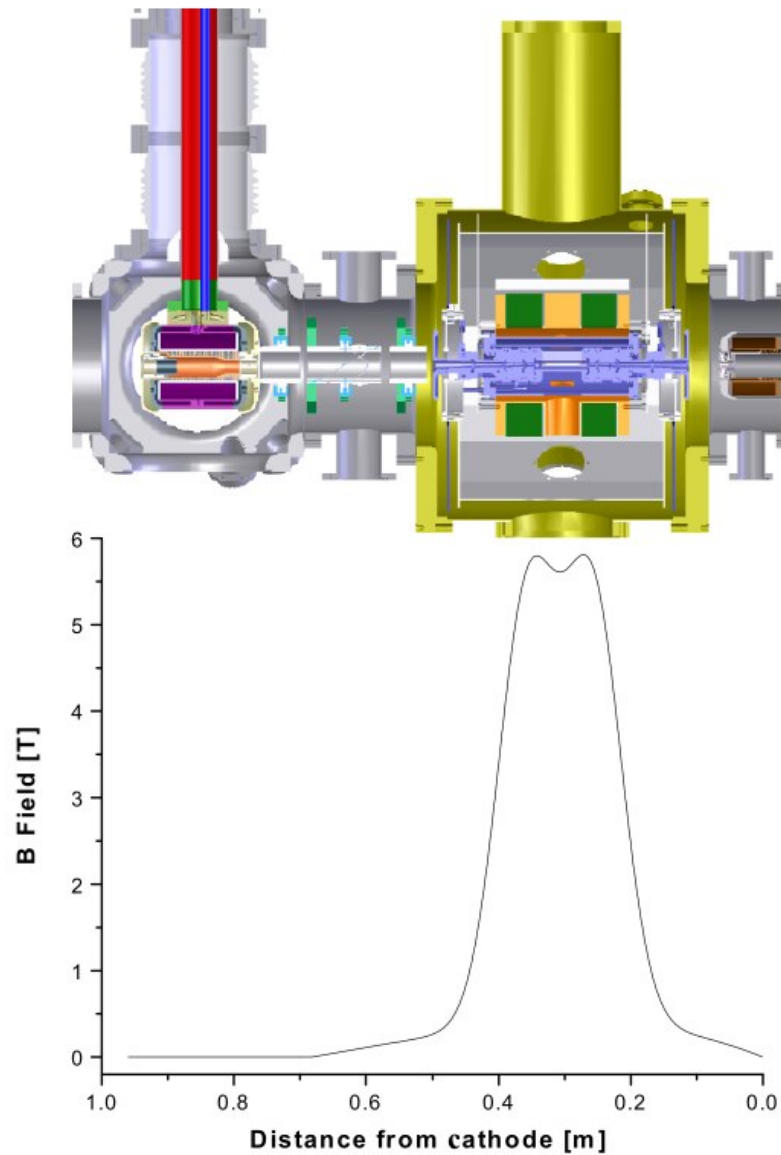


Figure 4.9: Cross-sectional view of the TITAN EBIT with the axial magnetic field strength plotted below (simulated B-field data from [80]). The B-field created by the superconducting coils is at a maximum in the trapping region and about zero at the cathode (not shown) for electron beam compression.

coils, would also effect the radius of the electron beam. The resulting variations, however, would have to be on the order of 15% for a change in radius of 8% (using

4.3. Axial Space Charge

the beam conditions from the Kr DR results above). In contrast, the variation in the plot is roughly only 5%. Using the experimental axial space charge potential values to determine the magnitude of the required radial change (assuming that the electron radius is $26.3 \mu\text{m}$ in the central trap), yields an impossible electron beam radius of over $500 \mu\text{m}$ in the adjoining electrodes. While magnetic field variations may play a role in explaining this observed axial trapping potential, it is clear that it can not solely account for this effect.

It is, therefore, concluded that further study is required. Additional experimental results using other EBITs should be performed and the theory used to predict the added axial trapping potential should be further investigated. Due to the similarities between the TITAN and TESLA EBITs, additional studies using both of these devices is planned.

Chapter 5

Conclusion and Outlook

5.1 Conclusion

The goal of this thesis has been to assemble, characterize, and commission a charge breeding EBIT for precision enhancement of the mass measuring capabilities of the TITAN project. This was accomplished at the MPI-K in Heidelberg before the EBIT was transported to TRIUMF.

The observed x-ray spectra confirm that the cathode performs as expected, providing background Ba ions, the presence of which, was confirmed through dielectronic recombination, producing L_α x-rays at 4.56 keV using an electron beam energy of 2.36 keV. Ba ions were also used to demonstrate the capability of floating the electron gun and collector to produce high energy electron beams. Thus far, electron beams of up to 27 keV were demonstrated, creating charge states as high as He-like Ba⁵⁴⁺. This required floating the collector and electron gun and their respective electronics in the HV cage to -20 kV, applying 5 kV to the trap electrodes, and an additional -2 kV applied to the cathode. The two overlaid x-ray spectra at beam energies of 23 and 25 keV (see Figure 4.3) clearly show radiative recombination of Ba into the $n = 2$ and $n = 3$ shells, which naturally appear at higher energies as the electron beam energy is

also increased.

The functionality of the gas injection system to introduce a collimated atomic beam of neutral gas into the trap region which is subsequently ionized, was also demonstrated. Kr ions were successfully produced, reaching charge states of up to Kr^{34+} , using an electron beam with an energy of 9.3 keV. The characteristic KLL dielectronic recombination of Kr at 13 keV was observed, in addition to the radiative recombination of Kr into the $n = 2$ shell and other background Ba transitions.

The discrepancy between the measured and calculated axial space charge potential remains unexplained. More thorough theoretical treatment may be required such as considering the effect of the changing magnitude of the magnetic field and the resulting change in the electron beam radius or the possible buildup of positive charges in neighbouring electrodes and the resulting potential changes. Additional experiments with EBITs such as the TITAN and TESLA EBITs may also help to elucidate this situation.

To date, the TITAN EBIT has produced a maximum electron beam current of 500 mA, with stable electron beam currents around 400 mA. Therefore, the maximum theoretical production of the currently installed cathode (about 500 mA) has been achieved, and the future installation of one of the two larger cathodes should allow the TITAN EBIT to produce electron beam currents of up to 2 or 5 A, increasing the present maximum achieved beam current with any EBIT by an order of magnitude. Based on these first results, the TITAN EBIT is ready to become incorporated into the TITAN experimental setup and to be ultimately used for the production of highly charged ions for precision mass measurement. The results of such measurements with short-lived radioactive isotopes will help to decrease the uncertainty of the V_{ud} term in the CKM matrix as discussed in Chapter 1. In addition to these important contributions to fundamental physics research, the TITAN EBIT will be uniquely situated to expand atomic spectroscopy of highly charged ions to include rare isotopes

produced with ISAC at TRIUMF.

5.2 Outlook

After the above successful results, the EBIT partial disassembly, and move to Vancouver, the EBIT is in the process of being installed on the TITAN platform in the ISAC I experimental hall. This will involve the reconnection of power and water, the removal of the transport holders for the electron gun and collector and restoring vacuum to the entire system. After sufficient pumping time, the cathode filament will be warmed up, and tests will ensure the system is still successfully operating after being transported. Once this has been verified, various options are available to prepare the EBIT for successful charge breeding and subsequent mass measurements. These options to further understand and optimize the TITAN EBIT for charge breeding are described below.

Ion extraction from the TITAN EBIT, while briefly demonstrated in Heidelberg, should be performed and documented to optimize future extraction to the TITAN system. This should ultimately involve the use of timing electronics to coordinate bunches from the EBIT for injection into the precision Penning trap. After a scheme to lower and raise the collector side of the trapping potential well has been chosen, the electronics and appropriate switches to quickly change the potentials must be purchased, installed, and tested. An approach to optimize extraction could involve attaching a magnet to the EBIT beam line near the outermost steerer lens. The magnet would allow one to perform a charge over mass scan with the help of an ion detector, allowing the identification of the detected ion species and subsequent optimization of the extraction process.

Similarly, ion injection should also be attempted and optimized to determine the appropriate trap electrode and ion optic settings. This will yield a greater variety of

ions to study spectroscopically from those that can only be introduced in a neutral gaseous state. The additional range of ions will also allow the charge breeding of injected rare isotopes for extraction into the precision Penning trap mass spectrometer. As mentioned previously in Section 3.3.2, the installed channeltron mounted with the prism between the trap and the electron gun, if desired, could be used to help test injection efficiencies, provided the applied magnetic field is no greater than 1.4 T. This test, however, would only determine the injection efficiency of ions into the trapping region with a weak B field and without the electron beam. A second moveable detector to measure the rate of the injected ions before they enter the trapping region might also have to be installed for accurate comparison.

A test of great importance to the TITAN project is the measurement of the emittance and ion temperature of the extracted ion beam of highly charged ions from the TITAN EBIT. While previous emittance results from EBITs have been published [73], the extracted ion temperature has never been determined. While a number of ion temperature measurements in an EBIT trap have been performed [57, 73], more accurate values and knowing their dependence on such parameters as the electron beam current would be very helpful. These results would clarify the extent of ion cooling needed and therefore help establish limits on the lifetimes of ions that can be successfully produced, charge-bred, cooled, and measured before they decay. The emittance would also allow the determination of the ion transport efficiency from the EBIT to other TITAN devices.

Additional properties of the extracted beam that would be of interest are its size and position. One method of measuring these quantities would be to use four adjustable electrodes, two on each axis, that could be moved together, closing an aperture for the extracted ion beam. The amount of the current on the aperture electrodes, created by the impinging ions, would allow the determination of the ion beam's size and position. Depending on the extracted ion current, an MCP could also be used for this test. Such

5.2. Outlook

an experimental setup would also facilitate the full characterization and optimization of the steerer lenses to determine if they can steer ions along one axis independently from the other.

As mentioned previously in Section 3.1.2, taking advantage of the radial segmentation of the central trap electrodes should also be investigated. Measuring the induced image charge on the trap electrodes due to the charge contained inside the trap could offer insight into the charge distributions of the ions and the electron beam. Using the electrodes to perform RF excitation or resistive cooling would be additional avenues to explore. Another possible option would be to apply a small electric field perpendicular to the trap axis, inside the central trapping region. This could conceivably give insight into the distribution of ion charge states and methods of altering charge breeding rates.

As mentioned in the conclusions above, the TITAN EBIT should be upgraded in the future with the already designed housing for the two larger cathodes, providing higher current capabilities and the corresponding faster charge breeding times. After installation and characterization of the new cathodes, it may prove useful to use a pyrometer to analyse the light reflected by the installed prism (see Section 3.3.2 for more details) to measure the temperature of the cathode. This would yield a more accurate value for the electron beam radius, which is inherently used to calculate the electron density, affecting the cross sections and rates of the reactions occurring in the trapping region of the EBIT.

Finally, additional radial ports could be used in the future for other detector arrangements, including mounting detectors closer to the trapping region for particularly low concentration species and the installation of quartz windows to allow visible light spectroscopy of the trapped ions.

Appendix A

TITAN EBIT Brief Operation Manual

A.1 Start Up Procedure

Beginning with everything off:

1. Ensure that the vacuum levels are at standard values, that there is a main magnetic field at the desired field strength, that ALL EBIT electrodes and power supplies are off (excluding the heater power supply), that grounding cords are connected to the HV cage and EBIT support structure, and that any other necessary safety precautions have been taken.
2. Confirm that the electron gun is at normal operational position, or move it there after opening the required gate valve.
3. Ensure that the cathode heating power supply has been heating the already used cathode filament for at least 10 minutes (otherwise initial electron beam currents will be extremely low).

4. Set the collector's extractor electrode (the electrode furthest away from the electron gun) to a potential at least 200 V more negative than you intend to apply to the cathode power supply.
5. Set the trap electrodes to the desired positive values.
6. Set the bucking and collector coils to around their respective default starting values.
7. Turn on the cathode power supply to float the heater and focus electrodes. You should now be able to read the beam current via the collector return current.
8. Turn up the heater voltage to increase the beam current (typical operation is around 6.5 V).
9. Tune the collector and bucking coils in addition to the anode voltage to minimize the current impinging on the anode electrode.
10. To further increase the beam current, increase the focus voltage, retuning as the beam current increases.

A.2 Shut Down Procedure

1. Note: This procedure assumes that this is not an emergency shut down. Turn down the focus voltage and turn this power supply off, turn down the heater voltage (to ≈ 4.5 V), and turn down the cathode voltage to zero before switching off the high voltage.
2. The beam current should be decreasing. Reduce the anode voltage to zero before turning this power supply off.

3. With no electron beam current passing through the EBIT, the trap electrodes may be turned down as well as the bucking, trim, and collector coils. The collector's extractor electrode may be turned off, but only if the high voltage switch on the cathode power supply is off! The remaining collector electrodes may be turned off as well.

A.3 Venting the EBIT System - Excluding the Cathode Chamber

17/06/06, see Figure A.1 for the vacuum system schematic diagram.

1. Ensure that the EBIT vacuum system is fully operational with vacuum levels of better than 10^{-7} mbar in all chambers. (The backing pressure should be around 10^{-6} mbar.)
2. Ensure the electron gun head is retracted and the gate valve between the cathode chamber and the superconducting magnet is closed.
3. Close the valve connecting the exhausts for the collector and magnet turbo pumps. Important Note: This isolates the cathode chamber and ensures it is continuously pumped as the cathode should NOT be exposed to air.
4. Collector and magnet turbo pumps are deactivated via their respective controllers.
5. Close the KF valves directly attached to the collector and magnet turbo pumps. This will help to decelerate the turbo pump blades and prepare for venting nitrogen into the system.

6. Open to atmosphere the now isolated vacuum piping between the collector and magnet and cover the the open pipe end with aluminum to limit the entry of dust. Connect the nitrogen source to the other open end (the exhaust port of either the collector or magnet turbo pump as opposed to the vacuum pipe). Ensure that the nitrogen begins to flow before connecting it to the turbo pump exhaust port to avoid excess amounts of air venting into the system. Use a T-piece with a standard blank KF and rubber O-ring without clamp in a vertical orientation (or a similar system) to avoid blowing the beryllium window which could occur if the system becomes over-pressurized.

7. Wait until the collector and magnet turbo pumps have stopped. This time varies with backing vacuum pressure, increasing with better (lower) backing vacuum (recommended minimum time: 7 minutes).

8. After the two turbo pumps have stopped, slowly allow nitrogen into system by watching the vacuum pressure increase. Gradual pressure changes are essential for the continued functionality of the installed, thin beryllium windows. Use an external pressure gauge to ensure that the pressure does not go above 1.1 bar. Note that ion gauges do not function properly with vented nitrogen so one atmosphere of actual pressure will read around 300 mbar. At this high pressure, the accuracy of the gauges will also lead to significant reported fluctuations.

9. When opening up the vacuum system to replace flanges, install/remove pieces, and other work, ensure that nitrogen is flowing out of the system to reduce the amount of air, dust, and water vapour that can get into the vacuum system.

A.3. Venting the EBIT System - Excluding the Cathode Chamber

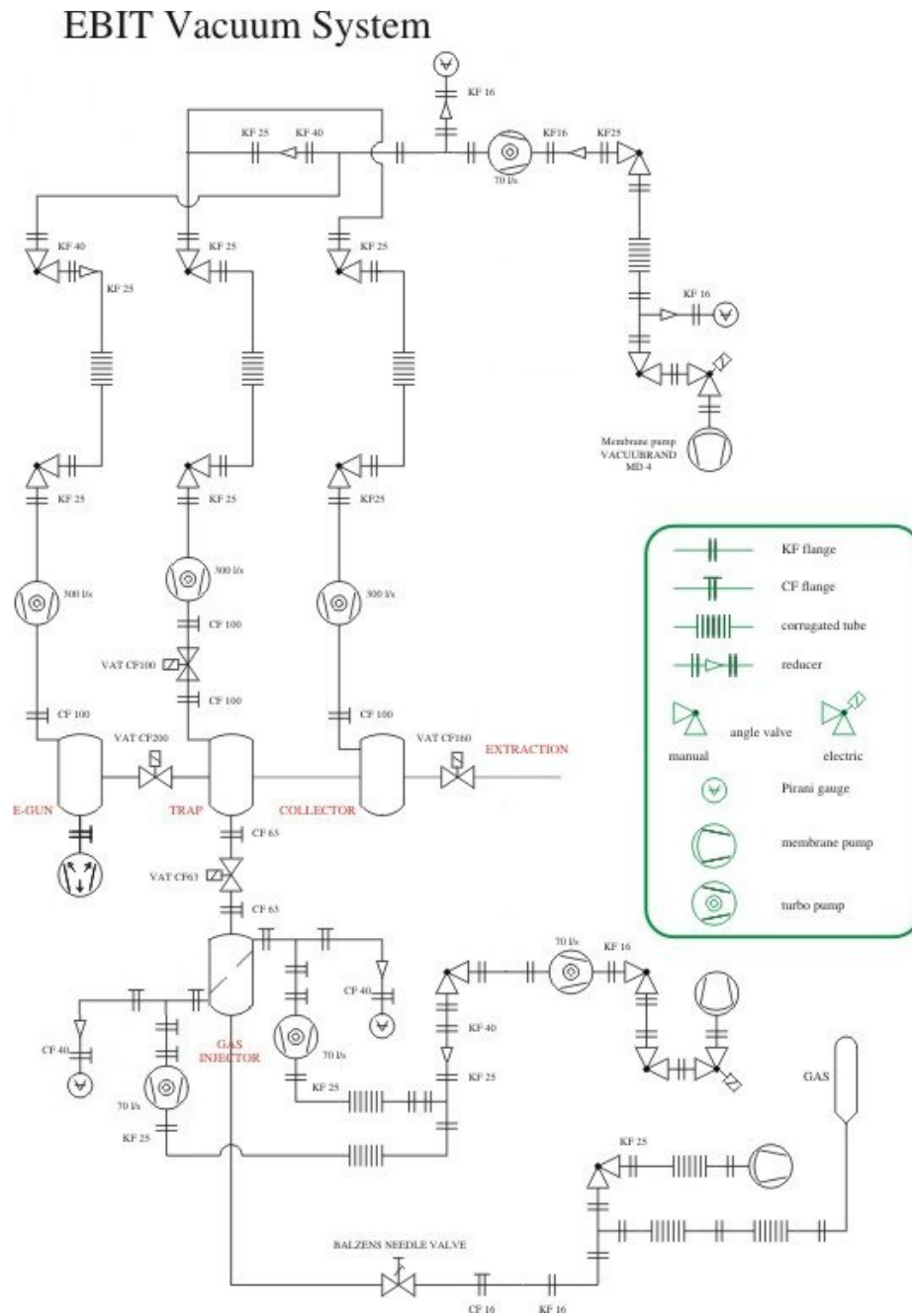


Figure A.1: Schematic of EBIT vacuum system from 2005 (modified from [88]). Vacuum gauges on the three main chambers (collector, magnet, and electron gun) are not depicted.

A.4 Restoring the High Vacuum

1. Ensure that all of the opened flanges are properly closed; then close the valve mounted on the turbo pump allowing the nitrogen into the system. Turn off the nitrogen source and disconnect it from the vacuum system. Reconnect the backing hose that connects the collector and magnet turbo exhaust ports.
2. IMPORTANT: Isolate the cathode turbo pump from the fore vacuum turbo pump by closing the valve between the pipe leading to the cathode turbo pump exhaust and the fore vacuum pump.
3. Turn the fore vacuum turbo pump off; then slowly close the valve between this turbo pump and the roughing pump to accelerate the turbo pump blade deceleration.
4. Turn the roughing pump off (optional) and wait for the fore vacuum turbo pump blades to stop rotating. When the fore vacuum pressure approaches 10^{-1} mbar, open the valve between the backing vacuum turbo pump and the vacuum pipe connecting the collector and magnet turbo pumps.
5. Turn the roughing pump on and open the valve between the roughing pump and the backing vacuum turbo pump. After the air has been pumped out of this part of the system (the fore vacuum pressure is ≈ 20 mbar), open the valves on the exhaust ports of the collector and magnet turbo pumps to begin pumping the nitrogen out of the system.
6. Wait until the collector and magnet pressure is ≈ 10 mbar before activating the collector and magnet turbo pumps. Start the backing vacuum turbo pump (low speed setting).

A.5. Venting the Backing Vacuum System

7. Ensure that all of the three turbo pumps attain normal operation and that their respective cooling fans are functioning, WAIT until backing vacuum pressure is restored to 10^{-5} to 10^{-6} mbar BEFORE opening valve between the backing vacuum and the cathode turbo pump exhaust. Do not forget to open the cathode turbo pump exhaust valve! Check to make sure the cathode chamber vacuum and the cathode turbo pump power level returns to approximately pre-venting values.

A.5 Venting the Backing Vacuum System

1. Ensure the EBIT vacuum system is fully operational with vacuum levels of better than 10^{-7} mbar in all chambers (the backing pressure is around 10^{-6} mbar).
2. Close the valves connected to the exhaust ports of the collector, cathode, and magnet turbo pumps. Note: The backing vacuum must be reinstated after around an hour to ensure the high vacuum system does not shut down due to turbo pump overheating.
3. Deactivate the backing vacuum turbo pump. Connect the nitrogen source to the blank port of the roughing pump. Start the flow of nitrogen prior to connecting the source to the vacuum system. Note that the nitrogen is not yet flowing into the system as this port is behind a closed valve.
4. Close the valve between backing vacuum turbo pump and roughing pump, turn the roughing pump off, and wait for the turbo pump to stop. This should not take long as the exhaust pressure of the backing vacuum turbo will be a few mbar. Once the backing pressure reads 10^{-1} mbar, enough time has passed.
5. Open the valve between the nitrogen source and the roughing pump, then slowly

open the valve between the roughing pump and the backing vacuum turbo pump. If the backing pressure is increased due to the introduction of nitrogen gas, but temporarily drops, the turbo pump blades are still rotating.

6. Note that ion gauges do not function accurately with mainly vented nitrogen so one atmosphere will read around 300 mbar. At this high pressure, the accuracy of the gauges will also lead to significant fluctuations.
7. When opening the vacuum system to install, replace, or remove pieces, ensure that nitrogen is flowing out of the system to reduce the amount of air, dust, and water vapour that can get into the backing vacuum system.

A.6 Restoring the Backing Vacuum

1. Ensure that all of the opened KF seals are properly closed and connected; then close the valve mounted on the roughing pump allowing nitrogen into the system. Close the nitrogen source and disconnect it from the vacuum system, replacing the blank KF seal.
2. Ensure that all of the required intermediate backing vacuum valves are opened (as all of these volumes should contain nitrogen gas. Activate the roughing pump and wait until the backing vacuum pressure reads ≈ 10 mbar.
3. Activate the backing vacuum turbo pump on the Low Speed (LS) setting via its controller and ensure it attains normal LS operation with its fan functioning properly.
4. When the backing vacuum pressure is restored to 10^{-5} to 10^{-6} mbar, open the three turbo pump exhaust valves. Check to make sure the collector, magnet, and

A.6. Restoring the Backing Vacuum

cathode chamber vacuum levels return to around pre-venting vacuum pressures and that their respective turbo pump power consumption levels return to normal.

Appendix B

Additional EBIT Component Schematics, Figures, and Photos

B.1 Schematic Drawing for Replacement Part

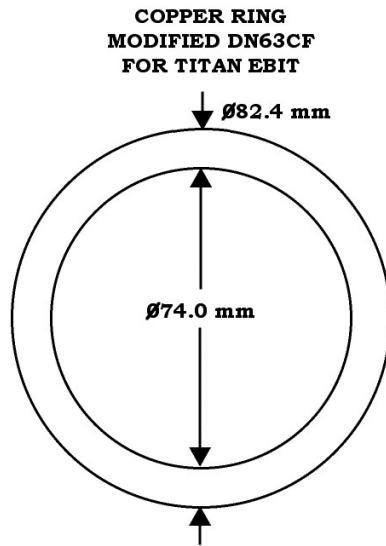


Figure B.1: Modified copper ring schematic for use with the TITAN EBIT collector and electron gun vacuum seals.

B.2 EBIT Photos

Additional photos include those from the EBIT assembly, the diagnostic components, a photo documenting a HV test setup, and an additional steerer lens photo.

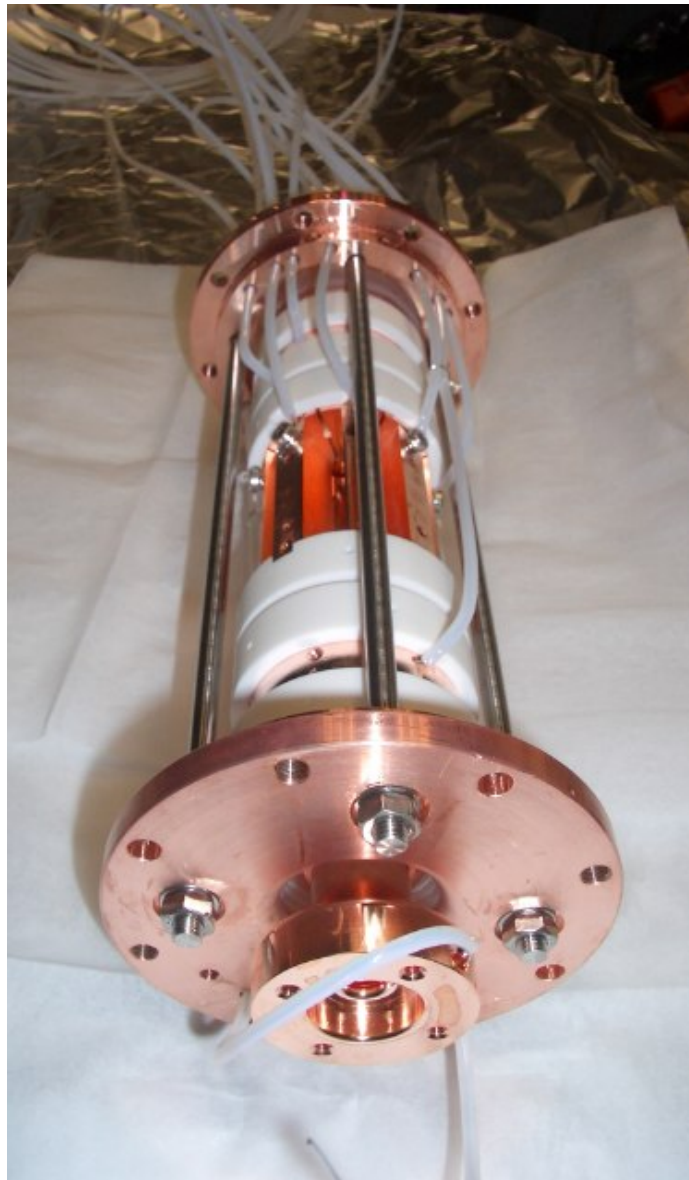


Figure B.2: Photo of the trap with connected wires during assembly.

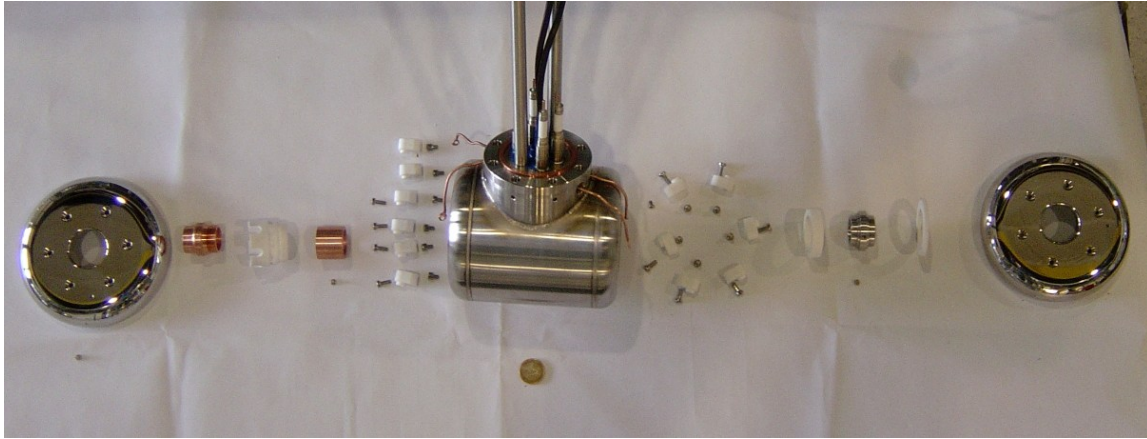


Figure B.3: The collector head after partial assembly.



Figure B.4: The collector head during assembly. Note that the copper seal visible is a custom size due to required geometry. For dimensions see Figure B.1.

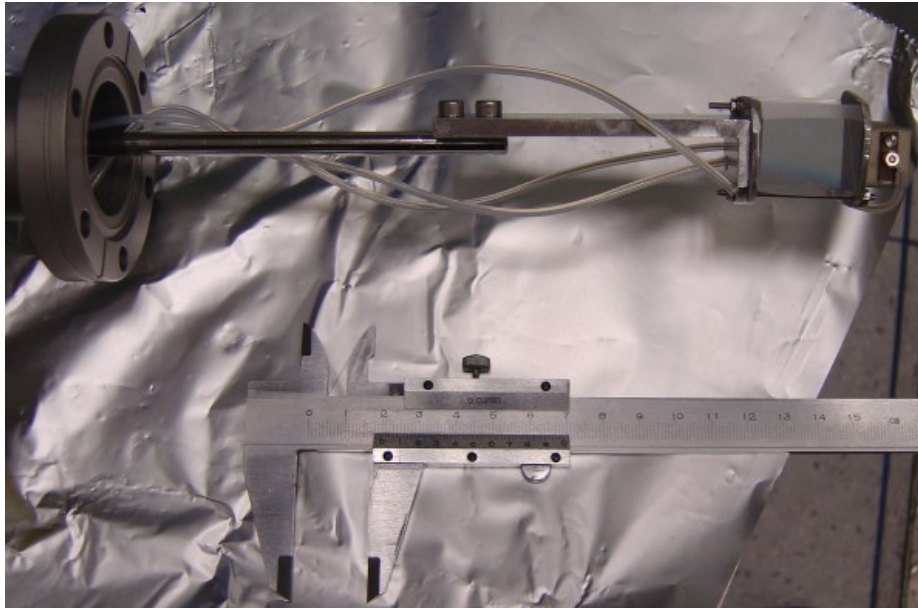


Figure B.5: The prism and channeltron assembly installed between the magnet and the electron gun. For optimal use and stability, the wires connected to the channeltron (as seen from the back side) were fed through the platform on which the prism is resting.



Figure B.6: Backside view of the channeltron and prism installed for diagnostic purposes.

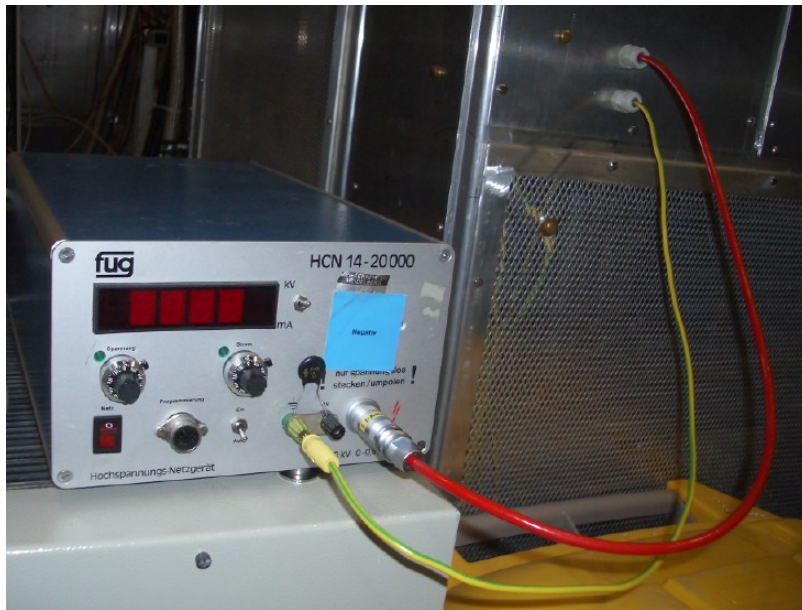


Figure B.7: The high voltage power supply setup used to float the electronics, electron gun, and collector to -20 kV.

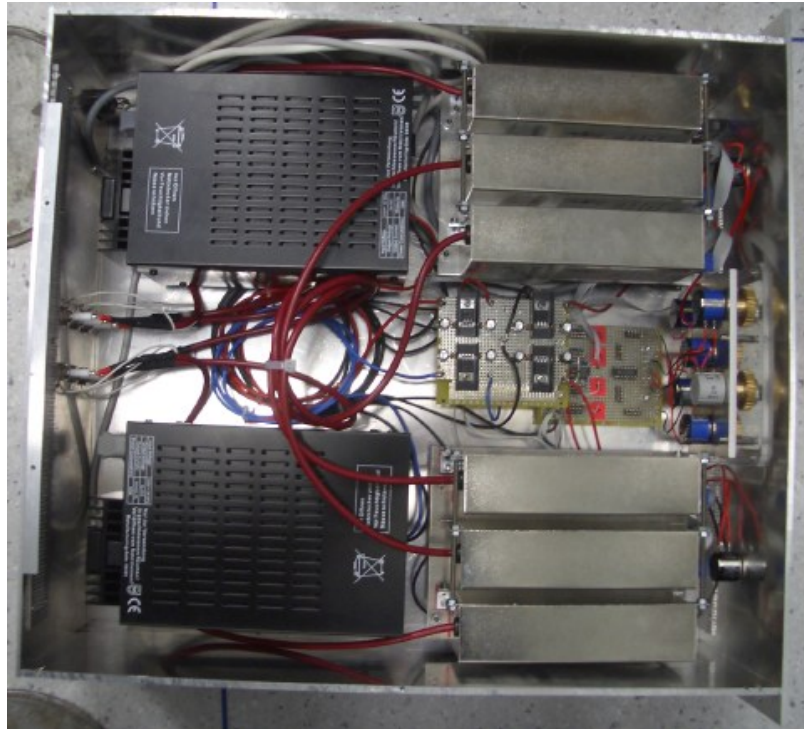


Figure B.8: Controller box for one of the steerer lenses used for ion beam focusing and steering. The large black units are the 24 V supplies for the six smaller HV power supplies to the right.

B.3 Printable Figures

Transformer figures and additional information are given here, in addition to the labels for the trap electrode feedthroughs and a trap cross-sectional view with the electron gun side on the left.

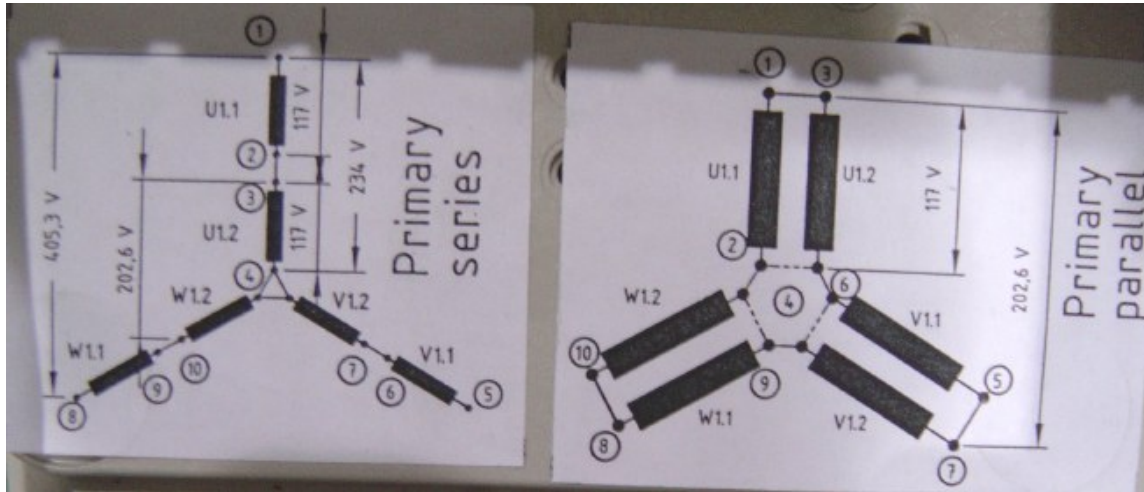


Figure B.9: Electrical schematic of the primary side of the transformer used for the HV cage. The left side is the configuration for European 220 VAC, while the right is for North American 110 VAC.

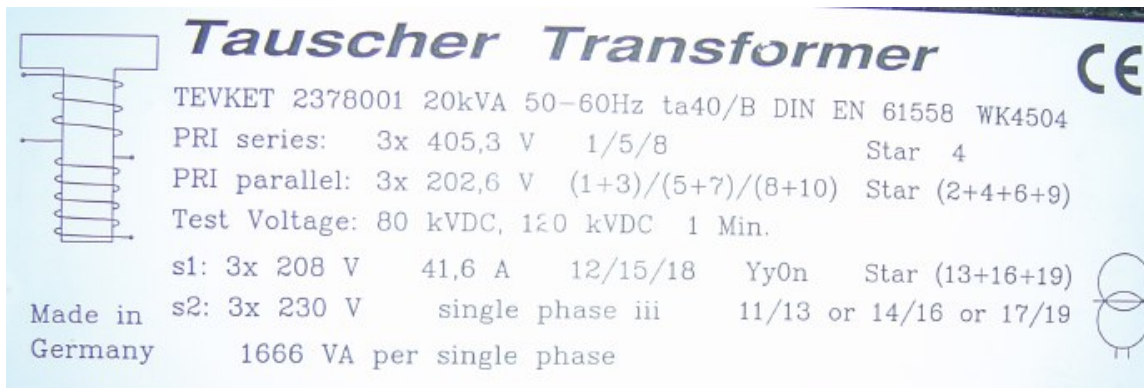
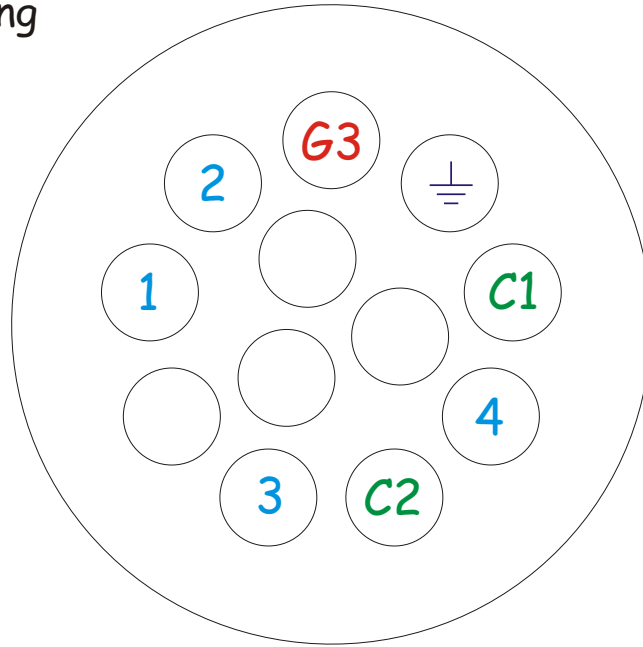


Figure B.10: Company label on the transformer with additional specifications.

Left Wing



Right Wing

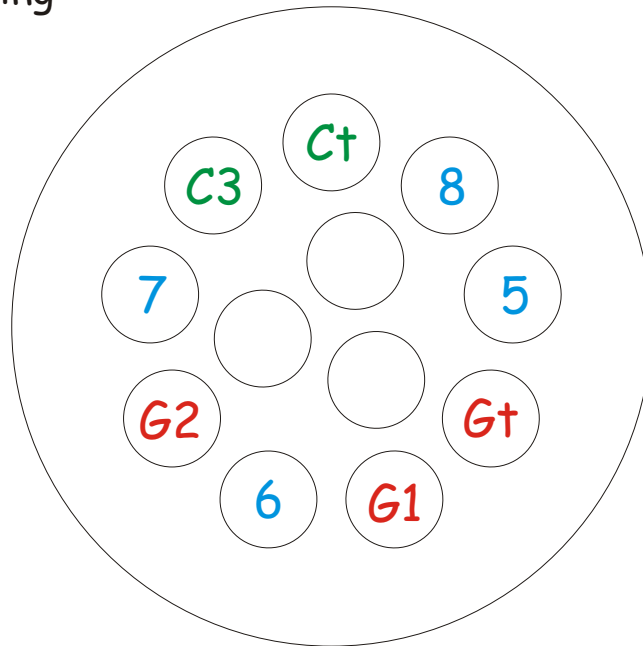


Figure B.11: Labels for the two twelve-piece electrical feedthroughs for the trap electrodes. Orientation is with respect to the electron beam.

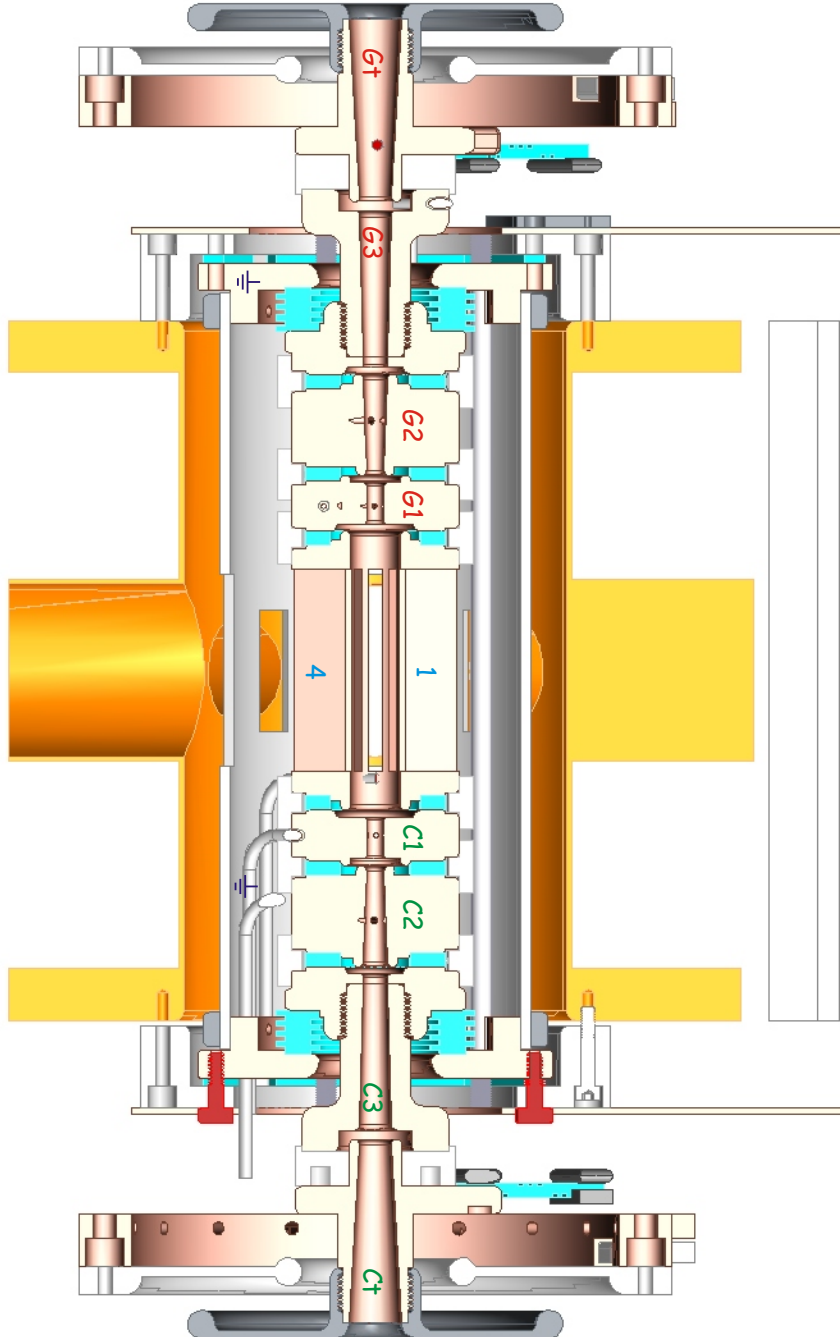


Figure B.12: Trap electrode labels with the electron gun on the left side.

Bibliography

- [1] F. Ames, R. Baartman, P. Bricault, K. Jayamanna, M. McDonald, M. Olivo, P. Schmor, D.H.L. Yuan, and T. Lamy. Charge state breeding of radioactive ions with an electron cyclotron resonance ion source at TRIUMF. *Review of Scientific Instruments*, 77:03B103, 2006.
- [2] L.H. Andersen and J. Bolko. Radiative recombination between fully stripped ions and free electrons. *Physical Review A*, 42:1184, 1990.
- [3] Atomic Physics Group at the Dresden University of Technology. Atomic physics group TU Dresden MCDF calculations with GRASP. Last Viewed: May 12, 2006. <http://www.physik.tu-dresden.de/apg/apehci.htm>.
- [4] R. Becker. Collision physics in ECR and EBIS/T. *Review of Scientific Instruments*, 73:693, 2002.
- [5] Reinard Becker. University of Frankfurt. Private communication.
- [6] E. Beebe, J. Alessi, S. Bellavia, A. Herschcovitch, A. Kponou, R. Lockey, A. Pikin, and K. Prelec. Results of beam tests on a high current EBIS test stand. In *Proceedings of the 1999 Particle Accelerator Conference, New York*, 1999.
- [7] E. Beebe, J. Alessi, A. Kponou, A. Pikin, and K. Prelec. A new generation of EBIS: High current devices for accelerators and colliders. In *Proceedings of EPAC 2002, Paris, France*, 2002.
- [8] P. Beiersdorfer. High-resolution x-ray spectra from low-temperature, highly charged ions. *AIP Conference Proceedings*, 389:121–136, 1997.
- [9] P. Beiersdorfer, T.W. Phillips, K.L. Wong, R.E. Marrs, and D.A. Vogel. Measurement of level-specific dielectronic-recombination cross sections of heliumlike Fe XXV. *Physical Review A*, 46:3812, 1992.
- [10] H.A. Bethe and E.E. Salpeter. *Quantum Mechanics of One- and Two- Electron Systems*. Springer, 1957.

-
- [11] P.R. Bevington and D.K. Robinson. *Data Reduction and Error Analysis for the Physics Sciences*. WCB McGraw-Hill, second edition edition, 1992.
- [12] H.F. Beyer and J.P. Shevelko. *Introduction to the physics of highly charged ions*. Institute of Physics Publishing, 2003.
- [13] C. Biedermann, A. Förster, G. Fußmann, and R. Radtke. First results from the Berlin EBIT. *Physica Scripta*, T73:360, 1997.
- [14] Laura Blomeley. First tests of a square wave RFQ cooler and buncher for TITAN. Master's thesis, McGill University, 2006.
- [15] G. Bollen. Mass measurements of short-lived nuclides with ion traps. *Nuclear Physics A*, 693:3, 2001.
- [16] M.P. Bradley, J.V. Porto, S. Rainville, J.K. Thompson, and D.E. Pritchard. Penning trap measurements of the masses of ^{133}Cs , $^{87,85}\text{Rb}$, and ^{23}Na with uncertainties ≤ 0.2 ppb. *Physical Review Letters*, 83:4510, 1999.
- [17] Leon Brillouin. A theorem of Larmor and its importance for electrons in magnetic fields. *Physical Review*, 67:260, 1945.
- [18] Hjalmar Bruhns. Max-Planck-Institute for Nuclear Physics. Private communication.
- [19] N. Cabibbo. Unitary Symmetry and Leptonic decays. *Physical Review Letters*, 10:531, 1963.
- [20] C. Carlberg, T. Fritioff, and I. Bergström. Determination of the ^{133}Cs and proton mass ratio using highly charged ions. *Physical Review Letters*, 83:4506, 1999.
- [21] J.A. Clark, G. Savard, K.S. Sharma, J. Vaz, J.C. Wang, Z. Zhou, A. Heinz, B. Blank, F. Bucchinger, J.E. Crawford, S. Gulick, J.K.P. Lee, A.F. Levand, D. Seweryniak, G.D. Sprouse, and W. Trimble. Precise mass measurement of ^{68}Se , a waiting-point nuclide along the rp process. *Physical Review Letters*, 92:192501, 2004.
- [22] Jason A. Clark. *Investigating the Astrophysical RP-Process through Atomic Mass Measurements*. PhD thesis, University of Manitoba, 2005.
- [23] Corning. Company producing Macor machinable glass ceramic.
- [24] Numa Crosthwaite. A beam line for the ion injection and extraction into and out of the TITAN EBIT. Technical report, Imperial College, London, 2005.

- [25] F.J. Currell, J. Asada, K. Ishii, A. Minoh, K. Motohashi, N. Nakamura, K. Hishizawa, S. Ohtani, K. Okazaki, M. Sakurai, H. Shiraishi, S. Tsurubuchi, and H. Watanabe. A new versatile electron-beam ion trap. *Journal of the Physical Society of Japan*, 65:3186, 1996.
- [26] L.J. Curtis and I. Martinson. *Lifetimes of Excited States in Highly Charged Ions*, chapter 10, pages 197–218. Springer-Verlag, 1999.
- [27] J. Dilling, P. Bricault, M. Smith, H.-J. Kluge, and TITAN collaboration. The proposed TITAN facility at ISAC for very precise mass measurements on highly charged short-lived isotopes. *Nuclear Instruments and Methods in Physics Research B*, 204:492, 2003.
- [28] J. Dilling et al. Mass measurements on highly charged radioactive ions, a new approach to high precision with TITAN. *International Journal of Mass Spectrometry*, 251:198, 2006.
- [29] E. D. Donets. Electron beam ion sources and associated physics at JINR. *Nuclear Instruments and Methods B*, 9:522, 1985.
- [30] E. D. Donets. Historical review of electron beam ion sources. *Review of Scientific Instruments*, 69:614, 1998.
- [31] E. D. Donets, V. I. Ilushchenko, and V. A. Alpert. In *Proceedings of the Premiere Conference sur les Sources d'Ions (INSTN, Saclay, France)*, page 625, 1969.
- [32] I. Draganić, J. R. Crespo López-Urrutia, R. DuBois, S. Fritzsche, V.M. Shabaev, R. Soria Orts, I.I. Tupitsyn, Y. Zou, and J. Ullrich. Precision wavelength measurements of QED-sensitive forbidden transitions in highly charged argon ions. *Physical Review Letters*, 91:183001, 2003.
- [33] S. Eidelman et al. Particle Data Group. *Physics Letters B*, 592:1, 2004.
- [34] Sascha Epp. Max-Planck-Institute for Nuclear Physics. Private communication.
- [35] R.B. Firestone and L.P. Ekström. WWW table of radioactive isotopes, version 2.1. Last Viewed: May 12, 2006. <http://ie.lbl.gov/toi/>.
- [36] T. Fuchs, C. Biedermann, R. Radtke, E. Behar, and R. Doron. Channel-specific dielectronic recombination of highly charged krypton. *Physical Review A*, 58:4518, 1998.
- [37] J. Gillaspay, editor. *Trapping Highly Charged Ions: Fundamentals and Applications*. Huntington, New York: Nova Science Publishers, Inc., 2001.

-
- [38] J. D. Gillaspy. First results from the EBIT at NIST. *Physica Scripta*, T71:99, 1997.
- [39] J. D. Gillaspy. Highly charged ions. *Journal of Physics B*, 34:R93, 2001.
- [40] W.G. Graham, W. Fritsch, Y. Hahn, and J.A. Tanis, editors. *Recombination of atomic ions*. New York : Plenum Press, 1992.
- [41] Dwight E. Gray, editor. *American Institute of Physics Handbook*. Mcgraw-Hill, 3rd edition, 1972.
- [42] Y.B. Hahn, R.E. Hebner, D.R. Kastelein, and K.J. Nygaard. Channeltron gain in magnetic fields. *Review of Scientific Instruments*, 43:695, 1972.
- [43] J.C. Hardy and I.S. Towner. Superaligned $0^+ \rightarrow 0^+$ nuclear β decays: A critical survey with tests of the conserved vector current hypothesis and the standard model. *Physical Review C*, 71:055501, 2005.
- [44] T.P. Heavner and S.R. Jefferts. Atomic mass of ${}^6\text{Li}$ using a Penning-ion-trap mass spectrometer. *Physical Review A*, 64:062504, 2001.
- [45] F. Herfurth et al. A linear radiofrequency ion trap for accumulation, bunching, and emittance improvement of radioactive ion beams. *Nuclear Instruments and Methods in Physics Research A*, 469:254, 2001.
- [46] Gabriel Herrmann. Optical theory of thermal velocity effects in cylindrical electron beams. *Journal of Applied Physics*, 29:127, 1958.
- [47] R. Hertenberger, Y. Eisermann, A. Hofmann, A. Metz, P. Schiemenz, S. Trieb, and G. Graw. Beam formation at the Munich atomic beam source. *Review of Scientific Instruments*, 69:750, 1998.
- [48] Scientific Instrument Services Inc. Company developing SimIon, a charged particle optics simulation program.
- [49] J.D. Jackson. *Classical Electrodynamics*, chapter 12.5, pages 592–596. John Wiley & Sons, Inc., third edition, 1999.
- [50] U. Kentsch, S. Landgraf, G. Zschornack, F. Grossmann, V.P. Ovsyannikov, and F. Ullmann. Dresden EBIT: Results and perspectives. *Review of Scientific Instruments*, 73:660, 2002.
- [51] O. Kester et al. Commissioning of the Rex-Isolde Linac. In *Proceedings of the 2001 Particle Accelerator Conference, Chicago*, 2001.

- [52] O. Kester et al. Status of REX-Isolde. In *Proceedings of LINAC 2004, Lübeck, Germany*, 2004.
- [53] Y.S. Kim and R.H. Pratt. Direct radiative recombination of electrons with atomic ions: Cross sections and rate coefficients. *Physical Review A*, 27:2913, 1983.
- [54] M. Kobayashi and T. Maskawa. CP-Violation in the renormalizable theory of weak interaction. *Progress of Theoretical Physics*, 49:652, 1973.
- [55] H.A. Kramers. The theory of x-ray absorption and of the continuous x-ray spectrum. *Philosophical Magazine*, 46:836, 1923.
- [56] Heat Wave Labs. Standard barium dispenser cathodes. Last Viewed: April 4, 2006. http://www.cathode.com/c_cathode.htm.
- [57] A. Lapierre et al. Relativistic electron correlation, quantum electrodynamics, and the lifetime of the $1s^2 2s^2 2p^2 p_{3/2}^0$ level in boronlike argon. *Physical Review Letters*, PRL 95:183001, 2005.
- [58] A. Lapierre et al. Lifetime measurement of the Ar XIV $1s^2 2s^2 2p^2 P_{3/2}^0$ metastable level at the Heidelberg electron-beam ion trap. *Physical Review A*, 73:052507, 2006.
- [59] R. Laxdal, R. Baartman, P. Bricault, G. Dutto, R. Poirier, and P. Schmor. Status of the ISAC accelerator for radioactive beams. In *Proceedings of LINAC Chicago, USA*, 1998.
- [60] M.A. Levine, R.E. Marrs, C.L. Bennett, J.R. Henderson, D.A. Knapp, and M.B. Schneider. EBIT: Electron beam ion trap. In *AIP Conference Proceedings*, volume 188, pages 82–101, 1989.
- [61] M.A. Levine, R.E. Marrs, J.R. Henderson, D.A. Knapp, and M.B. Schneider. The electron-beam ion trap - a new instrument for atomic physics measurements. *Physica Scripta*, T22:157, 1988.
- [62] David R. Lide, editor. *CRC Handbook of Chemistry and Physics*. Chapman and Hall/CRC, 82nd edition, 2001.
- [63] C. Litwin, M. C. Vella, and A. Sessler. Linear electrostatic instability of the electron beam ion source. *Nuclear Instruments and Methods in Physics Research*, 198:189, 1982.
- [64] J. R. Crespo López-Urrutia. Max-Planck-Institute for Nuclear Physics. Private communication.

-
- [65] J. R. Crespo López-Urrutia, A. Dorn, R. Moshhammer, and J. Ullrich. The Freiburg electron beam ion trap/source project FreEBIT. *Physica Scripta*, T80B:502, 1999.
- [66] J. R. Crespo López-Urrutia et al. Progress at the heidelberg ebit. *Journal of Physics: Conference Series* 2, pages 42–51, 2004.
- [67] W. Lotz. An empirical formula for the electron-impact ionization cross-section. *Zeitschrift für Physik*, 206:205, 1967.
- [68] R.E. Marrs, S.R. Elliot, and D.A. Knapp. Production and trapping of hydrogenlike and bare uranium ions in an electron-beam ion-trap. *Physical Review Letters*, 72:4082, 1994.
- [69] R.E. Marrs, D.H. Schneider, and J.W. McDonald. Projection x-ray microscope powered by highly charged ions. *Review of Scientific Instruments*, 69:204, 1998.
- [70] A.J. González Martínez et al. Benchmarking high-field few-electron correlation and QED contributions in Hg^{75+} to Hg^{78+} ions. *Physical Review A*, 73:052710, 2006.
- [71] A.J. González Martínez, J. R. Crespo López-Urrutia, J. Braun, G. Brenner, H. Bruhns, A. Lapierre, V. Mironov, R. Soria Orts, H. Tawara, M. Trinczek, and J. Ullrich. State-selective quantum interference observed in the recombination of highly charged $\text{Hg}^{75+\dots 78+}$ mercury ions in an electron beam ion trap. *Physical Review Letters*, 94:203201, 2005.
- [72] Antonio G. Martínez. *Quantum interference in the dielectronic recombination of heavy highly charged ions*. PhD thesis, University of Heidelberg, 2005.
- [73] J.W. McDonald, R.W. Bauer, and D.H.G. Schneider. Extraction of highly charged ions (up to 90+) from a high-energy electron-beam ion trap. *Review of Scientific Instruments*, 73:30, 2002.
- [74] D. J. McLaughlin, Y. Hahn, E. Takács, E. S. Meyer, and J. D. Gillaspay. Radiative and inner-shell dielectronic recombination in a highly charged barium ion. *Physical Review A*, 54:2040, 1996.
- [75] K. C. Mishra, R. Garner, and P.C. Schmidt. Model of work function of tungsten cathodes with barium oxide coating. *Journal of Applied Physics*, 95:3069, 2004.
- [76] A. Müller et al. Recombination of free electrons with ions. *Physica Scripta*, T37:62, 1991.

- [77] A. Müller and E. Salzborn. Scaling of cross sections for multiple electron transfer to highly charged ions colliding with atoms and molecules. *Physics Letters*, 62A:391, 1977.
- [78] N. Nakamura et al. The present status of the Tokyo electron beam ion trap. *Review of Scientific Instruments*, 69:694, 1998.
- [79] A. Nieminen et al. On-line ion cooling and bunching for collinear laser spectroscopy. *Physical Review Letters*, 88:094801, 2002.
- [80] Chris Osborne. TRIUMF. Private communication.
- [81] V.P. Ovsyannikov, G. Zschornack, F. Grossmann, S. Landgraf, F. Ullmann, and T. Werner. Highly charged ions produced in a warm electron beam ion trap. *Review of Scientific Instruments*, 71:690, 2000.
- [82] B.M. Penetrante, J.N. Bardsley, D. DeWitt, M. Clark, and D. Schneider. Evolution of ion-charge-state distributions in an electron-beam ion trap. *Physical Review A*, 43:4861, 1991.
- [83] J.V. Porto. Series solution for the image charge fields in arbitrary cylindrically symmetric Penning traps. *Physical Review A*, 64:023403, 2001.
- [84] R. Rao and O. Kultashev. Ir-Ce cathodes as high-density emitters in electron beam ion sources. *Measurement Science and Technology*, 8:184, 1997.
- [85] G. Savard, F. Bucchinger, J.A. Clark, J.E. Crawford, S. Gulick, J.C. Hardy, A.A. Hecht, J.K.P. Lee, A.F. Levand, N.D. Scielzo, H. Sharma, K.S. Sharma, I. Tanihata, A.C.C. Villari, and Y. Wang. Q value of the superallowed decay of ^{46}V and its influence on V_{ud} and the unitarity of the CKM matrix. *Physical Review Letters*, 95:102501, 2005.
- [86] Josha Schneider. Bericht zum 1. Praktischen Studiensemester. Technical report, Max-Planck-Institute for Nuclear Physics, 2006.
- [87] L. Schweikhard, P. Beiersdorfer, and E. Träbert. EBIT in the magnetic trapping mode: Mass spectrometry, atomic lifetime measurements, and charge transfer reactions of highly charged atomic ions. In F. Anderegg et al., editors, *Non-neutral Plasma Physics IV AIP CP606*, 2002.
- [88] Günther Sikler. TRIUMF. Private communication.
- [89] J.D. Silver, A.J. Varney, H.S. Margolis, et al. The Oxford electron-beam ion-trap - a device for spectroscopy of highly-charged ions. *Review of Scientific Instruments*, 65:1072, 1994.

- [90] Matthew J. Smith. A square-wave-driven radiofrequency quadrupole cooler and buncher for TITAN. Master's thesis, University of British Columbia, 2005.
- [91] J. Sugar and A. Musgrove. Energy levels of Krypton, Kr I through Kr XXXVI. *J. Phys. Chem. Ref. Data*, 20:859, 1991.
- [92] Stockholm Electron Beam Ion Trap. R-EBIT. Last Viewed: May 23, 2006. <http://atomlx04.physto.se/~rebit/>.
- [93] K. Widmann. *High resolution spectroscopic diagnostics of very high-temperature plasmas in the hard x-ray regime*. PhD thesis, University of Graz, 1998.
- [94] D.F.A. Winters, M. Vogel, D.M. Segal, and R.C. Thompson. Electronic detection of charged particle effects in a Penning trap. *Journal of Applied Physics of Physics B: Atomic, Molecular and Optical Physics*, 39:3131, 2006.
- [95] Z. Xikai, J. Dikai, G. Panlin, S. Shugang, Y. Heping, G. Peirong, W. Naxiu, S. Weiguo, C. Yonglin, X. Xiangyi, F. Shuqing, and Z. Tuantuan. Shanghai electron beam ion trap: Design and current status. *Journal of Physics: Conference Series*, 1:68, 2004.
- [96] X. Zhang, J. R. Crespo López-Urrutia, P. Guo, V. Mironov, X. Shi, A.J. González Martínez, H. Tawara, and J. Ullrich. Experimental study of the deep-lying dielectronic recombination resonances of He-like germanium ions. *Journal of Physics B*, 37:2277, 2004.